RCA Review

September 1972 Volume 33 No. 3
RCARCI 33(3) 481-604 (1972)

RCA Review, published quarterly in March, June, September and December by RCA Research and Engineering, RCA Corporation, Princeton, New Jersey 08540. Entered as second class matter July 3, 1950 under the Act of March 3, 1879. Second-class postage paid at Princeton, New Jersey, and at additional mailing offices. Effective Jan. 1, 1971, subscription rates as follows: United States and Canada: one year $6.00, two years $10.50, three years $13.50; in other countries, one year $6.40, two years $11.30, three years $14.70. Single copies (except for special issues) up to five years old $3.00.

RCA Review

A technical journal published quarterly
by RCA Research and Engineering
in cooperation with the subsidiaries
and divisions of RCA.

Contents

September 1972 Volume 33 Number 3

An Experimental Solid-State TV Camera Using a 32 x 44 Element Charge-Transfer Bucket-Brigade Sensor

Winthrop S. Pike, Michael G. Kovac, Frank V. Shallcross, and Paul K. Weimer

RCA Laboratories, Princeton, N. J.

Abstract—An experimental television camera, employing a 32 x 44 element charge-transfer bucket-brigade sensor, has been built. The design, construction, and performance of the camera are described. It was found that, within the limitations of its resolution capabilities, the camera produces good pictures at modest levels of illumination (5-20 foot candles). The camera's dynamic range is between 10:1 and 60:1. Improvements in silicon processing should permit extension of this range to lower illumination levels.

1. General

An experimental television camera employing a 32×44 element self-scanned bucket-brigade sensor has been constructed. The camera is shown in Fig. 1. It is cable-connected to a control box (Fig. 2) that contains a power supply, video amplifier, and sweep generators for the monitor. The entire camera chain including the monitor may be seen in Fig. 3. The camera is approximately $3.75 \times 2.75 \times 2.25$ inches exclusive of the lens. Weight, without lens, is about 12 ounces.

Fig. 1—The bucket-brigade camera.

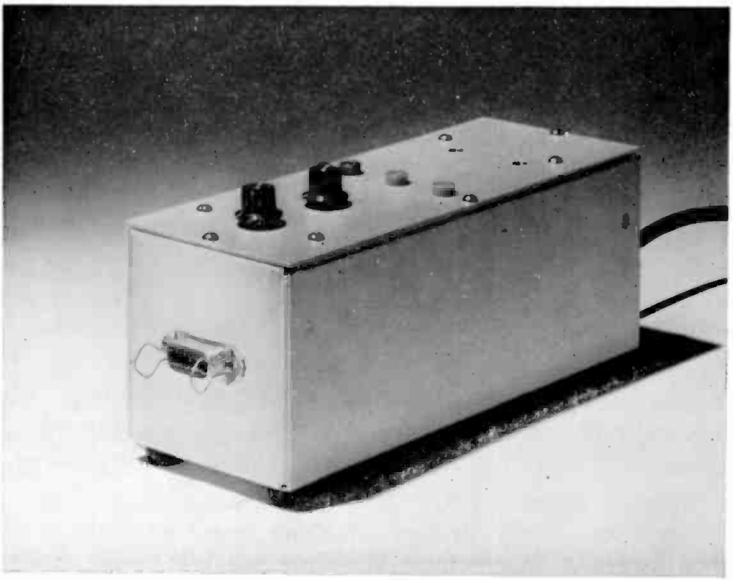

Fig. 2—The control box for the bucket-brigade camera.

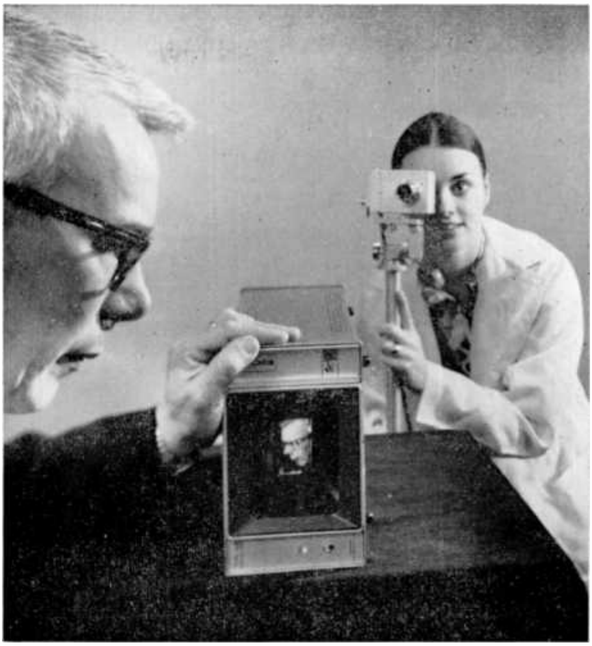

Fig. 3—The entire bucket-brigade camera chain in use, showing the monitor.

The camera chain, exclusive of the monitor, requires approximately 930 mW of power, which is provided by a commercial ± 15-volt dual regulated supply located in the control box. 653 mW is accounted for by the camera and the remainder, 278 mW, by the control-box circuits. Of the 653 mW used by the camera, about 250 mW is used in various bleeder chains that set the operating potentials of the sensor electrodes. Much of the remaining dissipation is in the driver circuits that interface the timing logic with the sensor. This could be reduced at least 50% by using complementary-symmetry drive circuits. Battery operation would be entirely feasible.

The camera operates in noninterlaced fashion at a frame rate of 60 Hz. Although the field rate used is identical to that in conventional broadcast television, the line rate is lower, as the sensor has only 32 horizontal lines of 44 elements each. The horizontal line rate is 2160 Hz and approximately three line times are allowed for vertical retrace. The nonstandard line rate necessitates the use of a commercial X-Y display unit as the monitor.

The camera operates with full frame-time storage, i.e., each element of the sensor integrates the illumination incident on it for the entire frame time. Because of the small number of lines (32), however, the readout time per line is a relatively large fraction (about 3%) of the total frame time. This causes a barely perceptible image smear, as light continues to be integrated at each sensor element during readout. With larger sensors having more elements, this phenomenon should decrease in importance.

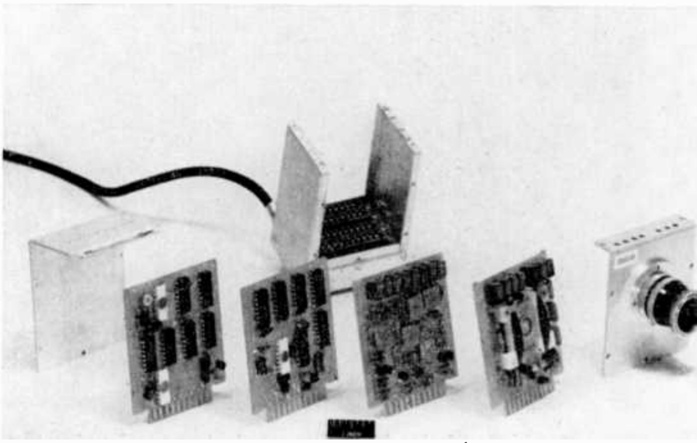

Fig. 4—An exploded view of the bucket-brigade camera showing the plug-in circuit cards.

Mechanically, the camera circuits are organized on four plug-in printed-circuit cards. These may be seen in Fig. 4. The card nearest the lens carries the solid-state sensor in its socket (see Fig. 5). The output processing circuit is just below the sensor, and trimmer potentiometers for setting various sensor potentials are located in a line above the sensor. A second card, behind the sensor card, carries the driver circuits and eight more trimmer potentiometers. The remaining two cards comprise the timing logic circuits. These have been implemented with 13 dual in-line, COS/MOS integrated circuit packages. The power savings made possible by this logic family are appreciable. The entire timing system consumes less than 10 mW. By contrast, a single binary counter in the resistor–transistor logic family used in an earlier camera consumed over 80 mW.

Fig. 5—The bucket-brigade camera showing the sensor.

2. The Bucket-Brigade Sensor

The 32 × 44 element bucket-brigade sensor employed in the camera has been described in a previous paper.[1] A charge pattern formed on the photodiode array is scanned by the transfer of charges via bucket-brigade registers to an output amplifier located on the same silicon chip. Fig. 6 is a block diagram of the principal components of the sensor that are integrated on the same chip. Each of the 32 rows of the sensor consists of a bucket-brigade register[2] in which the reverse-biased sources and drains of the MOS transistors act as photodiodes when illuminated.[3] During the 1/60-second period between scans, the horizontal clock voltages are disconnected from each line so that a charge pattern corresponding to the image builds up on the photodiodes. When a given line is to be scanned, the horizontal clocks are reconnected by means of the transmission gates, causing the charge

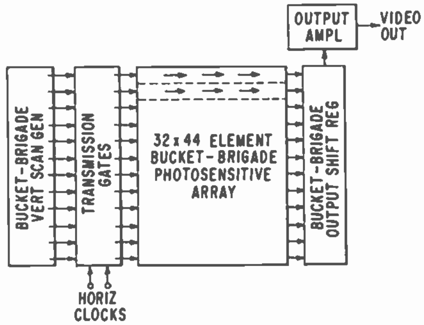

Fig. 6—Block diagram of the 32 × 44 element internally scanned bucket-brigade charge-transfer sensor.

pattern to be transferred toward the continuously running output register. The output register is a similar bucket brigade that delivers the charge packets in sequence to an output amplifier on the same chip. A 32-stage bucket-brigade vertical scan generator turns on the transmission gates for each line in sequence. Fig. 7 shows the actual circuit for each of the functions indicated in the block diagram. The two photodiodes associated with each element of the sensor registers are omitted from the drawing for lack of space.

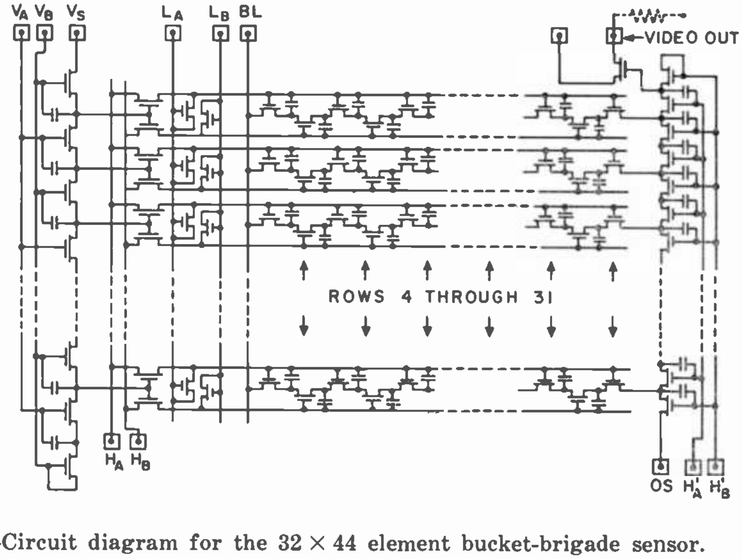

Fig. 7—Circuit diagram for the 32 × 44 element bucket-brigade sensor.

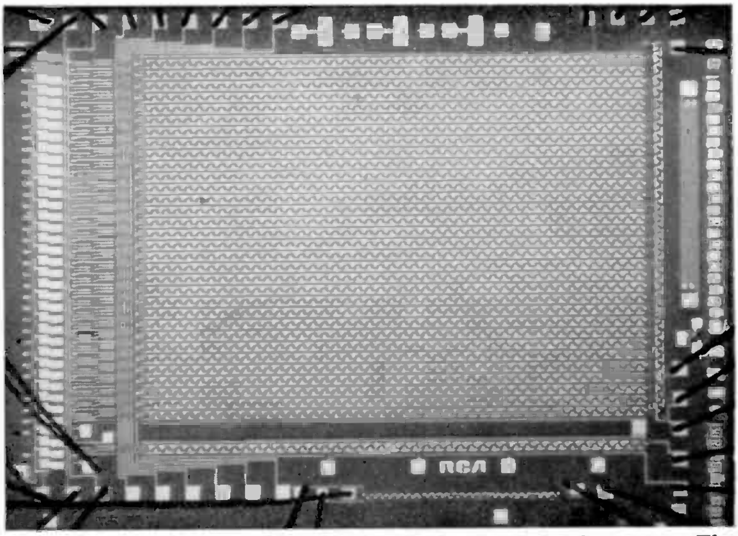

Fig. 8—Photomicrograph of the 32 × 44 element bucket-brigade sensor. The integrated sensor is 190 mils in the x direction and 140 mils in the y direction.

A photomicrograph of the completely integrated sensor is shown in Fig. 8. The output register is on the right and the vertical scan generator is on the left. The integrated sensor is 190 mils in the x direction and 140 mils in the y direction. The devices were fabricated using PMOS metal-gate technology. A more detailed photomicrograph of the upper right-hand corner of the sensor itself is shown in Fig. 9. Individual picture elements are spaced on 3-mil centers.

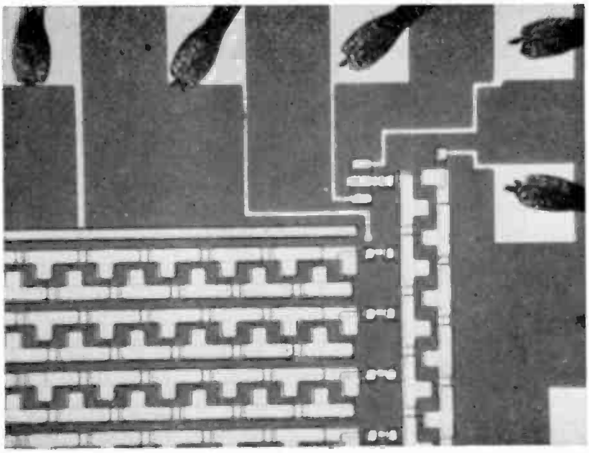

Fig. 9—Photomicrograph of top right corner of the 32 × 44 element bucket-brigade sensor showing a portion of the photosensitive array and the output shift register.

3. Circuit Design of the Camera

The electrical design of the camera is quite unlike that found in a conventional beam-scanned television camera tube. Instead of supplying linear saw-tooth currents to the horizontal and vertical windings of a deflection yoke, it is necessary to provide properly timed trains of pulses (typically square waves) to appropriate electrodes of the sensor. Fig. 10 is a block diagram of the camera. The solid-state bucket-brigade sensor is shown at the top; all of the elements enclosed within the dashed line are located on the sensor silicon chip.

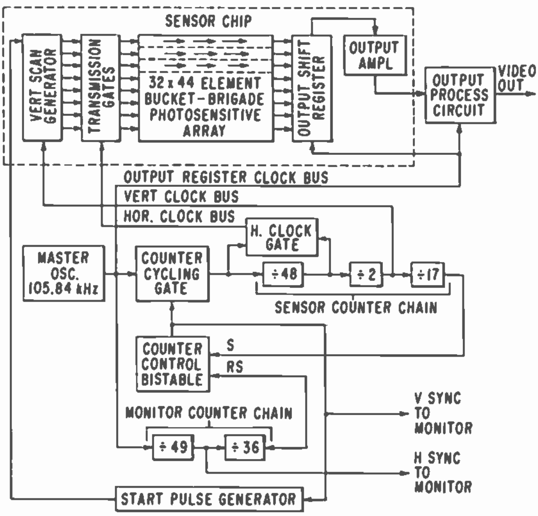

Fig. 10—Block diagram of the 32 × 44 element bucket-brigade camera.

Assume that a scan of the sensor is about to commence, i.e., the trailing edge of the vertical synchronizing pulse to the monitor has just passed. The start-pulse generator applies a pulse approximately 460 μsec (one horizontal line) in length to the vertical scan generator. The vertical scan generator is a 32-stage bucket-brigade shift register. The start pulse loads a logical "1" into the first stage of the register. (See Fig. 11.)

At the same time, clock square waves from the master oscillator are gated onto the horizontal clock bus by a gate driven from the divide-by-48 counter in the sensor counter chain. This bus connects to a set of transmission gates on the sensor chip driven by the 32 stages of the vertical scan generator. A logical "1" in any stage of the vertical scan generator will open the associated transmission gate, applying the master oscillator signal to the corresponding horizontal line of the sensor. When the horizontal clock voltages are applied to the first line of the sensor, the stored charges produced by the optical information impinging on this line are shifted to the right and into the output shift register. This register is continuously clocked by the master oscillator, hence any information fed into it is immediately shifted upward into the output amplifier on the chip.

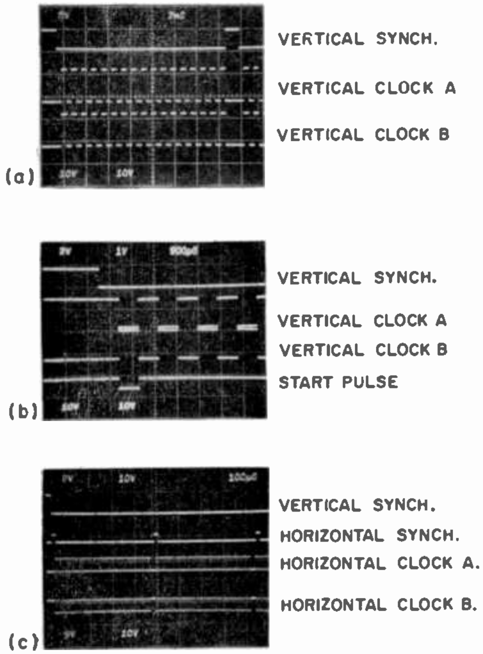

Fig. 11—Typical clock waveforms applied to the sensor.

After 44 clock cycles, the horizontal clock gate closes, cutting off the master oscillator signal from the horizontal clock bus. The divide-by-two counter in the sensor counting chain then changes state. This action causes any information in the vertical scanning shift register to advance one stage, hence the logical "1" in the first stage moves to the second. This opens the transmission gate between the horizontal clock bus and the second line of the sensor and closes the gate for the first line. Four horizontal clock cycles later, the horizontal clock gate re-opens and scanning commences on the second line.

It takes one clock period for the information at any given address of the sensor to shift to the next element to the right. Similarly, it takes one clock period for information in stage n of the output register to shift upward into stage $n+1$. The output register has one stage for each line of the sensor plus an extra stage on the output end. The extra stage has no particular significance as far as the operation of the sensor is concerned and was designed into it only for reasons connected with the sensor topology. As a result of the extra stage, however, when the top line of the sensor is scanned, there is a delay of one clock period before video information starts to emerge from the output amplifier. When the second line is scanned, there will be a delay of two clock periods and when the nth line is scanned, there will be a delay of n clock periods. Compensation must be provided for this progressive delay in order to correctly assemble the video information on the monitor.

The compensation is provided by a dual counter chain system. As shown in Fig. 10, the master clock oscillator directly clocks the continuously running output register. The master oscillator output is also applied via the counter cycling gate to the sensor counting chain and, without gating, to the monitor counting chain. Assume that the counter cycling gate under the control of the counter control bistable has just opened (bistable re-set) and that both counter chains are running. This corresponds to the start of a vertical scan.

The signal at the output of the counter cycling gate (which is also used to clock the sensor horizontal scanning circuits) is divided by 48 to obtain a pulse marking the end of each line. As each line has 44 elements, this allows a margin of four extra element times during which there is no useful video information. The vertical scanning register in the sensor is so designed that it advances to the next line on each half cycle of the vertical clock waveform. For this reason, the line frequency pulses from the divide-by-48 circuit are divided by two in a binary counter. This signal is used to clock the vertical register.

The last counter in the sensor counting chain counts off 17 cycles of the vertical clock signal corresponding to 34 lines. As the sensor has only 32 lines, this allows a margin of two extra line times. When the last counter completes its cycle, it sends a trigger pulse that sets the counter control bistable, closing the counter cycling gate and stopping the entire sensor counting chain. The signal from the counter control bistable is also used to initiate vertical flyback in the monitor, i.e., it is the vertical synchronizing signal to the monitor.

The monitor counter chain operates continuously, but its first counter counts by 49 rather than 48, as in the sensor counting chain. Thus, though both counters start in step (when the counter cycling gate opens), each succeeding pulse from the 49-times counter will be delayed with respect to the output pulses from the 48-times counter in the sensor counting chain by an amount, nE, where n is the number of the scanned line in the sensor and E is the element time (master clock period). By driving the monitor horizontal sweep circuit from the output of the 49-times counter, the sweep will be correctly timed with respect to the progressively delayed video information emerging from the sensor output register, and a correctly assembled picture will result on the monitor.

The pulses from the 49-times counter in the monitor counting chain are applied to a 36-times counter. At the 36th input pulse, this counter re-sets the counter control bistable to open the counter cycling gate and re-start the sensor counting chain. This action also terminates the vertical-flyback period of the monitor, releasing the sweep and allowing it to start scanning the next frame. It should also be noted that similar delay-compensation schemes (differing only in the divisors used in the counters) can be worked out for higher resolution sensors compatible with broadcast television standards.

A number of details of the timing system have been omitted in the interests of simplicity. For example, to ensure system timing stability, the duration of the start pulses, horizontal synchronizing pulses, vertical synchronizing pulses and various other internally necessary gating pulses are all digitally controlled by decoding the appropriate time slots of the applicable counters. The significant waveforms applied to the sensor are shown in Fig. 11. Fig. 11(a) shows the vertical synchronizing pulse and the two-phase vertical clocks applied to the sensor. Fig. 11(b) shows the same clocks and the vertical synchronizing pulse, but with an expanded time scale and with the addition of the start pulse. Fig. 11(c) shows the vertical synchronizing pulse, horizontal synchronizing pulses, and the horizontal clocks applied to the sensor. Note that the notches in the horizontal clock waveforms where the latter are gated off at the end of each line are in phase with the horizontal synchronizing pulses at the start of the frame (left side of photo) and then gradually become increasingly out of phase with them in succeeding lines. This shows the action of the double counter-chain system in compensating for the delay produced by the output register. It should also be noted that all of the bucket-brigade registers in the sensor require two-phase clocking, so that the sensor horizontal clock bus, vertical clock bus, and output register clock bus are actually dual bus bars carrying in-phase and antiphase gated square-wave clock signals. Further, the array of transmission gates in the sensor actually comprises two gates for each horizontal line.

Power is supplied to the timing logic circuits at 9 volts from an emitter follower regulator operating from the regulated +15 volt bus.

Thus, the logic levels available from the timing system are 0 and +9 volts (approximately).

The circuit used to interface the logic with the sensor is shown in Fig. 12. This configuration is used with minor variations for all clock pulses supplied to the sensor. Basically it is a simple long-tailed-pair current-switching circuit. A current set by R_1 is switched alternately to the collector circuit of Q_1 or Q_2. With equal resistors, R_3 and R_4 in the collectors, equal clock voltages adjustable in amplitude by means of R_1 are produced across R_3 and R_4. Most experimental sensors produced so far require clock voltages of the order of 6 to 8 volts peak-to-peak, and the parameters of the circuit shown are adjusted so that 12 to 13 volts of clock signal can be produced if needed.

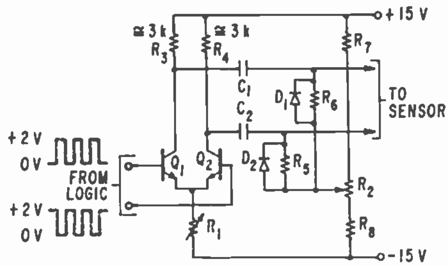

Fig. 12—Typical sensor driver circuit.

The signals at the collectors of Q_1 and Q_2 are capacitively coupled to the sensor by C_1 and C_2, and an adjustable dc component may be introduced by R_7, R_2, R_8, R_5, R_6 and clamp diodes D_1 and D_2. A bias range of ±5 volts has been provided for most of the sensor electrodes to which clock signals are applied.

The video signal at the sensor output has a form that is peculiar to bucket-brigade circuits and quite unlike the signals from a conventional camera tube. The sensor output signal is generated by using the gate of a MOS transistor to sample the voltage of the diffused p+ island in the last stage of the output register. A line-selector oscilloscope photo of approximately one horizontal line of the sensor output is shown in Fig. 13 (top trace). The useful video signal is embedded in the clock. With no light on the sensor, the output is a square wave at the clock frequency. Increasing light causes an upward modulation of the negative half cycles of the square wave. This may be seen on the seventh and eighth cycles from the left of the picture where a light spot has been focused on the sensor. At light saturation, the clock signal disappears entirely. It is desirable to process the signal to remove the clock component before applying it to the display monitor.

Two different methods of doing this have been tried. A sample-and-

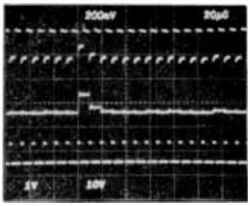

Fig. 13—Waveforms of the sample and hold video processing circuit.

hold processor is an obvious solution. The circuit actually used in one version of the camera is depicted in Fig. 14. Signal from the sensor is applied to emitter follower Q_1 through a capacitor and diode-clamp circuit that establishes the positive peaks of the video waveform at a definite dc level of approximately +5 volts. Transistor Q_2 acts as the sampling switch. Sampling pulses about ¼ clock cycle in length and timed to occur during the negative half cycle of the sensor output waveform are applied to the gate of Q_2. These cause the instantaneous voltage from the sensor at the moment of sampling to be stored on capacitor C_2. Transistors Q_3 and Q_4 form a simple impedance converter, with a very high input impedance and an acceptably low output impedance, to couple the signal on C_2 to the output terminal. The effectiveness of this technique may be assessed by comparing the top and middle traces in Fig. 13. The sampling pulses are also shown in Fig. 13.

A promising, less conventional, method for recovering the video signal is to make use of the signal at two successive nodes of the bucket-brigade output register.[1] The circuit and the applicable waveforms are shown in Fig. 15. By summing the signals at two successive nodes, P_1 and P_2 of a bucket-brigade, the clock signals can be quite effectively removed. In another version of the camera, an external bucket brigade four stages long and constructed of discrete components serves this purpose. It is located on the sensor printed-circuit card just below the sensor socket and may be seen in Fig. 5. An attractive feature of this type of processor is that it could ultimately be built into the sensor as an integral part of the output register.

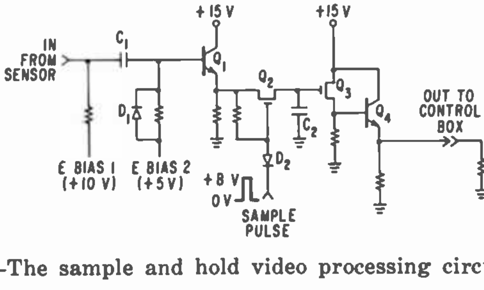

Fig. 14—The sample and hold video processing circuit.

All of the previously described circuits are located in the camera. The latter is cable-connected to its control box, power at ±15 volts being supplied to the camera via the cable. Video signal and horizontal and vertical synchronizing pulses also flow via the cable to the control box.

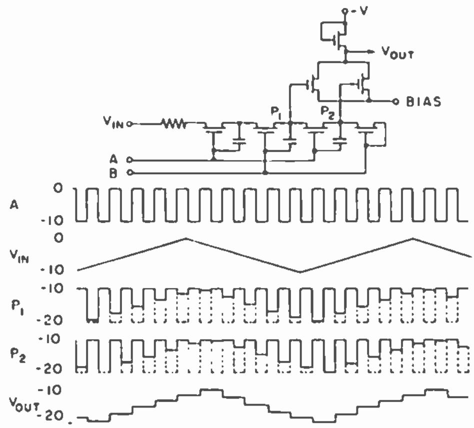

Fig. 15—The bucket-brigade summing processor for extracting video signals from the clock waveform.

The video signal at the output of the processor in the camera has a peak-to-peak amplitude approaching 0.5 volt. In the control box, this signal is applied to a gain control and then to the dc level-setting and blanking-insertion circuit. It then passes through a video amplifier. The net voltage gain from input to output of this system is about 10 times. The control box also contains horizontal and vertical sweep circuits for the monitor. Three signals are fed to the monitor: video, horizontal sweep, and vertical sweep.

4. Performance Characteristics

A typical picture produced by the camera is shown in Fig. 16. This picture was taken with an illumination of about 20 foot-candles incident on the scene (from "cool white" fluorescent lamps) and with the camera lens (13 mm $f/1.1$) set at an aperture of approximately $f/1.5$. With the lens wide open, recognizable images can be obtained down to about 1 foot candle. The limited resolution of the 32×44 sensor is readily apparent. Note, also, the pattern of white spots. These are elements in the sensor that have an abnormally high dark current.

Fig. 16—A typical picture from the solid-state bucket-brigade sensor.

The gray scale and dynamic range of the camera have been investigated using a calibrated step wedge test pattern. The pattern available covered a brightness range of about 60:1 (from 12.1 to 0.2 foot-lamberts). Fig. 17 depicts the response of one line of the sensor to this pattern. The scale factor and centering of the line-selector

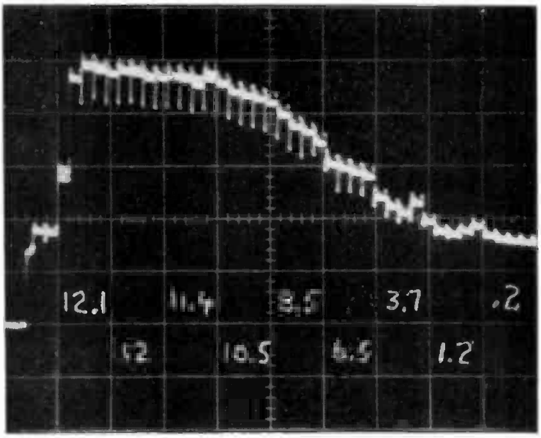

Fig. 17—Line-selector oscilloscope photograph of the response of the bucket-brigade sensor to a gray-scale test pattern. The numbers represent the brightness of each step in foot-lamberts.

oscilloscope have been adjusted to make the gray-scale steps correspond approximately with the graticule divisions. The light intensities of the steps, in foot-lamberts, are indicated on the photograph. The brightest step (12.1 foot lamberts) has been adjusted by means of the camera iris to be just below the level at which the sensor saturates.

It is difficult, due to the dark-current variations from element to element of the sensor, to determine where the sensor response goes to zero. Some insight into this may be gained from Fig. 18, which shows

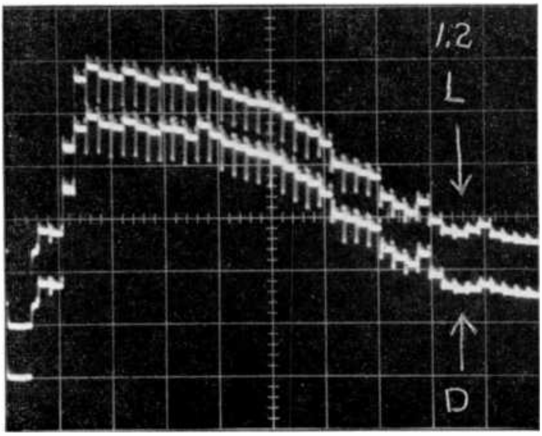

Fig. 18—Line-selector oscilloscope photograph of the response of the bucket-brigade sensor to a gray-scale test pattern. In the upper (L) trace, conditions are exactly as in Fig. 17. In the lower (D) trace, the two lowest steps have been occulted.

a double exposure of the step wedge. In the top trace, all conditions are as in Fig. 17. In the bottom trace, the 1.2-foot-lambert step and the 0.2-foot-lambert step of the test wedge are occulted with a piece of black felt. The difference between the top (light) trace and the bottom (dark) trace is quite apparent on the 1.2-foot-lambert step but not on the 0.2-foot-lambert step. We conclude that this particular experimental sensor has a dynamic range of not less than 10:1 (12.1/1.2) nor more than 60:1 (12.1/0.2).

This statement needs some explanation. Fluctuations in the dark current from element to element appear to be at least two orders of magnitude greater than the noise level of the rather low-gain amplifiers used in the camera video system. Fig. 19 depicts typical video signals from 10 lines of the sensor with no illumination on it. These show the fluctuations along the base line as well as about one quite high dark current spike (positive going) per line. (The negative-going pulses are the horizontal blanking signals.) Improvement in processing of the sensor and the use of higher-quality silicon, as in the silicon vidicon, should reduce the severity of this problem.

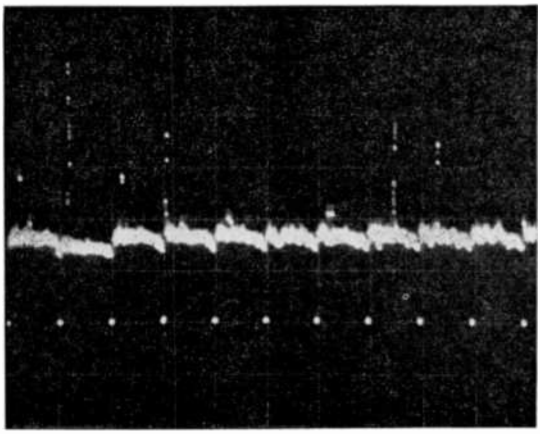

Fig. 19—Video output of ten lines of the bucket-brigade sensor showing dark-current fluctuations.

The overload characteristic of the silicon sensor also warrants brief comment. If a spot of light of sufficient brightness to cause overload is imaged on one of the elemental photosensors of the array, blooming occurs. However, it does not spread out uniformly in the observed picture as in a conventional television camera. Instead, it tends to spread laterally along the line associated with the overloaded element. In effect, the buckets become filled to overflowing and resolution along the line is lost. Several promising methods of overcoming this effect are being pursued. A good feature of the sensor however, is that recovery is rapid (typically within one frame-time) and no permanent damage to the sensor results.

Another interesting characteristic of the bucket-brigade sensor is that it has no perceptible lag.

5. Conclusions

A miniature television camera has been built around an experimental charge-transfer bucket-brigade sensor having 32 rows of 44 elements each. Within the limitations of its resolution capabilities, the camera produces good pictures at modest levels of illumination (5-20 foot candles). The camera's dynamic range appears to lie between 10:1 and 60:1, but as it was limited in the sensors tested by dark-current variations from element to element rather than by noise, this range can be extended toward lower illumination levels by improvements in silicon processing. Two effective methods have been developed for eliminating coherent clock interference from the camera video output, and the performance of the bucket-brigade sensor in this respect is appreciably superior to earlier, thin-film, X-Y addressed sensors. In view of the encouraging performance of this camera, larger sensors using bucket-brigade and charge-coupled registers should be evaluated.

Acknowledgments

The assistance of V. L. Frantz in the fabrication of the sensor and J. L. Pointkowski in the construction of the camera and its control box is gratefully acknowledged.

References:

[1] M. G. Kovac, W. S. Pike, F. V. Shallcross, and P. K. Weimer, "Solid State Imaging Emerges from Charge Transport," **Electronics**, Feb. 28, 1972.

[2] F. L. J. Sangster and K. Teer, "Bucket-Brigade Electronics—New Possibilities for Delay, Time-Axis Conversion and Scanning," **IEEE J. Solid-State Circuits**, June 1969, p. 131-136.

[3] P. K. Weimer, M. G. Kovac, F. V. Shallcross and W. S. Pike, "Self-Scanned Image Sensors Based Upon Charge Transfer by the Bucket-Brigade Method," **IEEE Trans. Electron Devices**, Nov. 1971, pp. 996-1003.

The Silicon Return-Beam Vidicon— A High-Resolution Camera Tube

Ralph W. Engstrom

RCA Electronic Components, Lancaster, Pa.

John H. Sternberg

RCA Astro-Electronics Division, Princeton, N. J.

Abstract—An experimental program was recently completed introducing a silicon diode array target into the configuration of a two-inch return-beam vidicon. Large silicon targets with 130 diodes per millimeter were fabricated. Tubes were constructed with the targets mounted directly on the inside surface of the faceplate. The new camera tube provides the wide spectral response and minimum lag associated with the silicon diode array target, and a limiting resolution exceeding 60 cycles per millimeter.

1. Introduction

Currently, the 2-inch and the 4.5-inch return-beam vidicon (RBV)[1,2] tubes offer near-photographic resolution capabilities. This paper describes the result of substituting a silicon diode-array target[3] for the ASOS (antimony-oxide-sulfide) photoconductive target. Both the ASOS- and the silicon-type RBV tubes were designed for use as single-frame, slow-scan sensors, but the silicon RBV tube is also operable in a conventional TV mode.

Conventional silicon targets have a diode center-to-center spacing density of 72 per millimeter. In order to improve the resolution capability of the tube, special silicon targets were made having spacing density of 130 per millimeter. Experimental tubes were built that demonstrated that high-resolution silicon-target tubes are practical.

This paper describes the new silicon target and the manner in which it was incorporated in the RBV-type camera tube. Results are given together with a discussion of the limiting factors of the design. Applications to 2000-line continuous-scan and to frame readout under minimum lighting conditions are described. Possibilities of improving the device through changes in the target, the electron gun, and the dynode structure are outlined.

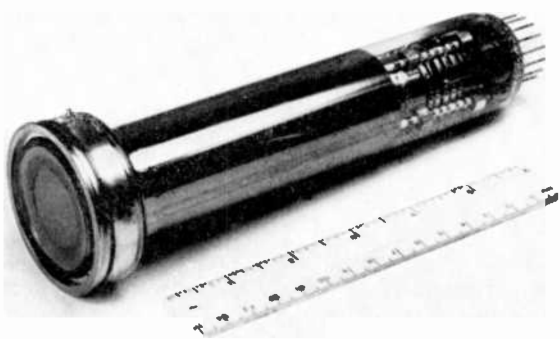

Fig. 1—Photograph of the two-inch silicon RBV tube.

2. Tube Construction

Other than the target and minor variations in the faceplate construction, the experimental silicon RBV tube is identical in construction with the 2-inch RBV (RCA Developmental Type C23061A). The electron gun is a scaled-down version of the 4.5-inch RBV electron-gun design,[1] a triode type using a dispenser-type cathode. The defining aperture of the gun has a diameter of 0.0007 inch. The all-magnetic electron optics are such that the aperture of the gun is demagnified by 2:1 at the target, providing a fine spot for high-resolution capability.

The general construction of the tube can be seen in Fig. 1. Overall length is 8.325 inches; maximum diameter is 2.300 inches.

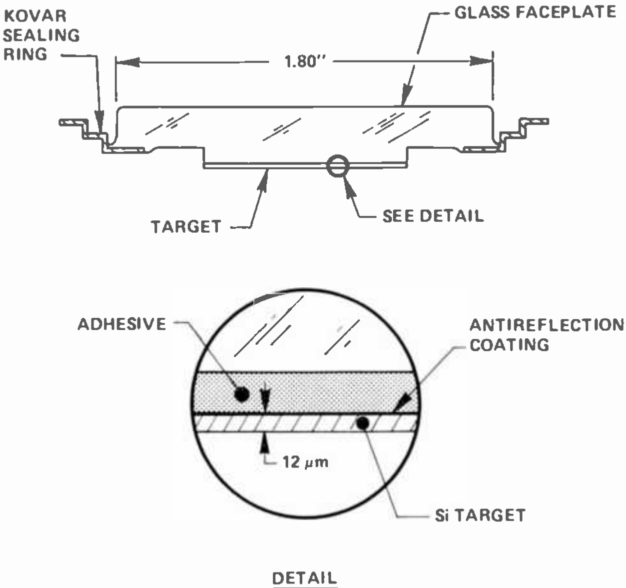

Fig. 2—Diagram of faceplate and target mounting for the two-inch silicon RBV.

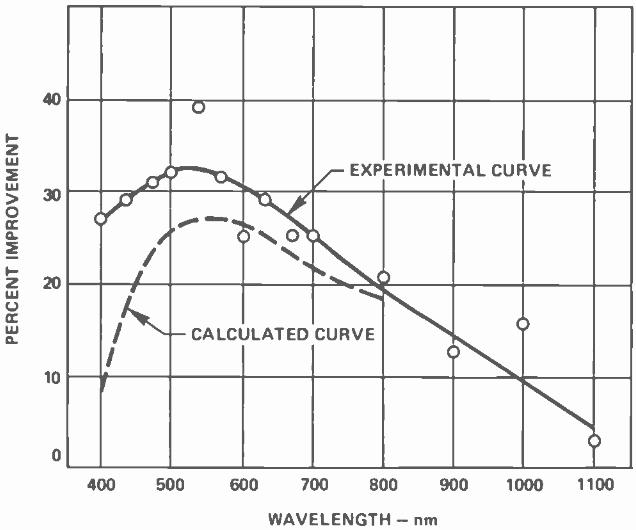

Fig. 3—Spectral distribution of the improvement in sensitivity resulting from a one-quarter-wavelength (at 600 nm) coating of TiO_2 on the silicon target.

The silicon target was mounted directly on the faceplate of the tube using a specially outgassed, silicone-rubber adhesive, as illustrated in Fig. 2. This mounting provided a rugged construction and a good optical contact. A quarter-wave thickness of TiO_2 (index of refraction 2.7) was evaporated onto the target, providing an antireflection coating match between the silicon (index of refraction approximately 3.9) and the adhesive (index of refraction 1.406). Fig. 3 shows the percent improvement in the spectral response anticipated and measured using this coating. The measurements were made by evaporating the antireflection coating on only one half of a target and comparing the sensitivities of the two halves.

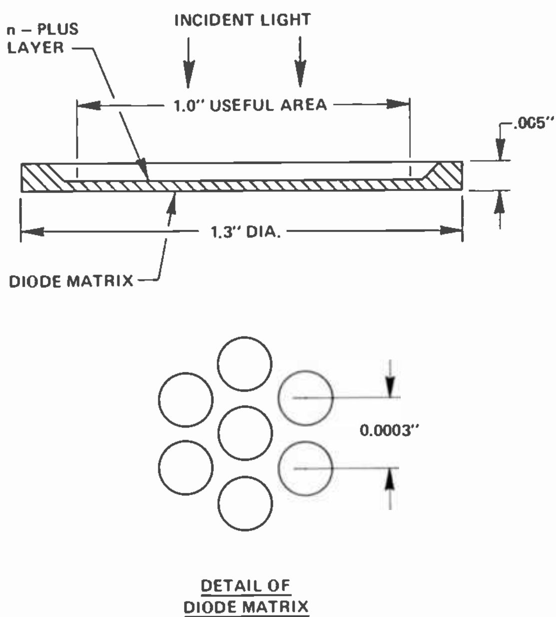

Fig. 4—Diagram of the silicon diode array.

3. Description of the Silicon Target

For this project, special, high-resolution silicon targets were fabricated in the configuration shown in Fig. 4. The useful diagonal of the target is 1.0 inch; thickness is about 12 μm. The diodes were grown in an hexagonal array to accomplish a 15% tighter packing than for a conventional square array; center-to-center spacing is 0.0003 inch (130 per mm). Although this geometry is of significantly smaller dimension than that of conventional silicon diode matrices, the quality of the initial targets was quite good. In fact, it was judged feasible to project the technology to a diode spacing of 160 per millimeter and to a target size capable of accommodating a 1 inch × 1 inch raster.

The performance of these targets retains the advantageous characteristics of conventional silicon-vidicon targets. Quantum efficiency approaches unity throughout the vasible range. The spectral response extends from 0.35 to 1.1 μm. The ultraviolet response is limited practically by the faceplate transmission, the infrared by the bandgap of the silicon. Because the signal developed in the silicon target is proportional to the input radiation, the device has a unity gamma characterstic in the operating range.

4. Predicted Performance and Experimental Results

Several tubes were fabricated and tested for key performance parameters, including MTF (Moduation Transfer Function), lag, sensitivity, and spectral response. These experimental tubes had 1-inch-diameter targets; however, it was anticipated that 1.4-inch-diameter targets would be installed in future designs offering a 1 inch × 1 inch raster. The tests were, therefore, conducted using a 1 inch × 1 inch square raster, as is used in the 2-inch RBV's. Those data that are affected by raster size (e.g., dark current) were adjusted to predict performance of a 1 inch × 1 inch active target area. However, the experimental configuration is in itself an attractive tube offering 2000 TV line performance for conventional TV applications.

In the following paragraphs, the results of these tests and predicted performance capabilities are compared.

4.1 Modulation Transfer Function

There are a number of factors that contribute to the overall MTF of the tube. Estimated MTF's of these individual factors are shown in Fig. 5.

Curve No. 1 represents the calculated response of the hexagonal diode array to a sine-wave bar pattern. Above a spatial frequency of 65 cycles per millimeter—half the diode spatial frequency—the curve is not a true indication of usefulness because of the onset of moire patterns. Curve No. 2 represents the calculated loss of response due to the diffusion of minority carriers in the field-free region between the depletion region and the backplate of the target. The calculation followed the analytical treatment of Crowell and Labuda.[3] The following values, representative of typical conditions, were used; 12 μm thickness, 50 ohm-cm resistivity, 1 μs lifetime, 3.3 μm field-free region, 8 V applied target voltage, and 3.5 V contact potential. Curve No. 3 shows the degradation due to the effect of the field mesh on the electron beam. This estimate was based on data from Schade[1] for the 1500 inch^{-1} mesh. Curve No. 4 is the gun-aperture response using a $\cos^2$-type of electron-emission distribution, also as suggested by Schade;[1] the diameter of the imaged aperture was taken as 9.25 μm. Again following Schade, Curve No. 5 shows the MTF resulting from the effect of electron thermal velocities. The product of all of the MTF curves of Fig. 5 represents the predicted MTF for the complete tube.

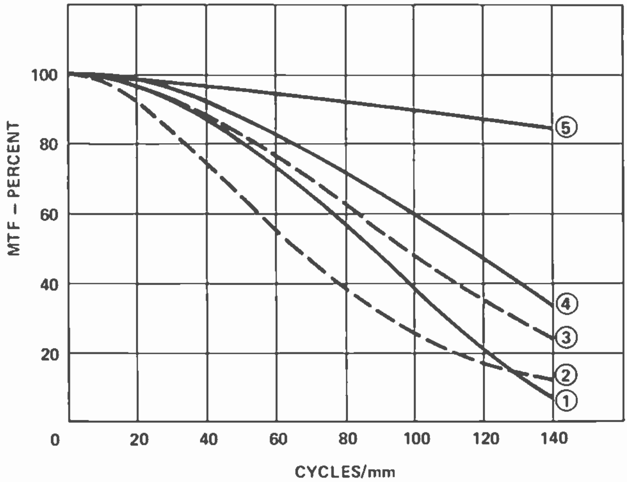

Fig. 5—Modulation transfer functions of the various elements that contribute to the overall MTF of the silicon RBV tube. These curves are estimates only, based on considerations discussed in the text: Curve No. 1—diode pattern geometry; Curve No. 2—minority carrier diffusion; Curve No. 3—field mesh; Curve No. 4—electron-gun aperture; Curve No. 5—electron-velocity distribution.

The predicted and measured MTF data are shown in Fig. 6. The experimental data were taken with square-wave test patterns but corrected to sine-wave response. The experimental data were also corrected for the MTF of the El Nikkor lens used in the measurement program.

The MTF for the silicon RBV tube was found to be a function of the cathode current as illustrated in Fig. 7. The reason for the degradation in MTF as the cathode current is increased is the spreading of the electron velocity distribution (Curve No. 5, Fig. 5). As the bias of the gun is reduced to increase the aperture current, there is an increase in the radial energy of those electrons that pass through the aperture and a consequent increase in the distribution of electron velocities in the axial direction.

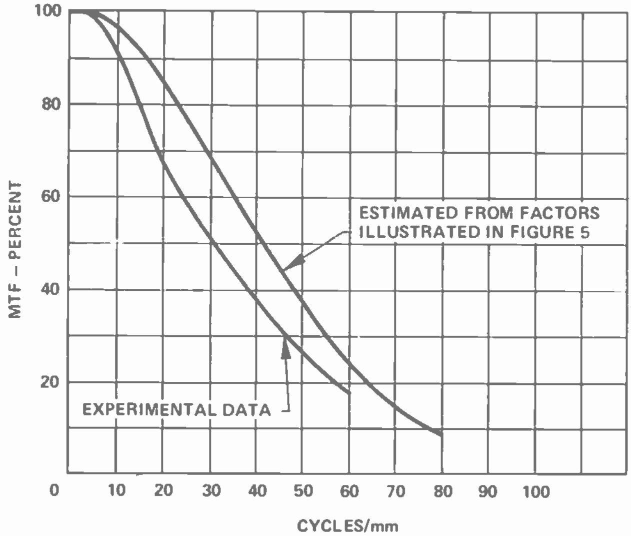

Fig. 6—A predicted MTF curve for the silicon RBV obtained by multiplying the ordinate values of the 5 curves shown in Fig. 5. Experimental data are shown after corrections from square-wave to sine-wave response and for MTF losses in the optical system.

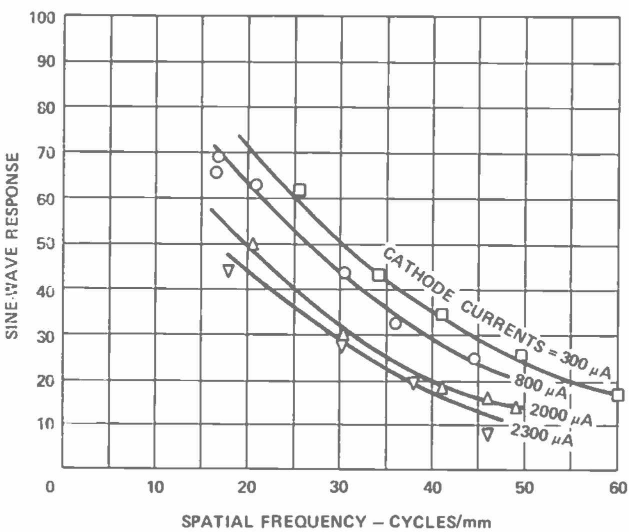

Fig. 7—These curves show the effect of electron-beam current on the MTF.

A picture is reproduced here, Fig. 8,* showing the general capability of the silicon RBV tube. The numbers in the large center circle when multiplied by 0.4 indicate line pairs per millimeter on the silicon target. Within the smaller circle at the bottom of the large circle (enlarged area in Fig. 8), the lines are numbered directly in line pairs per millimeter. Direct observation of the monitor indicated the limiting resolution was 60 line pairs per millimeter.

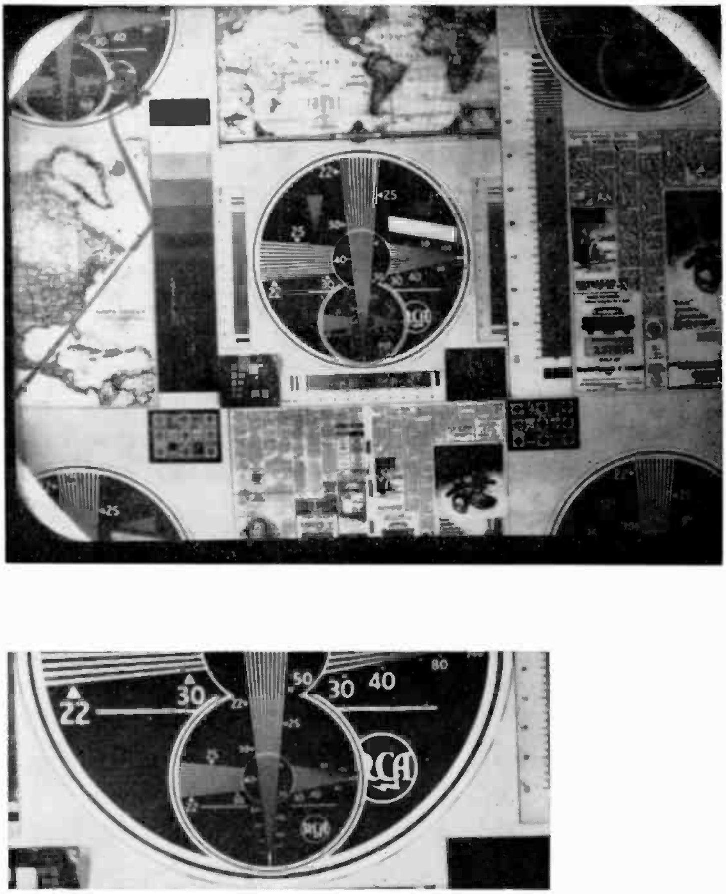

Fig. 8—A picture of the display monitor showing the general capability of the silicon RBV tube. Limiting resolution observed on the monitor was 60 lines pairs per millimeter. Shown below is an enlargement of an area of the top photograph.

* The picture was taken from the display monitor by O. H. Schade, Sr., in his laboratory setup.

4.2 Signal-to-Noise Ratio

Although the silicon RBV was designed to operate in the return-beam mode, it may also be operated in the target readout mode. The return-beam mode, however, provides a better signal-to-noise ratio, especially at wide bandwidths and at low signal levels. The return-beam mode also minimizes problems of shielding and of maintaining low capacitance in the readout circuit. The choice of operation mode depends upon the particular application. Some analysis of the advantages of each mode relative to signal-to-noise considerations is provided in this section.

Eq. [2] was developed for the return-beam mode to show the expected ratio of peak-to-peak signal to rms noise measured in the black—the worst case.

$$S/N_{(\text{R-B mode})} = \frac{i_p}{\sqrt{2ei_n\left(1+\dfrac{\delta}{\delta_1(\delta-1)}\right)B}}. \qquad [2]$$

In this equation, i_p is the signal photocurrent at the target, i_n is the beam current from the electron gun, δ_1 is the secondary emission ratio at the first dynode, δ is the secondary emission ratio of each of the other dynodes (all assumed to have the same value), e is the charge on the electron, and B is the bandwidth.*

It is apparent that to maximize the signal-to-noise ratio, the beam current should be chosen as small as possible. Corresponding to the experimental condition, the beam current is taken as that value just sufficient to discharge the highlight signal level, represented by the target signal current, i_p. Not all of the beam current is available to discharge the signal; some is absorbed by the mesh and some is wasted because it is scattered back from the target. Let M represent the transmission of the mesh (40% in the case of the 1500 inch^{-1} mesh); let A represent the fraction of the electrons striking the target that are absorbed and serve to discharge the signal. (An average value of A was found to be of the order of 0.36.) The required beam current is

* No account is taken in Eq. [2] of the scan efficiency; it is assumed to be 100%. If the scan efficiency is η, the bandwidth would have to be increased to B/η. The beam current likewise would need to be increased to i_n/η. Similarly, the signal current would be increased to i_p/η. These three increase factors will all cancel in their application to Eq. [2], provided the signal current is measured dynamically and not on an average dc basis. In this discussion, it is assumed that Eq. [2] applies without modification.

therefore,

$$i_n = \frac{i_p}{A\,M}. \qquad [3]$$

Using this criterion for the magnitude of the beam current, Eq. [2] may be rewritten as follows:

$$\mathrm{S/N}_{(\text{R-B mode})} = \left[\frac{i_p\,A\,M}{2e\left(1+\dfrac{\delta}{\delta_1(\delta-1)}\right)B}\right]^{1/2}. \qquad [4]$$

This expression for S/N was developed to include the first-dynode gain, because frequently in return-beam camera tubes the first-dynode gain is lower than the gains of subsequent stages. Values of 2 and 3 were assumed for δ_1 and δ, respectively, for purposes of comparing theoretical and experimental relationships. There is some evidence to suggest that the value for δ_1 is optimistic. This point will be discussed later.

In the target mode, the signal-to-noise ratio is limited by the noise figure of the amplifier. In this case, the signal-to-noise ratio may be expressed as follows:[4]

$$\mathrm{S/N}_{(\text{target mode})} = \frac{R\,i_p}{\sqrt{4kT}\sqrt{(R+R_t)B + \dfrac{4\pi^2}{3}C^2R^2R_tB^3}}, \qquad [5]$$

where k is Boltzmann's constant, T is the absolute temperature, R is the value of the coupling resistance, R_t is the equivalent noise resistance of the amplifier input, C is the total capacitance of the tube and associated input circuitry, and B is the bandwidth. For wide bandwidths and fairly large values of R, Eq. [5] reduces to:

$$\mathrm{S/N}_{(\text{target mode})} = \frac{i_p}{\left[(4kT)\dfrac{4\pi^2}{3}C^2R_tB^3\right]^{1/2}}. \qquad [6]$$

In tests made in the target mode, the value of C was measured to be 87 pF, of which 60 pF were attributed to the tube, a cooling plate adapted to the faceplate of the tube, and the coaxial cable. The balance was that of the amplifier. The equivalent noise resistance of the amplifier* used was 64 ohms.

The choice of operating mode for best signal-to-noise performance may be made by comparing the signal-to-noise values as functions of i_p and B from Eq. [4] and [6]. For the parameter values, as indicated above, it may be shown that the return-beam mode is preferred whenever

$$i_p/B^2 < 27 \text{ nA}/(\text{MHz})^2. \qquad [7]$$

This relationship is explored in Fig. 9. A line showing the maximum target signal current that can be accommodated by the storage capacitance of the target is included to complete the delineation of usable and preferred operating ranges. This line was calculated assuming a 1 inch $\times$ 1 inch target having a total capacitance of 26 nF, a 10-volt maximum target signal-voltage excursion, and a scan time in seconds equated to $2/B$, with the bandwidth in MHz. Note that this relationship between scan time and bandwidth implies a capability for $(2000)^2$ picture elements per scan. The operating ranges shown in Fig. 9 are illustrative only, and will change with different picture element capability and target size. It may be stated that in general the return-beam mode is preferred for low target currents and large bandwidths.

The theoretical signal-to-noise ratios in the return-beam mode (Eq. [4]) and in the target mode (Eq. [6]) are plotted in Fig. 10 as a function of target signal current, i_p, for a bandwidth of 10.5 MHz. Also shown are experimental data for both cases. Signal values are peak-to-peak measured at a low spatial frequency; noise values are rms measured in the black. The data for the target mode is artificial in that pickup degraded the measurements and could not be eliminated in the limited experimental program. The noise value was, therefore, taken as that with only the target preamplifier and processing amplifier operating.

The top line of the data in Fig. 10 represents a hypothetical signal-to-noise characteristic assuming no noise is contributed by the

* The preamplifier, characterized by a low-dynamic-impedance FET front end, was designed by R. L. Rodgers, 3rd, of RCA, Lancaster, Pa. It should be noted that the target readout amplified was at a disadvantage because of the rather large input capacitance as noted. By careful design, this capacitance could be reduced to perhaps 60 *pF* total, which would improve the target-mode signal-to-noise ratio accordingly.

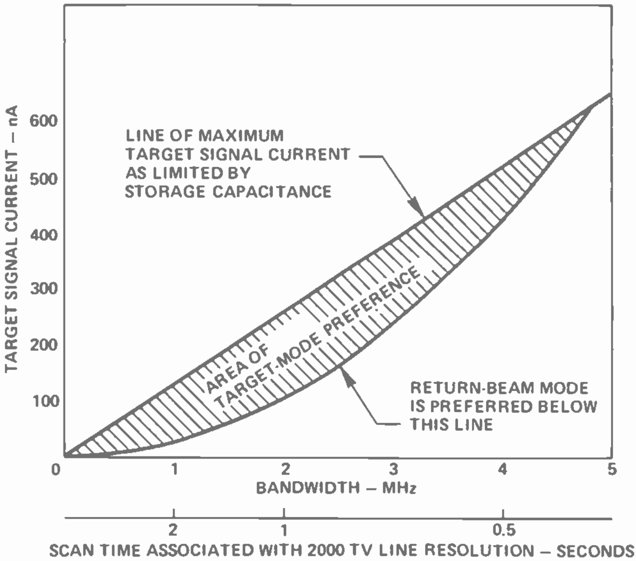

Fig. 9—Approximate ranges of preference for target mode and return-beam mode.

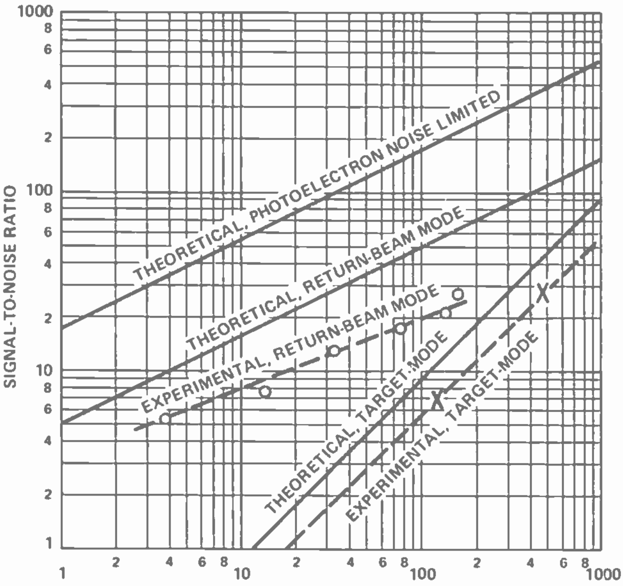

Fig. 10—Calculated and measured signal-to-noise ratios for the silicon RBV tube operated in the return-beam mode and in the target mode. Bandwidth is 10 MHz. Also shown is the calculated signal-to-noise ratio for the photocurrent only with no loss assigned to the readout mechanism.

readout mechanism. In this case, the noise is chosen as the photoelectron noise in the white signal, which varies as the square root of the signal level.

It may be observed that the measured S/N in the return-beam mode is a factor of 2 or more poorer than predicted. Two possible explanations are suggested.

(1) The effective gain of the first dynode may have been substantially lower than estimated because: the electron-optical efficiency between the first and second dynodes is poor; there are obstructions of the mesh and support members at the entrance to the second dynode; no cesium activation of the first dynode is used in this tube as in the typical image orthicon; a fraction of those electrons striking the pinwheel second dynode are lost because of the inefficiency of the pinwheel design.

(2) The modulation factor–defined as the difference between white and black levels of current divided by the black level current–was significantly lower as measured in the output lead of the multiplier than that evaluated for the current entering the first dynode. This difference implies a spurious source of current in the black that would degrade the signal-to-noise ratio. Efforts to identify the source of this extra current were unsuccessful.

4.3 Lag Phenomena

In the typical photoconductor used in vidicons, there are two mechanisms–photoconductive lag and capacitive lag—that prevent full readout of the signal in the first scan. The former is caused by the trapping of charge carriers in the photoconductor. Capacitive lag is associated with the rate at which the electron beam neutralizes the charge stored by the target.[5]

In the RBV tubes having ASOS photoconductor targets, special erase techniques, such as multiple-erase frames, are used to overcome the effects of photoconductive lag. For the silicon target, there is no photoconductive lag and one needs only to deal with the capacitive lag. The storage capacitance of the silicon-diode matrix target is approximately 4.5 nF/cm^2.

Capacitive lag results from the variation of the beam current that lands on the target as a function of the target surface potential. The beam current may be described approximately by $i = i_o e^{bV}$ for $V < 0$; and, $i = i_o$ for $V > 0$, where V is the target surface voltage relative to that of the thermionic cathode, and i_o represents the maximum beam current landing on the target. The constant, b, is inversely related to the breadth of the energy distribution in the electron stream. The larger the value of b, the less the capacitive lag. In an electron-optic arrangement providing unity magnification of the cathode aperture, one expects $b = e/kT = 10$ volt^{-1}, assuming the thermal emission velocity spread is preserved at the target. In this expression, e is the electron charge, k is Boltzmann's constant, and T is the temperature of the thermionic cathode. However, experimentally measured values of b for a typical vidicon run about 5 volts^{-1}. In the silicon RBV tube, the demagnification of the gun aperture as it is imaged on the target results in an increase in the axial energy distribution of electrons in the beam that directly affects the value of b. In this case, the values of b run between 1 and 2 volts^{-1}. Consequently, capacitative lag is somewhat larger than for an electron optic with unity magnification.

4.4 Sensitivity and Dark Current

The measurements of quantum efficiency on the silicon RBV indicated close agreement with published data for conventional silicon vidicons, especially if adjustments are made for the differences in antireflection coating practice. The silicon vidicon has an antireflection coating on the silicon target, which is suspended in vacuum; the silicon RBV has an antireflection coating between the silicon and the cement bonding it to the faceplate. No antireflection coating was used on the external faceplate surface.

Dark current was found to be of the order of 100 nA at room temperatures for a 1×1 inch^2 raster and a target voltage of 8. This figure is about an order of magnitude greater than the dark current observed in the typical one-inch silicon vidicon tube because the dark current tends to be proportional to the number of diodes. In order to minimize the dark current during the measurement program, the faceplate was cooled to 10°C.

4.5 Mode of Operation

Although the silicon RBV is intended for a single-frame, slow-scan operation, the tube can also be operated in a conventional TV scan mode. However, in order to realize even 2000 TV lines limiting resolution per picture height in a square raster of one-inch diagonal, the bandwidth would have to be 60 MHz for a 1/30th-second scan cycle. The signal current measured at the target would have to exceed 500 nA in order to realize sufficient signal-to-noise ratio to provide the desired resolution with reasonable contrast rendition. For an f/2 lens with 80% transmission, a scene reflectance of 60%, the illumination level to produce this target current would be about 5 foot candles assuming infrared radiation is excluded with a Schott (JANAer) KG-3 filter 5.5 mm thick.* This level of illumination corresponds to that just after sunset. At this condition, there would be some objectionable capacitive lag—about 20% in the third field (0.050 second).

A more favorable operation of the tube would be a slow-scan mode similar to that of RBV applications such as in the ERTS (Earth Resources Technology Satellite) satellite: expose-read-erase. The full resolution capability of the tube can be realized and good signal-to-noise can be achieved provided the target is exposed to a reasonable charge level. Typical read-and-erase cycle time for such an application might be less than 1s. (The ERTS system uses a 14.5-s prepare and a 3.5-s read time.)

In slow-scan operation, however, the tube must be cooled to reduce the dark current. At room temperature, dark current is of the order of 100 nA (for a 1 × 1 inch^2 raster) so that in a period of less than one second the dark current would discharge the target almost completely for the typical target-storage capacitance of 26 nF (per square inch). For a reduction in temperature to −10°C, the dark current should be about 10 nA, which is of minor consequence.† Assume a target exposure of 0.02 foot-candle-second using the KG-3 filter to exclude the infrared. A target voltage shift of approximately 5 volts would be developed. For a 0.5-second read time, the target current would be 250 nA. Signal readout efficiency (first scan) would be of the order of 95%. The residual signal is easily removed by an erase scan in the dark. If desired, the erase cycle can be shortened by increasing the beam current. Experimental erase cycles of ⅛th second were found to be adequate. Bandwidth requirement for 3000 TV lines in the one-inch square raster would be 9 MHz; the return-beam mode would be indicated. If even longer read times were utilized with lower bandwidths, the target-read mode would be indicated for signal-to-noise reduction (see Fig. 9).

5. Conclusion

A new, rugged, silicon vidicon tube was developed using a high-density silicon-diode array and a high-resolution, electron-optic arrangement. Resolution of 60 line pairs per millimeter was achieved. The tube was designed with a multiplier section for return-beam operation that

* Without the infrared excluding filter, the sensitivity would be substantially greater—a factor of 5 in the case of tungsten radiation.

† A cooling mechanism for the RB faceplate exists for the ERTS RBV camera design. It uses thermal electric cooling elements that provide about 10°C differential between faceplate and ambient.

provided better signal-to-noise values than were obtained in target readout, especially for wide bandwidths and for moderate or low-signal currents. Lag was found to be somewhat higher than in standard silicon vidicon tubes because the electron-optic design increased the divergence of axial electron-beam velocities. Other properties of the tube such as high quantum efficiency and wide spectral response were those expected for silicon targets. Dark current was fairly large because of the large number of diodes in the high-resolution target, but it could be reduced by cooling.

Improvements and modifications of the silicon RBV tube could be made. Although the experimental targets accommodated a square raster 0.7 inch on a side, a target providing for a one-inch square raster could readily be achieved; in fact, it is anticipated that a target having a useful two-inch square area could be produced to fit into the 4.5-inch RBV format. The first-stage gain and electron optic design could be improved to yield better signal-to-noise ratios. Improvements could also be made in the electron-gun design to minimize radial velocities at the exit aperture. Initial experiments indicated that a tetrode gun may provide the desired improvement.

Applications which suggest themselves are satellite TV, real-time airborne surveillance, and high-resolution TV reproduction of hard copy such as maps and photographs.

Acknowledgment

The authors wish to acknowledge particularly the contributions of C. P. Hadley and T. W. Edwards of RCA Electronic Components and G. A. Beck and J. J. Hawley of the RCA Astro-Electronics Division, who assisted in the development and measurement program for the silicon return-beam vidicon.

References:

[1] O. H. Schade, Sr., "Electron Optics and Signal Readout of High-Definition Return-Beam Vidicon Cameras," **RCA Rev.**, Vol. 31, pp. 60-119 (1970).
[2] RCA Developmental Types C23061A and C74137A, respectively.
[3] M. H. Crowell and E. F. Lubuda, "The Silicon Diode Array Camera Tube," **Bell Sys. Tech. Jour.**, Vol. 48, pp. 1481-1528 (1969).
[4] V. K. Zworykin and G. A. Morton, **Television** (Wiley, 1940), p. 434.
[5] R. W. Redington, "The Transient Response of Photoconductive Camera Tubes Employing Low-Velocity Scanning," **IRE Trans. on Elec. Devices**, ED-4, pp. 220-225 (1957).

An Experimental Study of High-Efficiency GaP:N Green-Light-Emitting Diodes*

I. Ladany and H. Kressel

RCA Laboratories, Princeton, N. J.

Abstract—A study of techniques for preparing n-type material and junctions that yield the most consistently high diode-efficiency values has highlighted the role that Ga vacancies and/or associated defects play in reducing the green luminescent efficiency of n-type GaP. It has been shown that junction formation at high temperatures in a process where the n-to-p transition occurs without removing the substrate from the furnace yields devices superior to those obtained by diffusion or double epitaxy in the conventional manner previously used for GaP junction formation. Under pulsed excitation (to minimize junction heating) an efficiency value of 0.7% has been achieved at 200 A/cm^2 with mesa diodes. At lower current densities (33 A/cm^2), a value of 0.2% has been achieved under dc operation. These values are the highest reported to date under pulsed and dc modes of operation for double epitaxial diodes using a process consistent with the use of large-area GaP substrates. Structures containing (AlGa)P-GaP heterojunctions were investigated with the aim of improving the diode efficiency. The results were disappointing in all cases in that the efficiency was lower than in homojunctions. Both Be and Mg have been studied as possible substitutes for Zn. There appears to be no obvious advantage to their use at this time, although the reduced red emission at room temperature observed when Mg is used may have special applications.

* Research partly supported by the Langley Research Center of NASA, Hampton, Virginia, under Contract NAS1-10696.

1. Introduction

The near-bandgap radiation of GaP, which peaks at about 5600 Å, is very close to the wavelength of maximum eye response. This makes GaP potentially the most useful of all visible semiconductor light sources. Research on GaP light-emitting diodes (LED's) began over a decade ago, but useful green emission has only been obtained since the use of liquid-phase epitaxy[1] to grow this type of material[2] and of nitrogen to enhance the diode near-bandgap radiation at room temperature.[3]

Despite the extensive prior research on GaP materials, it has proved difficult to reproduce high-efficiency green-emitting LED's. This paper is concerned with a study of some important factors affecting the diode efficiency at room temperature. We have studied diodes made by diffusion and epitaxial growth under a variety of liquid-phase synthesis conditions. An improved single-step growth process is described that yields diode efficiencies as high as 0.7% at 200 A/cm^2 on large-area melt-grown substrates, a value significantly higher than previously reported for material of this type.

2. Basic Materials and Device Properties

2.1 Preparation and Properties of n-Type Material

It is well established that nitrogen is needed to obtain the highest possible room-temperature green-emission diode efficiency,[3] but the correlation between the nitrogen concentration in the solid and the efficiency is not easily established because: (a) some N is always present in the material (even without its addition to the growth solution); (b) it is difficult to measure the N concentration in the relevant regions of the diode, and (c) other factors that can depress the diode efficiency can mask the effect of nitrogen.

Some major factors that can degrade the diode efficiency are (1) vacancies and associated impurity complexes that in GaAs are known to be nonradiative centers and can be expected to behave similarly in GaP, (2) contaminants such as Cu, and (3) defects at the p-n junction interface (dislocations and associated precipitates) that result from the lattice parameter mismatch due to difference in the impurity concentration.*

Thus, despite the fact that the radiative efficiency of the material (as measured by photoluminescence) in the *bulk* of the n- or p-side of

* X-ray topographs have indeed shown that such dislocations exist (Ref. [4]).

the junction is high, the diode efficiency can be low because of non-radiative recombination in the p-n junction interface region. This is particularly significant in GaP, because the minority-carrier diffusion length is so short[5]—0.2 to 0.5 μm—that the bulk of the carriers actually recombine very near the p-n interface.

The relative contributions of the p- and n-sides of the junction to the green emission will depend on the doping in the two regions. It appears from visual observation and from a comparison of the photoluminescence (PL) from the n-side of the junction and electroluminescence (EL) that much of the green emission occurs in the lightly doped n-side of the junction in the present devices.† Fig. 1 shows a

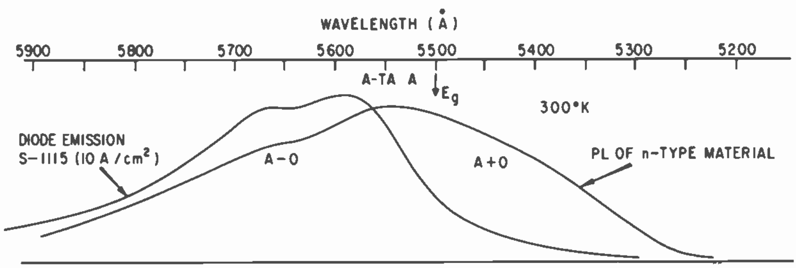

Fig. 1—Photoluminescence of a high-efficiency n-layer and electroluminescence from a diode incorporating that layer.

comparison of the diode EL and PL from the n-side layer of the kind used in our double epitaxial diodes. While the major features are similar, note that the high-energy side of the emission is reduced in the EL spectra because of selective internal absorption in the diode. The PL spectra have been extensively described in the literature[3] and we will only note some of the key features. The relative magnitudes of the 5540-Å line and the 5650-Å line depend on the nitrogen concentration in the solid, with the intensity of the 5650-Å line increasing (relative to the 5540-Å line) with increasing N concentration. Thus, in the presence of a high N content, the emission of the diode is no longer purely green but is closer to yellow.

In addition to the green emission, the spectra include some red emission at room temperature, which is not usually identical for the n-type PL and the EL. In the diodes the red EL band is centered at about 6900 Å and is identical to the Zn-O pair recombination band. It

† In any case, the Zn diffusion during and after growth places the junction into what was originally the n-type layer; thus its initial quality is always of great importance.

is due to residual oxygen in the p-type grown material. The PL band of the n-type material, on the other hand, is broader and shifted further into the infrared, being centered at ~7200 Å. This band is attributed to a complex center associated with Ga vacancies. The relative PL intensity of the 7200 Å red band compared to the green band at 300°K was found to qualitatively correlate with the green emission efficiency of the diodes made in that material. The diodes made from n-type material with the highest PL ratio of green-to-red intensities at 300°K were generally the most efficient ones. This ratio was varied by the proper choice of preparative method. Using bulk "liquid-encapsulated" (LEC) material for substrates, n-type layers were grown by two distinct methods: Group I material was grown in a "quasi" sealed crucible, while Group II material was grown under flowing hydrogen in an open-tube system.

The quasi-sealed crucible is shown in Fig. 2. It consists of a vitreous carbon boat inside an Al_2O_3 tube fitted with an Al_2O_3 plug.

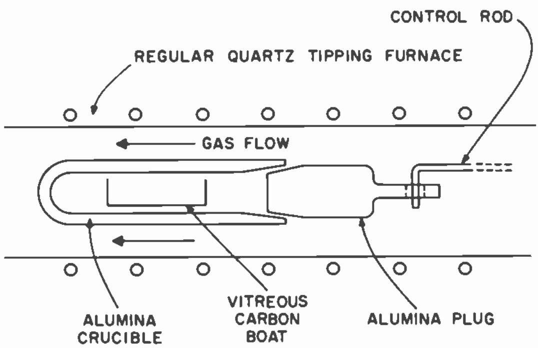

Fig. 2—Quasi-sealed crucible.

The crucible can be manipulated from outside the furnace, thus allowing the atmosphere surrounding the solution and wafer to be controlled. In the open-tube method for Group II material a conventional tipping furnace was used with a boat containing a vitreous carbon liner. Palladium-diffused hydrogen was continuously flowed over the solution.

The PL characteristics of Group I and Group II materials differed significantly. Group I material had a low relative PL efficiency at room temperature with mostly long wavelength (7200 Å) emission, while Group II material had a much higher efficiency with the emission concentrated in the green. The EL obtained from a diode where a p-layer was grown on Group I material had very weak green emission with the Zn-O red emission from the p-region of the diode dominating. Diodes made from Group II material, on the other hand, had enhanced green emission that overshadowed the red emission.

Inefficient n-type layers similar to Group I material were also obtained by restricting the flow of hydrogen in the open-tube system during growth. The similarities in the results obtained are attributed to the fact that in both cases the predominant vapor series (phosphorus) is kept at a higher level than under flowing hydrogen condition. At the growth temperature, the partial pressure due to P_2 (and P_4) is larger than the partial pressure due to Ga. Thus GaP decomposes to give P_2 (or P_4) in the vapor,[6] which affects the Ga vacancy concentration in the solid. In a stagnant atmosphere or in a sealed crucible, where the pressure P_2 increases, more Ga vacancies are generated than in a stream of H_2 where the P_2 is swept away.

We have tested this model by another experiment in which the P_2 pressure was reduced. A nitrogen-doped layer was grown in a sealed crucible as before, but one end also held a reservoir of Ga to trap the phosphorus vapor. At the end of the run, GaP platelets were evident in the Ga reservoir, as expected, and the resultant layer PL exhibited Group II (open-tube) behavior with the long-wavelength IR contribution weak and the green emission strong.

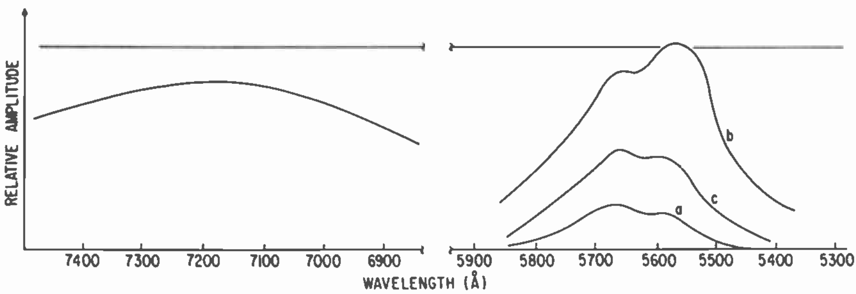

Fig. 3—(a) Photoluminescence of an n-layer grown in a sealed crucible; (b) the same layer after vacuum anneal; and (c) the same layer after further anneal in phosphorus ambient.

Annealing studies also suggest that recombination centers associated with Ga vacancies are formed. A Group I epitaxial layer, whose PL spectrum is shown in Fig. 3(a), was annealed in *vacuum* at a temperature of 550°C for 18 hours with a relative reduction in the low energy band (Fig. 3(b)). However, an anneal of this material in a *P ambient* again increased the low energy-band intensity (Fig. 3(c)).

Thus, we find that the best layers, from the point of view of PL results, are obtained under a low P pressure, and the worst ones are obtained under conditions resulting in high P_2 (or P_4) partial pressures. It is irrelevant whether the solutions are confined, thus trapping P_2 or P_4, or whether we reduce the hydrogen flow rate and thus build up the phosphorus partial pressure. Furthermore, we find that these effects are reversible in that annealing the material in vacuum reduces the low energy band; the low energy band can be enhanced by annealing in a phosphorus-rich ambient. It is plausible, therefore, that excess phosphorus pressure results in the generation of point defects, presumably connected with Ga vacancies, which manifest themselves by a broad emission band centered at ~7200 Å and by reduced green emission efficiency. Material having such emission also yields inefficient diodes.

The sensitivity of the material to the P pressure provides a clue to the poorly understood reason for the commonly observed variability in efficiency from standard runs where the P pressure is only determined indirectly. The present results suggest that the phosphorus pressure should be directly controlled in order to stabilize a heretofore ignored variable.

Another important problem concerns the incorporation of nitrogen into the layers, which presumably occurs via the nitrogen dissolved in Ga. The most controllable method used in the present work consisted of placing a mixture of GaP and Ga, the so-called "melt", in the quasi-sealed crucible together with a small quantity of crystalline GaN, and then raising the temperature to 1060° to 1080°C for a few minutes. The melt was then transferred to another boat and used for the open-tube growth of the n-type layer. Another useful technique consists of baking out the melt at 600°C, adding nitrogen by flowing NH_3 through the furnace,[3] and then proceeding to the LPE growth. This avoids the transfer of solutions with the possibility of contamination.

The nitrogen concentration in the GaP was determined by optical absorption.[7] Typically, the N concentration was 4×10^{18} cm^{-3} in the materials studied as determined by the absorption method. The n-layer electron concentration was usually in the 2-6 $\times 10^{16}$ cm^{-3} range without intential donor doping.

Since the solubility of N in GaP is high[3] (~10^{19} cm^{-3}), it would appear that the highest possible doping should be used in order to enhance the green luminescence, particularly since the addition of N does not increase the free-carrier concentration and does not, therefore, lead to nonradiative Auger recombination. However, excessive concentrations of N lead to disturbances in growth, and the formation of other crystal structures (Fig. 4) indicating the presence of new phases involving nitrogen. For the above reason, as well as because of the high absorption due to nitrogen in GaP, optimum nitrogen concentration must be somewhat below that set by the solubility limit, the exact value depending also on the diode configuration.

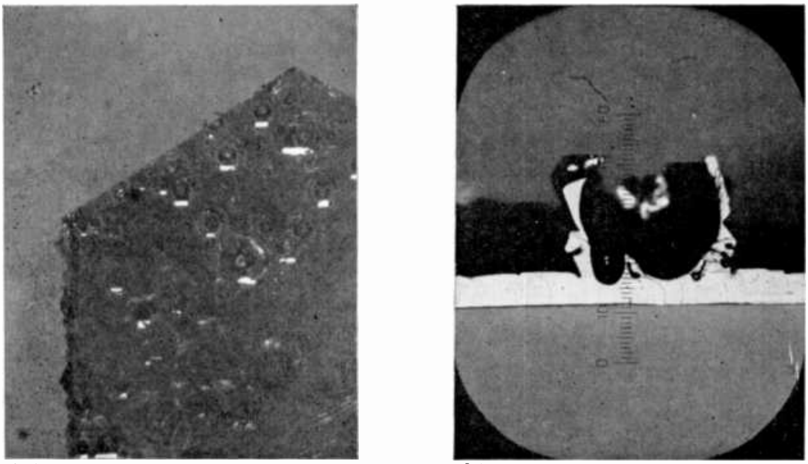

(a) (b)

Fig. 4—Growth disturbances due to excess nitrogen in the Ga solution. In photograph (a), numerous hexagonal "caverns" are seen to grow out of the wafer surface. Photograph (b) shows a cross section through such a "cavern." (Scale 0.001 cm/division.)

2.2 Preparation of p-n Junctions

In order to study the influence of the junction formation method on the diode performance, we have prepared three different types of junctions using similar n-type regions prepared as discussed above. The junctions were formed by zinc diffusion, two-step LPE, and single-step LPE. The dc efficiencies of the diodes obtained were compared at ~ 10 A/cm^2 using a standard assembly technique in which a 0.25×0.25 mm chip was provided with alloyed contacts on portions of the bottom and top surfaces, mounted on a TO-18 header, and covered with a plastic dome. The green emission was separated from the red emission by the use of a Corning 4-97 filter, while the red emission was separately measured by the use of a 2-58 filter. A calibrated Si solar cell was the detector, and all diodes were measured in an integrating sphere. Results are shown in Table 1.

Table 1—Efficiency of Diodes Similarly Assembled

Junction Type	Standard Efficiency* (green only) (%)
Diffused	0.03
Two-step	0.045
Double-bin	0.14

* "Standard" efficiency is the dc value of encapsulated diodes having planar geometry and alloyed contacts, at ~ 10 A/cm^2.

1. Zinc-Diffused Diodes—Zinc was diffused into Group II LPE layers in sealed ampoules using various schedules, with all of them giving similar results. A typical schedule consisted of 1 mg/cm^3 of ZnP_2 at 850°C for 1.5 hours, which yielded a junction depth of 7 to 8 μm. Efficiencies for these diodes were typically 0.03% at 10 to 40 A/cm^2.

2. Two-Step LPE—Two-step LPE diodes were made by growing a Zn-doped layer on a previously prepared nitrogen-doped n-layer of the Group II type. The p-layer was grown from a solution containing 5 g Ga, 0.095 g GaP, 10 mg Zn, at a tipping temperature of 960°C and a cooling rate of 20°C/minute. The green diode efficiencies were typically 0.045% at ~10 A/cm^2. For comparison, we note that diodes made using Group I n-layers had green efficiency values of only 0.001-0.002%.

3. Single-Step, Double-Bin (DB) Epitaxy—The double-bin growth was carried out in a special quartz and vitreous carbon boat shown in Fig. 5 using the basic design of Nelson.[8] Once the boat was set on the desired cooling schedule, the wafer was moved from bin to bin to produce the layers. The Ga solutions were first prebaked at 1040°C in flowing palladium-diffused hydrogen. The solution used for the n-type layer

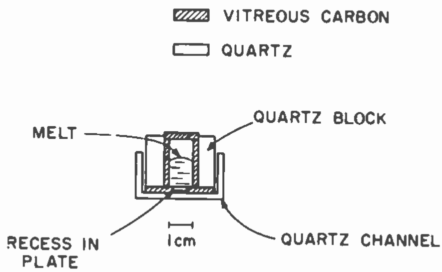

Fig. 5—End-view of double-bin boat used in the growth of GaP layers. The slide direction is perpendicular to the page.

was saturated with nitrogen in a separate heating step before being placed in the bin. The Ga solutions contained Zn for the p-side with usually no deliberate donor doping for the n-side. The cooling rate was 7.5°C/minute starting at 1020°C, and the p-n junction was formed at 980°C. The n-type layers, typically 20 μm thick, had a carrier concentration in the low 10^{16} cm^{-3} range as determined from capacitance–voltage measurements. The residual donor impurities were probably sulfur or silicon, both of which are known to be common contaminants in GaP. The p-region hole concentration was $\sim 5 \times 10^{17}$ cm^{-3}. These double-bin diodes showed the highest "standard" efficiency of all three types, about 0.14% at $\sim$10 A/cm^2.

The reason for the improved green efficiency of the DB diodes compared to other types is believed to be the better material quality of the p-n junction. In part, this may be the result of some degree of compensation on the n-side of the junction due to Zn intermixing in the solutions, as a result of which the *impurity* concentrations on the p and n-sides of the junction are very nearly equal. Such a condition would provide a lower interfacial defect density because of reduced lattice mismatch at the junction. Since the diffusion length in GaP is so short, the improved interfacial crystalline quality will be reflected in a higher overall efficiency. It is of interest to note that in contrast to two-step diodes, the DB devices do not improve by post-growth annealing. If we assume that such anneals help by reducing junction defects, this result suggests that DB material already has as low a defect density as can be expected.

It should be noted that diodes with efficiencies approaching those obtained by the above DB process have been obtained by a modified method where the p-n junction is also generated at high temperature. This technique consists of first growing an n-type layer, then adding Zn to the solution by vapor doping the hydrogen stream, which results in the growth of a p-type layer.

A number of runs were also made using dislocation-free solution-grown platelets for the substrates. No significant correlation was found between efficiency and substrate type.

Occasionally a DB run was made that produced material with very low EL efficiency. A cleaved and delineated profile from such a wafer is shown in Fig. 6, which illustrates a multiplicity of junctions due to inadvertent Zn diffusion. (A desirable profile from a good wafer is shown in Fig. 7.) Since the p-type GaP layer is grown after the n-type layer, the p-solution is heated to the high temperature required for the n-solution growth, and the zinc vaporizes and may counterdope

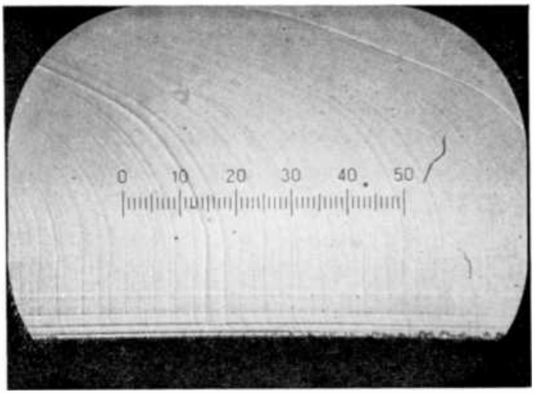

Fig. 6—Multiple junctions produced inadvertently in DB growth by uncontrolled Zn diffusion (scale 0.001 cm/division).

the weakly doped n-solution. One way of eliminating this problem is to reverse the order and grow the p-layer first. Indeed, several reverse-order runs were made showing no contamination, but the efficiency, so far, has been lower than in the p-on-n case. The best answer thus appears to be a careful control of the heating cycle, a careful control of the zinc content in the p-solution, and good boat design to reduce the chance of zinc cross-contamination.

2.3 Other Acceptors in GaP: Be and Mg

In general, a suitable acceptor should have a high solubility in GaP, should not form precipitates, should dissolve readily in Ga, and should

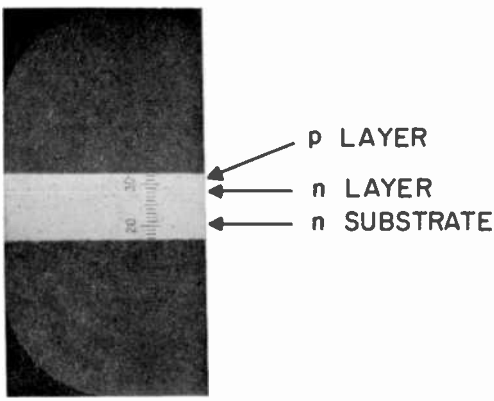

Fig. 7—Delineation of a high-efficiency DB junction.

have a low vapor pressure and a moderate diffusion rate. In several respects Be meets these requirements, but it diffuses too rapidly and its solubility in Ga is low. It can, however, be used to form p-n junctions, and the ones that we have prepared did not differ in efficiency from those achieved with Zn in two-step growth.

With regard to Mg, its vapor pressure is lower than that of Zn and the diffusivity is also expected to be lower. A number of runs were made using Mg additions to a Ga-GaP mixture that was used as the solution for growing p-layers on a previously grown nitrogen-doped layer. It was found that the solution is altered in appearance, similar to the effect of adding aluminum to the melt. At the end of a run, one often sees floating on the Ga surface bright green crystallites that rapidly disappear on exposure to air. This technique does not appear to affect the growth process however, and can produce very adequate diodes. In the limited number of runs made, the "standard" diode efficiency obtained was ~0.03%.

One interesting property of Mg is that no Mg-O pair emission analogous to the Zn-O pairs is observed at room temperature; these diodes do not, therefore, have any red emission. The stringent requirements on solution purity concerning oxygen contamination can therefore be relaxed.

2.4 GaP-(AlGa)P Heterojunctions

The room-temperature lattice constants of GaP and AlP ($E_g = 2.45$ eV) are close (5.450 Å for GaP versus 5.462 Å for AlP), and it appears attractive to investigate simple possibilities to improve the efficiency of the GaP diode emission by:

(a) taking advantage of the (AlGa)P-GaP heterojunction in order to improve the injection efficiency of holes into n-type material, and

(b) providing a window over the GaP homojunction in order to improve the extraction of the junction radiation.

Several attempts were made to utilize scheme (a), but the results were not encouraging. In some cases, it is possible to understand the reason for this; for example, as shown in Fig. 8, an $Al_xGa_{1-x}P$ p-type layer was grown onto an n-type GaP layer ($x \approx 0.5$). An etch of a cleaved edge shows a line of what appear to be decorated dislocations, and the junction emits very little light.

A more successful approach consisted in placing the junction in a graded region, i.e., one where the Al-to-Ga ratio varies smoothly. Al-

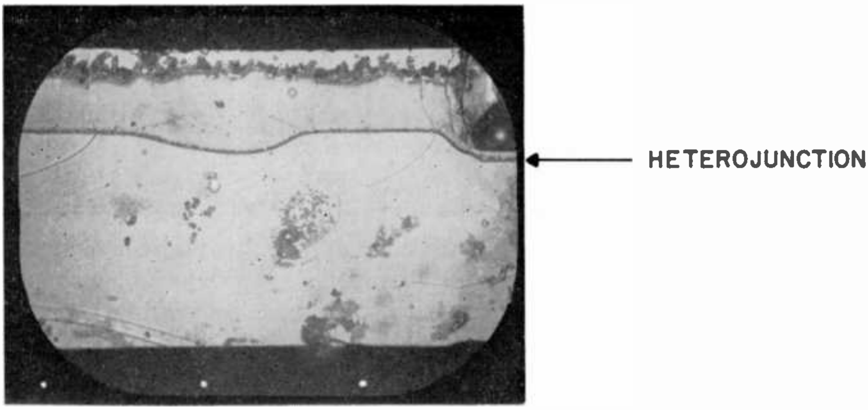

Fig. 8—Heterojunction between (AlGa)P and GaP "decorated" with impurity precipitates.

though fairly good light emitters were made, and the possibility of eventually obtaining superior performance could not be ruled out, we have not found the added complexity to be justified in the result.

Attempts made to place a window near the GaP homojunction (as suggested in (b) above) also failed to yield higher-efficiency diodes. Two explanations suggest themselves: (1) the strain due to the heterojunction affects the homojunction and (2) the internal light reflection at the refractive index discontinuity hinders the light emission. The second explanation gains some support from a microscopic examination of an emitting diode containing such a structure.

Fig. 9 shows a cross section of a heterojunction diode under forward bias. The large dark region is the substrate consisting of p-type

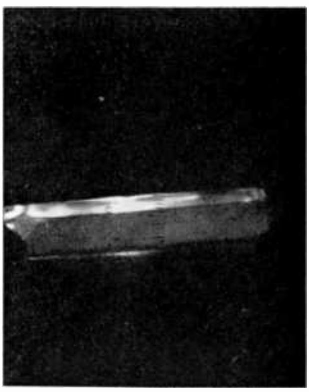

Fig. 9—Reflection from an internal heterojunction between GaP and (AlGa)P (see discussion in text).

GaP, the next layer is p-type (AlGa)P, and above the bright region is an n-type (AlGa)P layer. As can be seen there is an extremely sharp dividing line between the substrate and the (AlGa)P that may be due to the reflection at the heterojunction boundary.

The poor results obtained with the GaP-(AlGa)P heterojunctions may be the result of a greater than expected lattice parameter mismatch at the growth temperature. As the material cools to room temperature, strains can be frozen into the active region of the device, and dislocations can be formed to relieve the lattice misfit at high temperatures. As a result, the radiative efficiency of the GaP active region is greately reduced. Gallium phosphide efficiency is likely to be far more sensitive to the introduction of nonradiative centers than is a direct-bandgap compound like GaAs, because the radiative processes in GaP:N constitute but a small fraction of the overall recombination processes.

3. Device Fabrication

The basic device problem in LED's is that high external *efficiency* requires that the greatest possible number of photons be incident *normal* to the emitting surface, whereas high *brightness* requires all the emission to come from a small area. These two requirements conflict. While the efficiency can be greatly increased by shaping the diode into a hemisphere with a small circular junction area at the center, its brightness is low because the emission is spread out over the hemispherical surface. A high-brightness emitter is obtained from a planar diode with the junction parallel to the surface.* Under this condition most of the photons incident on the surface within the critical angle will be able to leave the crystal, with the distribution of radiation being approximately Lambertian. Photons outside the acceptance cone undergo multiple reflections and become absorbed due to the various loss mechanisms in the diode. Thus, diodes with planar geometry are bright but relatively inefficient, while diodes with dome geometry are efficient but not as bright.

It is generally advantageous to use a planar geometry for practical diodes and, within those limitations, to optimize the diode efficiency by the proper choice of metallization. Obviously if the contact blocks the light, the device output will suffer; but contact design depends on the resistivity of the material, because a high resistivity leads to current crowding under the contact. Thus, an optimum geometry depends on the materials parameters.

* We ignore edge emission, which, although the brightest, is only justified in special cases.

3.1 Diode Design for High External Efficiency

In Section 2, we compared the efficiency of diodes fabricated in a standard way in which a significant fraction of the internally generated radiation is reabsorbed. While such a comparison is useful in determining the best process for diode fabrication, it is of equal importance to determine as closely as possible the internal efficiency by studying diodes in which the coupling between the internally generated radiation and the outside is optimized without consideration of surface brightness. In fact, the highest previously reported GaP diode efficiency of 0.6% at 80 A/cm^2 for single epitaxial material on a solution-grown platelet[3] and 0.35% at 200 A/cm^2 for double LPE on LEC substrates was obtained with a diode in which emission was obtained from both the top and bottom of the diode by bonding a chip to a glass plate, or by suspending it by contacting wires in free space.

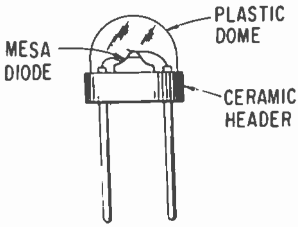

Fig. 10—Mesa diode construction used for the highest-efficiency diodes.

The diode construction we used to obtain the highest possible efficiency is shown in Fig. 10. The basic feature is a small p-side contact, a mesa construction, and a small n-side contact with the diode mounted on a reflecting white ceramic base. The whole diode is encapsulated in epoxy. Such diodes can be operated with dc up to a current density of about 30 A/cm^2; above that value, the current must be pulsed to eliminate efficiency loss due to junction heating. In the diodes that were measured pulsed, the green emission increased superlinearly with current up to at least 200 A/cm^2. The green emission L varied with junction current density J as follows

$$L = KJ^n, \qquad [1]$$

with n between 1.47 and 1.49, and K a constant. This superlinear dependence is indicative of the presence of nonradiative recombination processes, which do not increase as rapidly with current as the radiative ones involving the nitrogen centers.

The diode efficiency η at a given current density is given by

$$\eta = C \frac{L}{AJ} = \frac{CK}{A} J^{(n-1)}, \quad [2]$$

where C is a constant and A is the junction area. Thus, the diode efficiency increases with increasing current density in the range where the light output variation with current is superlinear.

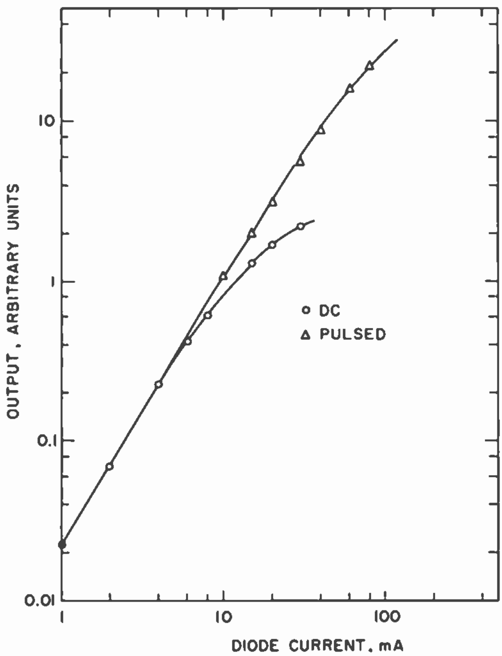

Fig. 11—Relative output from a high-efficiency DB mesa diode as a function of diode current.

Fig. 11 shows the light output as a function of the diode current of a DB diode optimized for emission efficiency with a better than 12:1 green-to-red emission ratio at $\geqslant 30$ A/cm². The value of n in this diode is 1.49. The absolute efficiency as a function of diode current density for the same diode is plotted in Fig. 12. The dc value is seen to saturate near 0.22%, whereas the pulsed value continues to climb to 0.7% at ~200 A/cm².

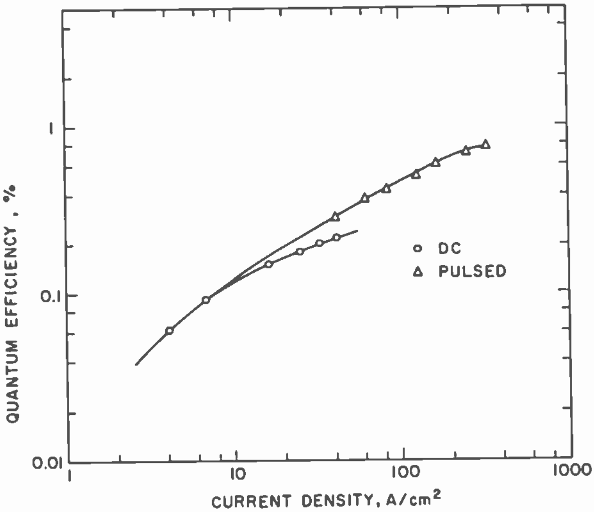

Fig. 12—Quantum efficiency as a function of current density of a high-efficiency DB mesa diode with minimal internal loss. The green/red emitted power ratio is greater than 12:1 for current densities $\geqslant$30 A/cm^2.

3.2 Numeric Displays

It appears likely that small LED displays will be unsurpassed in respect to brightness, cost, and ruggedness, as long as they are designed for close viewing by individuals. For such individual dsplays, a numeral size of 3 to 4 mm is adequate, as it allows easy reading at normal viewing distances. Two types of such small displays were made, one a diffused monolithic and the other an LPE segmented type.

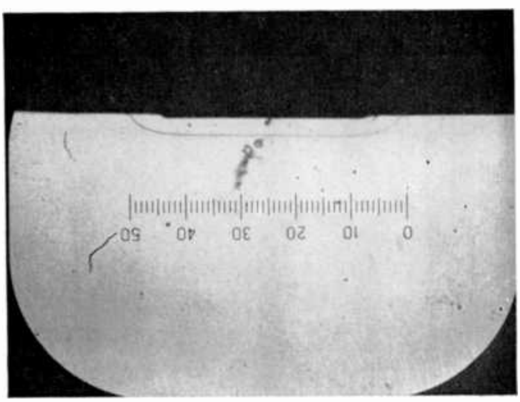

Fig. 13—Planar p-n junction Zn diffused through opening in an SiO_2, Si_3N_4 mask.

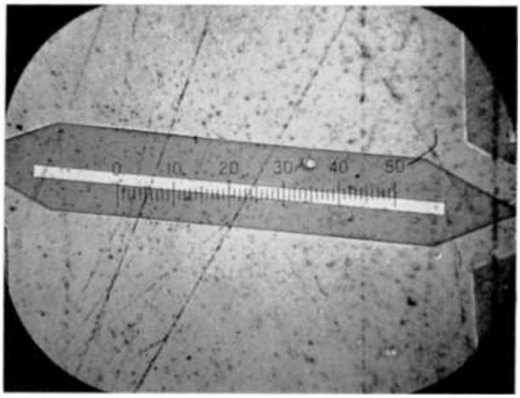

Fig. 14—A segment of the monolithic-diffused display. The center stripe is the top contact. Dimensions are 0.28×1.6 mm.

Monolithic-Diffused Display—The diffusion is carried out through a mask produced by deposition of SiO_2 and Si_3N_4 layers using photoresist techniques. Diffusion confined by the mask is illustrated in Fig. 13. Details of one segment of the display are shown in Fig. 14. The dimension of the display is 4×2.3 mm (Fig. 15). At present, the current requirement for these diffused displays is approximately 50 mA per segment, which is greater than that required for the discrete seven-segment display using epitaxially grown junctions.

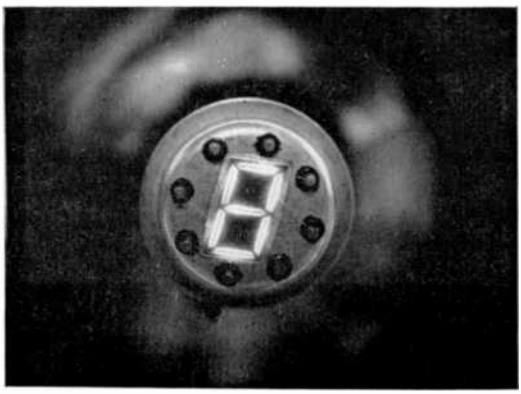

Fig. 15—Seven-segment monolithic display formed by Zn diffusion (4×2.3 mm).

Segmented Display—The design adopted uses plane geometry with reduced-area top contacts and partially reflecting contacts on the bottom. This is illustrated in Fig. 16, which shows the design of a typical 0.3×1.1 mm bar used in the seven-segment display. The bottom contact is an ohmic-contact ring around the periphery, with a reflector through the center; the top contact is an ohmic center bar.

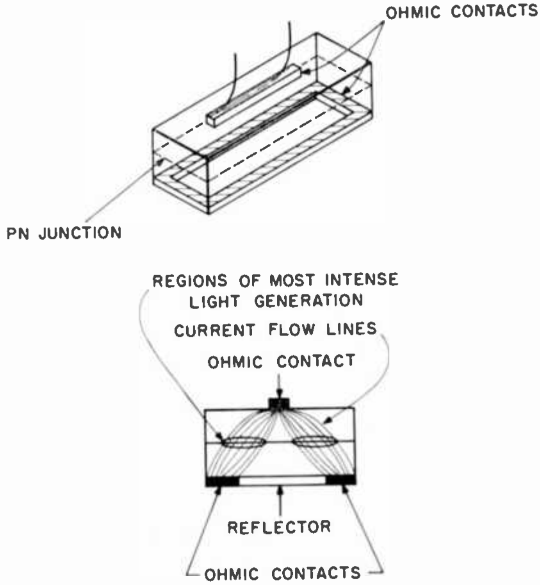

Fig. 16—Structure of segmented display using epitaxial junctions, showing contact arrangements and current flow.

The contact metal is evaporated over the whole wafer, and the pattern is obtained by photolithographic masking and etching. After a high-temperature alloying step, another layer of evaporated metal is applied over the bottom surface to serve as the reflector. The current flow and the region of maximum light generation is also shown in Fig. 16. The arrangement of the contacts is such that the current is forced outward from the center bar forming the top contact. In this manner, the brightest region is only slightly blocked by the contact, and light striking the bottom is reflected upward for a return trip. The display is assembled from seven bars bonded to a TO-5 header. Currents of 10-20 mA/segment are sufficient to produce adequate contrast and brightness.

4. Conclusions

An improved process for the fabrication of efficient green-emitting GaP diodes has been described. Under pulsed excitation (to minimize junction heating) an efficiency value of 0.7% has been achieved at 200 A/cm^2. At lower current densities (33 A/cm^2) a value of 0.2% has been achieved under dc operation. These are the highest values reported to date under their respective modes of operation for double-epitaxial diodes.

A study of the techniques for preparing n-type material and junctions that yield the most consistently high diode efficiency values suggests that Ga vacancies and/or associated defects play a critical role in reducing the green luminescent efficiency of n-type GaP. A useful method of obtaining good-quality material has been developed. We have shown that junction formation at high temperatures in a process in which the n-to-p transition occurs without removing the substrate from the furnace yields devices superior to those obtained by diffusion or double epitaxy in the conventional manner previously used for GaP junction formation. While the reason for the improvement is not definitively established, it is believed that reduced nonradiative recombination occurs in such diodes, possibly because of a better lattice constant match at the p-n junction. It is very significant that similar efficiencies have been obtained on diodes grown using large-area melt-grown GaP and on dislocation-free platelets grown from Ga solution.

The efficiencies of structures containing (AlGa)P-GaP heterojunctions were investigated. The results were disappointing in that the efficiency was lower than in homojunctions. The partial explanation may be that the lattice parameter mismatch at high temperatures is significantly worse than at room temperature, with the resultant formation of a high density of nonradiative recombination centers.

Both Mg and Be have been investigated as possible substitutes for Zn. There appears to be no obvious advantage to their general use at this time, although Mg may have special applications connected with the absence of red emission.

Acknowledgments

The skillful assistance of M. Dale Moyer and Dean Gilbert and useful discussions with F. H. Nicoll are gratefully acknowledged.

References:

[1] H. Nelson, "Epitaxial Growth from the Liquid State and Its Application to the Fabrication of Tunnel and Laser Diodes," RCA Review, Vol. 24, p. 603, Dec. 1963.

[2] K. K. Shih, J. M. Woodall, S. E. Blum, and L. M. Foster, "Efficient Green Electroluminescence from GaP p-n Junctions Grown by Liquid-Phase Epitaxy," **J. Appl. Phys.**, Vol. 39, p. 2962, May 1968.

[3] R. A. Logan, H. G. White, and W. Wiegmann, "Efficient Green Electroluminescent Junctions in GaP," **Solid-State Electron.**, Vol. 14, p. 55, Jan. 1971.

[4] A. S. Brown and A. J. Springthorpe, "Defects in Epitaxial Gallium Phosphide," **Phys. Status Solidi (2)**, Vol. 7, p. 495, Oct. 1971.

[5] See, for example, M. Toyama, A. Kasami, M. Naito, and K. Maeda, "Effect of Heat Treatment on Diffused GaP Electroluminescent Diodes," **Trans. Met. Soc. AIME**, Vol. 245, p. 551, March 1969.

[6] H. C. Casey, Jr. and F. A. Trumbore, "Single Crystal Electroluminescent Materials," **Materials Science and Engineering**, Vol. 6, p. 69, 1970.

[7] D. G. Thomas and J. J. Hopfield, "Isoelectronic Traps Due to Nitrogen in GaP," **Phys. Rev.**, Vol. 150, p. 680, Oct. 14, 1966.

[8] H. Nelson, U.S. Patent 3,565,702.

Non-Destructive Sheet-Resistivity Measurements with Two-Point Probes

J. L. Vossen

RCA Laboratories, Princeton, N.J.

Absract—A simple, nondestructive two-point probe for rapid and accurate sheet-resistivity measurements has been developed and characterized. The accuracy of the measurement above 10 ohms/square is limited only by the accuracy of the ohmmeter or bridge employed. Below this resistivity, probe contact resistance increasingly limits the measurement accuracy. The probe diameter and the force applied to it cannot result in plastic deformation of substrates, which cracks films, but it will scratch very soft metals such as Au. The system is especially useful for measuring transparent conducting films on surfaces that must not be damaged (e.g., vidicon faceplates).

Introduction

There is a need in thin-film technology for simple, accurate, and nondestructive sheet-resistivity measurements over a wide range of values. This need is especially true for the transparent conducting films used, e.g., in vidicons and liquid-crystal displays. In these and similar applications, the range of sheet resistivity values can vary from 10 to 100,000 ohms/square, and the measurement technique must be such that the film is not disturbed in any way (scratches, indentations, etc.). Even very small scratches and mechanical imperfections show up as visible defects in many electro-optic devices.

This paper describes a simple, inexpensive test set for this application. The first measurement scheme that comes to mind for sheet-resistivity measurements is the four-point probe (Kelvin contact) method using either dc[1,2] or ac[3] power. This approach is not suitable for this application, however, for two reasons. First, since a constant-current source is employed, very high voltages would be required to make the high sheet-resistivity measurements. Using relatively low voltages (⩽50 volts) four-point probe techniques are limited to sheet resistivities below about 10,000 ohms/square. Secondly, the four probes must be very closely spaced to permit measurements near the periphery of the film,[3] implying that the probes must be physically small. If the probe-tip radius is small, damage results because of plastic deformation of the substrate.[4] Thus, one is forced to choose a two-point probe system. The basic problem with two-point probe measurements is probe contact resistance, and this problem is further aggravated by the requirement for a probe pressure sufficiently low to avoid plastic deformation of the substrate.

The load required to start plastic flow is directly proportional to the square of the tip radius.[4] Thus, it is desirable to have as large a tip radius as possible. However, to keep the probe separation as small as possible, so that measurements can be made near the edges of the substrate, the tip radius should be small.[3] The compromise selected was a 0.9 mm diameter spherical tip, for which the critical load for plastic deformation of most glasses is approximately 30-35 grams.

Mechanical Design of Probe

A very convenient, spring-loaded probe assembly was fabricated using dial thickness indicators with spherical tips.[5] These indicators are actually intended to be used for small incremental thickness measurements, but they are ideal for the present application, since the load exerted is only 20-22 grams over their entire scale range (0-15-0 mils). This load does not result in plastic deformation of most glasses and will scratch only the softest metal films (Au, Ag, etc.).

The ball tips on these indicators are Cr-plated steel and are subject to corrosion leading to contact-resistance variations with time. To eliminate corrosion, the tips were coated with approximately 1 μm of Rh deposited by dc sputtering with rf-induced substrate bias.[6] Rh was selected for its durability and resistance to corrosion.

Fig. 1 shows the complete probe assembly. The probes are rigidly

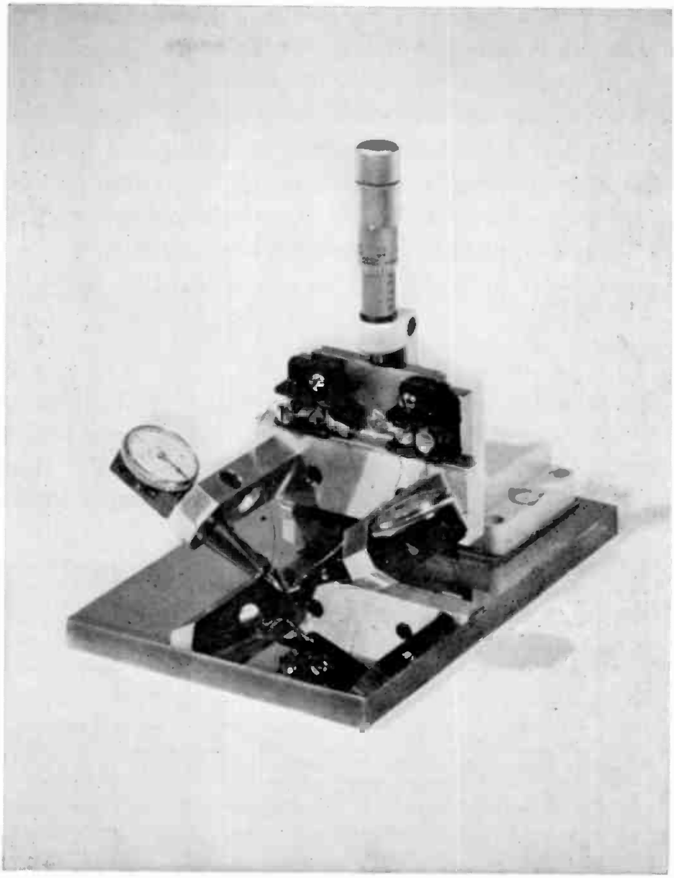

Fig. 1—Two-point-probe assembly.

mounted in clamps attached to a vertical-motion micropositioner. The mount isolates one probe from the micropositioner electrically. The probe spacing and angles are set so that both probes touch a flat surface at exactly the same point in the micropositioner travel. The initial probe angle is 30°. At the point of initial contact, the probe separation (center to center) is 2.16 mm. As the probe is further depressed to an indicator reading of 15 mils (half-scale), the probe pivots and the separation decreases to 1.5 mm. That is, each of the ball tips slide across the film surface a distance of 0.33 mm. The dial indicator reading enables one to repeat the probe separation to better than 0.0125 mm, which is approximately 0.8% of the probe spacing at the measurement point.

The entire assembly is mounted on a polished steel base that is coated with Rh in the same manner as the probe tips. The Rh coating is employed to prevent corrosion, so that the base itself can be used for zeroing out any contact resistance in the circuit.

The mechanical linkages involved in the spring-loaded indicator assembly produce erratic contact-resistance variations. To circumvent this, a fine magnet wire (AWG #30) is soldered to each probe above the ball tip and connected to a terminal block.

Any ohmmeter or bridge can be used with this assembly.

Calibrations

To calibrate probe resistance reading with actual sheet resistivity, about 20 transparent conducting films were rf sputtered onto electroded microscope slides. In general, the lower resistivity ranges were covered by In_2O_3:Sn[7] and the higher resistivity ranges by SnO_2:Sb.[8,9]

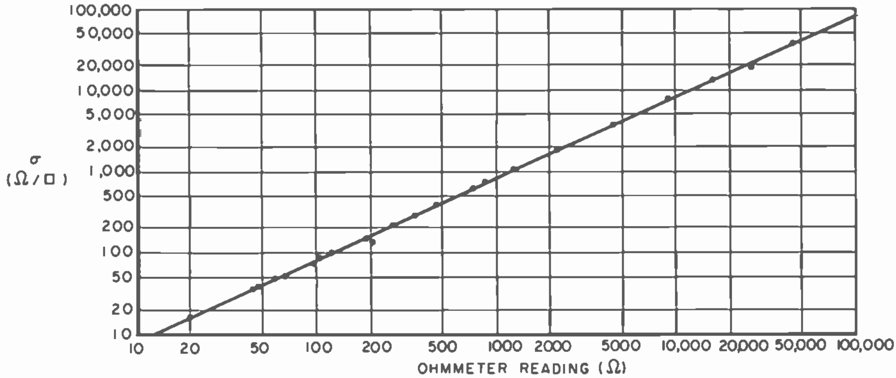

Fig. 2—Probe calibration. Sheet resistivity versus resistance reading.

The electrodes on the substrates (evaporated Cr-Cu) were 1 inch wide and separated by 1 inch. The transparent conductor films were masked during deposition to overlap the electrodes. The electrodes could then be used to measure directly the sheet resistivity of the oxide films and also to determine how close to the electrode one could measure with the probes without obtaining spurious readings.

Because of the high refractive index of the transparent conductor films (approximately 2.0), it is possible to detect thickness variations as small as 50 Å by observing color changes in reflection. All films were uniform to at least ±50 Å as no variation in color could be detected.

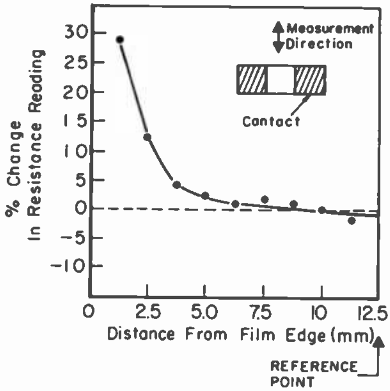

Fig. 3—Effect of film-edge proximity on probe resistance reading.

Fig. 2 shows the film sheet resistivity versus the probe resistance reading for measurements made near the center of each film. Each of the datum points represents an average of 10 probe measurements on each film.

To determine how closely the probes may aproach the film edge before spurious readings result, several of the films were probed at 0.125 cm increments from the edge of the substrate to the center of the film. The average deviation of the resistance reading from the reading at the center of the film is plotted in Fig. 3. If measurements

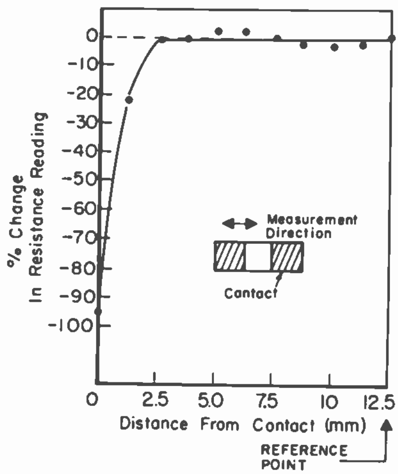

Fig. 4—Effect of proximity to an electrical contact on probe resistance reading.

are made farther than about 0.25 cm from the film edge, the error is at most 10% and can be corrected by using the data plotted in Fig. 3. Similar measurements were made to determine how closely the probes may be used to the Cr-Cu contacts, which had a sheet resistivity of 0.002 ohm/square as determined by four-point probe measurements. These data are plotted in Fig. 4.

Conclusions

A simple, nondestructive two-point probe for rapid and accurate sheet-resistivity measurements has been developed. The accuracy of the measurement above 10 ohms/square is limited by the accuracy of the ohmmeter used. Below this resistivity, probe contact resistance increasingly limits the measurement accuracy. The probe diameter–pressure combination used does not cause plastic deformation of substrates and cracking of films, but will scratch soft metal films such as Au. This device is especially useful for measuring transparent conducting films on surfaces that canot be damaged (e.g. vidicon faceplates).

Acknowledgment

The mechanical design and fabrication of the probe described above was almost completely done by J. J. Pacia. The use of the Starrett dial indicator as the heart of the probe element was his suggestion.

References:

[1] L. B. Valdes, "Resistivity Measurements on Germanium for Transistors," **Proc. IRE,** Vol. 42, p. 420 (1954).

[2] F. M. Smits, "Measurement of Sheet Resistivities with the Four-Point Probe," **Bell Syst. Tech. J.,** Vol. 37, p. 711 (1958).

[3] M. A. Logan, "An AC Bridge for Semiconductor Resistivity Measurements Using a Four-Point Probe," **Bell Syst. Tech. J.,** Vol. 40, p. 885 (1961).

[4] P. Benjamin and C. Weaver, "Measurement of Adhesion of Thin Films," **Proc. Roy. Soc.** (London), Vol. A254, p. 163 (1960).

[5] Model. No. 711 F Dial Test Indicator with Model 711-16A (0.035-inch diameter ball tip); L. S. Starrett Co., Athol, Mass.

[6] J. L. Vossen and J. J .O'Neill, Jr., "DC Sputtering with RF-Induced Substrate Bias," **RCA Rev.,** Vol. 29, p. 566 (1968).

[7] J. L. Vossen, "RF Sputtered Transparent Conductors, II: The System In_2O_3-SnO_2," **RCA Rev.,** Vol. 32, p. 289 (1971).

[8] J. L. Vossen, Proc. 3rd Symposium on the Deposition of Thin Films by Sputtering, Univ. of Rochester (Sept. 9, 1969), p. 80.

[9] J. L. Vossen and E. S. Poliniak, to be published (Thin Solid Films).

Broad-Band Acousto-Optic Deflectors Using Sonic Gratings for First-Order Beam Steering

Gerard A. Alphonse

RCA Laboratories, Princeton, N. J.

Abstract—A broad-band acousto-optic (AO) Bragg deflector using acoustic beam steering to track the Bragg angle is described. The variable acoustic beam is the "first order" output of a flat transducer grating made up from a single piezoelectric platelet. The correct diffraction theory applicable to AO deflectors is reviewed, including an accurate analytical description of the intensity of the second-order light that limits the deflector's bandwidth, and the theory of broad-band steering deflectors is developed. Experimental results on lead molybdate deflectors are presented to verify the prediction that the achievable beam-steering bandwidth is a constant that depends only on materials parameters, the optical wavelength and the width of the acoustic column. This is, in turn, shown to be at least four times the optimum bandwidth obtainable from the standard fixed-beam Bragg deflectors. Finally, techniques are presented to improve the fabrication yield of devices using lead molybdate as the AO medium, and to easily convert any standard deflector to the beam-steering mode of operation.

1. Introduction

Acousto-optic (AO) devices are finding widespread application as light deflectors in optical memories[1-5] and in other systems such as optical processors,[6] laser television displays,[7,8] acoustic switches,[9] intracavity devices for Q-switched lasers,[10] and picosecond light generators.[11] In its simplest form, the device consists of an acousto-optic medium to which is bonded an electrically driven piezoelectric transducer. The acoustic strain wave modulates the refractive index of the medium, and the medium acts as a "thick" grating that strongly diffracts light in a preferred direction when the light is incident on it in a narrow angular range near the Bragg angle. The effect is identical to x-ray diffraction in crystals. The grating period is equal to the wavelength of the sound in the AO medium, and when the acoustic frequency is below the microwave region, the direction of the output light is proportional to the acoustic frequency. The Bragg angle of a given order is uniquely specified by the optical wavelength and the acoustic frequency. The efficiency of the deflector represents the amount of incident light that is converted to first-order (the strongest) diffracted light; it is proportional to the acoustic power and beam width. The resolution is related to the angular range or diffraction bandwidth that can be swept while maintaining a satisfactory efficiency; it is inversely proportional to the Bragg frequency and to the acoustic beam width. The effective resolution is often limited by the constraint that the second-order light is not allowed in the space covered by the first order. Thus, not only are the efficiency and resolution limited, but also neither one can be arbitrarily increased without adversely affecting the other.

It has been well recognized that if the Bragg condition is continuously satisfied by rotating the acoustic beam in the direction of the diffracted light as the acoustic frequency varies, the efficiency–resolution performance would be significantly improved. The width of the transducer would be chosen for the desired efficiency, the center frequency would be chosen high enough for the transducer to have the desired bandwidth, and the acoustic steering process would maintain the Bragg condition for the first order over the whole bandwidth, thus eliminating the second order and overcoming the effect of the narrow diffraction bandwidth at high frequencies.

Much work has been done in the use of phased transducer arrays for beam steering. Korpel et al[6] have experimented with water cells using an array of transducers mounted on a common plane and connected in a series configuration that gives a phase shift of 180° between transducers. The output of the array consisted of two acoustic beams of equal intensity whose directions were frequency dependent. One of the beams was used for light diffraction and the second one discarded. However, because the frequency range of operation was too low (10 to 30 MHz), the second beam was within the appropriate range of angles to diffract the output light into new directions, resulting in a loss of output. This problem was overcome by some of the same authors[6] who mounted the transducers in ascending steps of height equal to one-half the acoustic wavelength at the center frequency, thus creating a blazed grating that eliminated the undesired acoustic beam. Several variations of this basic scheme were studied by Coquin et al,[12] who achieved a bandwidth of 250 MHz in a lithium niobate deflector using an array CdS transducer evaporated on steps machined on one face of the lithium niobate. Other work on beam steering include a theoretical analysis by Gordon[13] for single plane arrays having arbitrary phase difference between transducer elements (including the case where this phase shift is 180°) and design equations by Pinnow[14] for the stepped-array configuration.

For a given deflection range the Bragg frequency for solid AO media is higher than that for liquid media of the same dimensions by a factor of 3 to 5, and consequently the height of the steps for the stepped array must be correspondingly smaller. Practical AO deflectors require longitudinal acoustic waves for which lithium niobate is more suitable than cadmium sulfide as transducer. The lithium nibate transducer is usually bonded to the AO material by pressing both together in vacuum at several thousand psi after prior preparation of the surfaces to be bonded, namely after lapping and polishing them to optical flatness and parallelism, and coating them with an evaporated layer of indium. Lead molybdate, alpho iodic acid, telluride glass and other high-index glasses[15-17] are the most suitable materials for AO media, but they are soft, difficult to bond to the transducer, and susceptible to surface deterioration upon handling and to cleavage under pressure or heat induced stress. Such materials would be destroyed by the repeated operations of grinding, polishing, and bonding required to make the stepped arrays. Since the fabrication of the flat phased array is less complicated, this configuration is preferable for deflectors using the above materials if the acoustic frequency and the grating period of the transducer array are chosen such that the angular separation between the two acoustic beams is high enough to prevent the parasitic beam from interacting with the output light.

Part of this paper is aimed at bringing into perspective the correct and specific aspect of diffraction theory that applies to AO deflectors. Other parts are concerned with the analysis and design of beam-steering deflectors using flat arrays with 180° phase shift between array elements, the description of design configurations that allow the fabrication of the array from a single transducer, fabrication techniques that considerably increase the production yield of lead molybdate deflectors, and experimental results on lead molybdate beam-steering deflectors made according to the theory and techniques that are presented here. The overall result is that, for a given acoustic beam width, the bandwidth in the beam-steering mode is a constant equal to about four times the maximum bandwidth of an ordinary Bragg cell, and that any ordinary Bragg deflector can be easily converted to function in this mode.

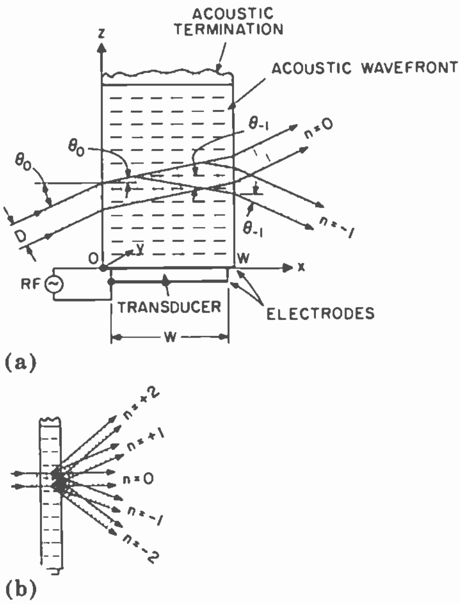

Fig. 1—Acousto-optic (Bragg) diffraction cell: (a) thick grating configuration and (b) thin grating configuration.

2. Review of Acousto-Optic Diffraction

An acousto-optic diffraction cell consists of a piezoelectric transducer bonded to one face of an AO medium (see Fig. 1a). The transducer may be a half-wave rotated Y-cut lithium niobate ($LiNbO_3$) platelet metallically coated on both surfaces; it has a high coupling constant and can be designed for broad-band operation. The AO medium may be any of the known materials with high photoelastic constants or tensor components (water, alpha iodic acid, lead molybdate, telluride glass, dense flint glass, etc.). The choice of the acoustic and optical polarization and direction depends on the relative magnitude of the photoelastic tensor components and on the configuration that makes the mathematics simplest. In this work we have chosen to use longitudinal acoustic waves propagating in the z direction (the "C" axis in crystals), and optical waves polarized in the y direction and propagating in the x direction. The application of an rf voltage to the transducer electrodes generates an acoustic strain wave in the medium. The far end of the AO medium opposite the transducer is terminated by an acoustic absorber to prevent reflection of sound from that end. The strain wave causes the refractive index of the midium to be periodically modulcated in space and time, with a spatial period equal to the wavelength, Λ, of the sound. The width W of the acoustic column being finite, the strain wave and the magnitude of the refractive index modulation diverge over a narrow angular range with a spread at the high-power points equal to Λ/W.

Light of wavelength λ_o in air is incident at an angle θ_o on the AO medium. In the absence of modulation it is refracted to an angle $\bar{\theta}_o$ which, by Snell's law, is given by $\sin \theta_o/\sin \bar{\theta}_o = n_o = \sqrt{\mathcal{E}_1}$, where n_o and $\mathcal{E}_1$ are, respectively, the appropriate refractive index and dielectric constant for light propagating in the direction $\bar{\theta}_o$. The optical surfaces at $x = 0$ and $x = W$ are anti-reflection coated to minimize reflections; the optical beam may be a Gaussian beam truncated by a circular aperture of diameter D or any other geometrical aperture.

With the sound present, the modulated AO medium acts as a thick phase grating of optical thickness W and period Λ. Thus, from an electromagnetic viewpoint, the effect of the interaction between the light wave and sound wave is the diffraction of the light by the grating. Intuitively one can distinguish two regimes where the solution is obvious. In the first regime, called Raman–Nath and illustrated in Fig. 1b, the grating is thin, so that each ray from the incident beam passes through a homogeneous region of the medium, i.e., it encounters no refractive index change in going from 0 to W. This situation occurs for values of incidence angle $\bar{\theta}_o$, acoustic wavelength Λ, and acoustic beam width W such that $\bar{\theta}_o \ll \Lambda/W$. In this case, since the refractive index is of the form

$$\tilde{n} = n_o \left[1 + \frac{\Delta n}{n_o} \cos (\Omega t - Kz) \right],$$

the phase factor of the light is just the exponential $\exp [ik_o Wn \cos \bar{\theta}_o]$, where $k_o = \omega_o \sqrt{\mu_o \mathcal{E}_o} = 2\pi/\lambda_o = \omega_o/c$ is the optical wave number in free space, μ_o and $\mathcal{E}_o$ the permeability and permittivity of free space, ω_o the angular frequency of the light, λ_o its wavelength in free space, and

c the speed of light in vacuum. Since the exponential is periodic, a Fourier expansion decomposes it into a set of exponentials representing the spectral orders or space harmonics of the diffracted light with magnitudes equal to $J_m[k_o W \Delta n \cos \bar{\theta}_o]$, where J_m is the Bessel function of the first kind and integral order m, and directions $\bar{\theta}_m$ given by $\sin \bar{\theta}_m = \sin \bar{\theta}_o + m[\lambda_o/(n_o \Lambda)]$. Outside the medium the angles become θ_m obtained from $\bar{\theta}_m$ by Snell's law.

When the grating is not "thin", a given light ray passes through inhomogeneous regions, i.e., the refractive index does not have the same value at every point in the light's path. As a ray progresses it is partly reflected by the various index planes. As always with monochromatic light, those reflected rays interfere with each other destructively in most directions except those directions corresponding to the Bragg angles and for which the optical path difference is an integral number of optical wavelengths. At a given Bragg angle, only the zeroth order and the order m that satisfies both the grating equation and the Bragg condition exist. Moreover the relation $|\bar{\theta}_o| = |\bar{\theta}_m|$ is satisfied, and any fraction of the incident light can be diffracted into that order, just as in a blazed grating. For a given acoustic power the diffraction efficiency is highest for the first order $(m = \pm 1)$ Bragg regime.

The mathematical treatment of the problem is complicated. A direct method consists of integrating Fraunhofer's approximation over the whole volume of the AO medium,[13] however it does not give much insight into the nature of the problem. Another method consists of rigorously deriving the appropriate solution of the wave equation in the periodic medium. It gives a set of characteristic solutions from which any particular solution can be obtained as a linear combination. When used in conjunction with coupled mode theory, it gives a lot of insight into the nature of the problem. The appropriate wave equation in the MKS system for a medium with inhomogeneous permittivity is

$$\nabla^2 \mathbf{E} + \nabla (\underset{\sim}{\mathcal{E}}^{-1} \mathbf{E} \cdot \nabla \underset{\sim}{\mathcal{E}}) - \mu_o \mathcal{E}_o \frac{\partial^2}{\partial t^2} \mathcal{E} \mathbf{E} = 0 \qquad [1]$$

where $\mathbf{E}$ is the electric field vector and $\underset{\sim}{\mathcal{E}}$ the dielectric permittivity tensor. This equation is derived from Maxwell's equations $\nabla \times \mathbf{E} = -\partial/\partial t\, \mathbf{B}$, $\nabla \times \mathbf{H} = \partial/\partial t\, \mathbf{D}$, the vector identity $\nabla \times \nabla \times \mathbf{E} = \nabla(\nabla \cdot \mathbf{E}) - \nabla^2 \mathbf{E}$ and the relation $\nabla \cdot \mathcal{E}\mathbf{E} = \mathcal{E} \nabla \cdot \mathbf{E} + \mathbf{E} \cdot \nabla \mathcal{E} = 0$ in a source-free medium. The quantities $\tilde{\mathbf{D}}$ and $\tilde{\mathbf{B}}$ are the electric displacement tensor and the magnetic field density vector, respectively. Eq. [1] can be reduced to a simple scalar wave equation by an appropriate choice of coordinates and field polarization. Without any loss of generality, let all motions be in the x-z plane, i.e. $\partial/\partial y \equiv 0$. Let the electric field be polarized in the y direction, i.e., $\mathbf{E}(x,z,t) = \mathbf{y}_o E(x,z,t)$ where $\mathbf{y}_o$ is the unit vector in the y direction, and let the strain be directed in the z direction (with a small diffraction spread in the x direction). From Appendix 1 we see that only the component $\mathcal{E}_2$ enters the wave equation as (in reduced notation)

$$\mathcal{E}_2(z,t,\phi) = \mathcal{E}_2(0) - \mathcal{E}_2^{\,2}(0) p_{33} S_3(z,t,\phi), \qquad [2]$$

where $\mathcal{E}_2(0)$ is the value of $\mathcal{E}_2$ in the absence of sound, p_{33} is the component of the photoelastic tensor that participates in the acousto-optic interaction and $S_3(z,t,\phi)$ the acoustic strain given by (see Appendix 2)

$$S_3(z,t,\phi) = \left[\frac{2P_d}{\rho v^3}\right]^{1/2} \operatorname{sinc}\left[\frac{KW}{2}(\sin\phi - \sin\phi_o)\right] \cos(\Omega t - Kz), \qquad [3]$$

where P_d is the acoustic power density in the AO medium, ρ the mass density, v the speed of longitudinal wave in the chosen direction, Ω the acoustic angular frequency ($\Omega = 2\pi f$, f being the rf frequency), K the magnitude of acoustic wave vector ($K = 2\pi/\Lambda = \Omega/v$), all in the AO medium, and $\operatorname{sinc} x \equiv (\sin x)/x$. The function $\operatorname{sinc}[(KW/2)\sin\phi - \sin\phi_o)]$ is the angular spectrum of the strain amplitude spreading over a small range of angles ϕ about the launching direction ϕ_o (which in this case is the z axis, measured from some convenient reference angle ϕ_o). The half-power spread of the strain is easily found to be $\Delta\phi = \Lambda/W$. The choice of $\mathbf{E}$ and $\mathcal{E}_2$ makes $\mathbf{E}\cdot\nabla\mathcal{E}_2 = 0$, and Eq. [1] becomes the scalar equation in the region $0 < x < W$:

$$\nabla^2 E(x,z,t) - \mu_o\mathcal{E}_o \frac{\partial^2}{\partial t^2}[\mathcal{E}_2(z,t)E(x,z,t)] = 0. \qquad [4]$$

In the formal solution[18-20] the electric field is given as a summation in terms of *characteristic modes*. These modes are solutions of the wave Eq. [4], which, because of Eqs. [2] and [3], take the form of Mathieu's equation. By use of Floquet's theorem these characteristic modes are expanded into a Fourier series giving rise to the *spectral* *orders*, sometimes called space harmonics. As a result the net field is a double summation over all the characteristic modes and the spectral orders. This rigorous and complete solution is complicated, but it does yield analytical results in any region, including the Bragg regimes of arbitrary order, with any desired degree of accuracy.

By interchanging the order of the summation a set of *normal modes*, which are the same as the spectral orders, can be found. These modes can exist independently of one another in the absence of sound, i.e., in the limit where $\Delta n \rightarrow 0$. Thus, when independent of one another, they represent solutions to the wave equation in the unmodulated medium, and their propagation numbers can be plotted on a dispersion diagram. When light is incident at some angle $\overline{\theta}_o$, the zeroeth order mode, which is the same as the transmitted wave, is the only mode that is excited (there are no reflections at $x = 0$ and W because these surfaces are antireflection coated). When the medium is modulated by the sound, these modes become coupled, and energy is transferred between the coupled modes at the points of coupling in the dispersion diagram. This corresponds to the excitation of the observed higher spectral orders. It is important to recognize that these modes are the same as in the unmodulated medium and that the effect of the modulation is to couple them. Since Δn is usually of the order of 10^{-4} or less, the propagation constants of these modes are essentially the same as in the unmodulated medium except at the point of coupling. A set of coupled-mode equations can be obtained from the wave equation, and for a given situation (incidence angle, acoustic frequency) the number of propagating modes can be found from the dispersion diagram, and their magnitudes found from the coupled equations.

In the specific situation where the acoustic frequency is below the microwave range, Ω is much smaller than ω_o, i.e.

$$\frac{\partial^2}{\partial t^2} \mathcal{E}_2 E \cong \mathcal{E}_2 \frac{\partial^2 E}{\partial t^2}.$$

Then, writing $\mathcal{E}_2 = [n_o + \Delta n \cos (\Omega t - Kz)]^2$ where $n_o = \sqrt{\mathcal{E}_2(0)}$ and $\Delta n \ll 1$, it follows that the wave Eq. [4] can be written

$$\frac{\partial^2}{\partial x^2} E + \frac{\partial^2}{\partial z^2} E + (k_o n_o)^2 \left[1 + 2 \frac{\Delta n}{n_o} \cos (\Omega t - Kz) \right] E = 0, \qquad [5]$$

where, from Eq. [2],

$$\Delta n = -\frac{1}{2}\mathcal{E}_2(0)p_{33}|S_3|\sqrt{\mathcal{E}_2(0)}$$
$$= \left[\frac{M_2 P_d}{2}\right]^{1/2} \operatorname{sinc}\left[\frac{KW}{2}(\sin\phi - \sin\phi_o)\right], \quad [6]$$

$$M_2 = \frac{(n_o{}^3 p_{33})^2}{\rho v^3}.$$

The parameter M_2, which involves only material constants, is the so-called figure of merit of the AO medium. It determines the amount of refractive index modulation that results from the application of a given amount of acoustic power.

Let the incident wave be of the form $E(x,z,t) = E_i \exp[i(\mu x + \nu z - \omega_o t)]$ in air, where the wave numbers in the x and z direction obey the relations

$$\mu = k_o \cos\theta_o, \qquad \nu = k_o \sin\theta_o,$$
$$\mu^2 + \nu^2 = k_o{}^2. \quad [7]$$

In the absence of modulation the field is refracted to an angle $\bar{\theta}_o$ in the medium. It is of the form $\bar{E}(x,z,t) = E_i \exp[i(\bar{\mu}x + \bar{\nu}z - \omega_o t)]$, where $\bar{\mu}$ and $\bar{\nu}$ obey the relations

$$\bar{\mu} = k_o n_o \cos\bar{\theta}_o,$$
$$\bar{\nu} = k_o n_o \sin\bar{\theta} = \nu,$$
$$\bar{\mu}^2 + \bar{\nu}^2 = (k_o n_o)^2. \quad [8]$$

In the remainder of this paper, the bar on top of a symbol indicates the unmodulated medium. The boundary condition at $x = 0$ requires $\bar{\nu} = \nu$, giving Snell's law $n_o \sin\bar{\theta}_o = \sin\theta_o$. When the medium is modulated, the coupled mode solution is given by[20]

$$\tilde{E}(x,z,t) = \sum_{m=-\infty}^{\infty} A_m(x)\exp\{i\tilde{\mu}_m x\}\exp[i(\tilde{\nu}_m z - \omega_m t)], \quad [9]$$

where $\tilde{\nu}_m = \bar{\nu}_m = \bar{\nu} + mK = \nu + mK,$

$$\omega_m = \omega_o + \omega\Omega. \quad [10]$$

It can also be shown[20] that

$$dA_m/dx = i \sum_s c_{ms} A_s, \qquad [11]$$

where c_{ms} is a set of coefficients that can be calculated from the formal solution of Eq. [5].

In the remainder of this paper, the tilde on top of a symbol indicates the modulated medium. The interpretation of Eq. [9] is that the field is obtained as a summation over an infinite number of modes of the form $\exp\,[i\tilde{\nu}_m z - \omega_m t]$ propagating in the x-direction as $\exp\,\{i\mu_m x\}$. The coefficients $A_m(x)$ represent the amount of field excited in the m^{th} mode; it is a function of Δn and of the interaction distance. As $\Delta n \to 0$, the modes become uncoupled, i.e., $A_o \to E_i$, $A_m(m \neq 0) \to 0$, $\tilde{\mu}_m \to \bar{\mu}_m$, resulting in the dispersion relation

$$\begin{aligned} &\bar{\mu}_m{}^2 + (\bar{\nu} + mK)^2 = (k_o n_o)^2, \text{ for } \bar{\nu} + mK < k_o n_o \\ &-|\bar{\mu}_m|^2 + (\bar{\nu} + mK)^2 = (k_o n_o)^2, \text{ for } \bar{\nu} + mK > k_o n_o. \end{aligned} \qquad [12]$$

The significance of this last equation is that each mode m is a wave traveling in a direction $\bar{\theta}_m$, such that $\bar{\mu}_m = k_o n_o \cos \bar{\theta}_m$ and $\bar{\nu}_m = (\nu + mK) = k_o n_o \sin \bar{\theta}_m$. This last expression is usually written

$$\sin \bar{\theta}_m = \frac{\bar{\nu} + mK}{k_o n_o} = \sin \bar{\theta}_o + \frac{mK}{k_o n_o} = \sin \bar{\theta}_o + m \frac{\lambda_o}{n_o \Lambda}. \qquad [13]$$

These modes do exist even in the absence of modulation. In that case, however, only the $m = 0$ order has physical significance, since $A_o = E_i$, $A_m(m \neq 0) = 0$, and the dispersion relation Eq. [12] reduces to Eq. [8] for $m = 0$.

The behavior of the solution can be predicted[20] with the held of the dispersion diagram of Fig. 2. This diagram is a plot of $\bar{\nu}$ vs $\bar{\mu}$ from Eq. [12] for the unmodulated medium ($\Delta = 0$) or $\bar{\nu}$ versus $\tilde{\mu}$ for the modulated medium ($\Delta n \neq 0$). In the absence of modulation, the curves are either circles for $\bar{\nu}_m < k_o n_o$ or hyperbolas for $\bar{\nu}_m > k_o n_o$. There is one curve centered at $\bar{\nu} = -mK$ for each value of m (i.e., for each mode). The circles correspond to propagating modes, the hyperbolas to modes that are evanescent. These curves cross one another in the dotted regions of the diagram. At the points of intersection between the dispersion curves of any two modes, these modes have the same propagation characteristics, i.e., the same values of $\bar{\mu}_m$ and $\bar{\nu}_m$, even though m is not the same for both. When the medium is modulated, these modes are coupled at their points of intersection, as shown by the solid curves joining the crossing circles at the left and right of the dotted regions, and the set of solid curves represents the new dispersion diagram, i.e., the plot of $\bar{\nu}$ versus $\tilde{\mu}_m$ for the modulated medium. This new dispersion diagram is essentially the same as for the unmodulated

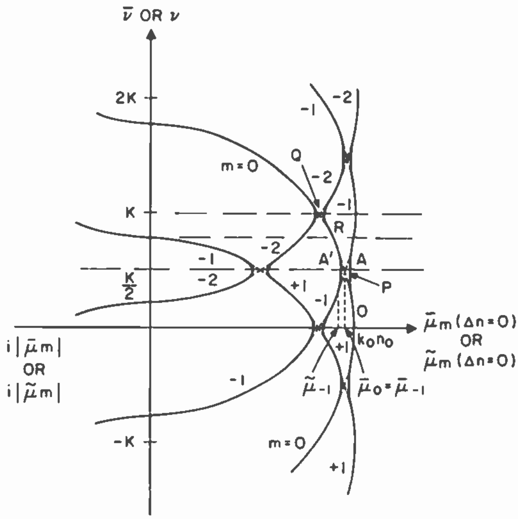

Fig. 2—Dispersion diagram for periodically modulated medium (only waves for $m = -2$ to $m = +1$ are shown). The dotted intersections of the circles correspond to the unmodulated case and the solid curves near the intersections correspond to the modulated case.

medium except for the regions where mode coupling occurs. Thus in most regions, little energy is coupled between the modes, just as in the absence of modulation; but in the coupling regions the exchange of energy is strong. The more rigorous analysis using the theory of Mathieu's equation reveals that these mode coupling regions are the actual Bragg regimes mentioned earlier, and that $\bar{\nu}$ is imaginary in those Bragg regimes, i.e., the Bragg regimes correspond to stop bands of z-propagation in the medium. The width of the bandgap is proportional to the strength of the modulation.

In acousto-optic deflectors operating at acoustic frequencies below the microwave range, K is very much less than $k_o n_o$ (by a factor of several hundreds in some cases). The circles for the unmodulated medium are very close to one another, and the set of modes that are coupled are not necessarily those that are coupled when K is high.

This case is illustrated in the neighborhood of $\bar{\nu} \approx 0$ by the enlarged diagram in Fig. 3. As the acoustic frequency increases, the diagram changes from Fig. 3 to Fig. 2.

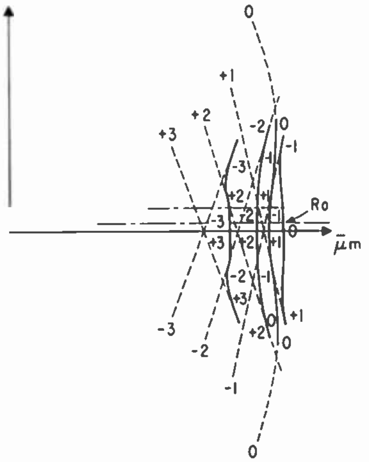

Fig. 3—Enlarged dispersion diagram near $\nu \cong 0$ illustrating mode coupling at low acoustic frequencies.

The above considerations can now be used to examine the diffraction of a plane wave by the modulated medium. Consider a plane wave incident at an angle $\bar{\theta}_o$ on the medium. Since $\bar{\nu} = k_o n_o \sin \bar{\theta}_o$ is a constant, the value $\tilde{\mu}_m$ for each mode can be found by drawing a horizontal line having $\bar{\nu}$ as its ordinate, and marking its intersection with the dispersion curves. Several cases can be considered.

2.1 Raman-Nath Solution

If the acoustic frequency is very low and the incidence angle near normal ($\bar{\theta}_o \cong 0$), the mode coupling is as shown in Fig. 3. The horizontal line drawn on it shows that the incident or $m = 0$ mode is given by a point R_o and the other modes by R_m (not shown on the diagram for the sake of clarity). It can be seen that $m = 0$ is coupled to $m = -1$ and $m = +1$, $m = -1$ to $m = 0$ and $m = -2$, etc., i.e., the modulation couples nearest neighbor modes. An examination of Eq. [5] shows that

$$\cos (\Omega t - Kz) = \frac{1}{2} \exp \{i(Kz - \Omega t)\} + \exp \{-i(Kz - \Omega t)\}$$

couples the m mode to the $m \pm 1$ modes. Therefore substitution of Eq. [9] into Eq. [5] yields the appropriate coupled-mode equations for this case, assuming A_m to be slowly varying (i.e., $d^2A_m/dx^2 = 0$) and assuming $\tilde{\mu}_m \cong \bar{\mu}$:

$$\xi A_{m-1} + \frac{dA_m}{dx} - im\beta_m A_m - \xi^* A_{m+1} = 0, \qquad [14]$$

where

$$\xi = -i\frac{k_o\Delta n}{2\cos\bar{\theta}_o}, \quad \beta_m = \frac{K}{\cos\bar{\theta}_o}\left(\sin\bar{\theta}_o + \frac{mK}{2k_o n_o}\right) \cong K\bar{\theta}_o,$$

with the boundary condition $A_o(0) = E_i$, $A_m(0) = 0$. The solution to Eq. [14] at $x = W$ is

$$A_m(W) = E_i \exp\left[-i\beta_m\frac{W}{2}\right] J_m\left[2\xi W \operatorname{sinc}\left(\beta_m\frac{W}{2}\right)\right] \qquad [15]$$

where J_m is the Bessel function of the first kind order m. Because of the sinc $(\beta_m W/2)$ term in the expression, this solution is significant only near normal incidence, i.e., for $|\bar{\theta}_o| < \pi/(KW)$.

2.2 Solution in the First Bragg Regime

In this case the horizontal line drawn in Fig. 2 passes through the P on the $m = 0$ circle in the absence of modulation and the points A and A′ on the $m = 0$ and $m = -1$ curves in the presence of modulation and intersects the $\bar{\nu}$ axis at $K/2$. The abscissas of points A and A′ give μ_o and $\tilde{\mu}_{-1}$, and since $\bar{\nu} = k_o n_o \sin\bar{\theta}_o$, the Bragg incidence angle is

$$\sin\bar{\theta}_o = \frac{K}{2k_o n_o} = \frac{\lambda_o}{2\,n_o\Lambda}. \qquad [16]$$

The line AA′ may cross other curves, as shown in Fig. 2; this line shows that the $m = +1$ and $m = -2$ modes are also coupled. However these other modes are not coupled to the $m = 0$ mode and hence are not excited by the latter. In solving the set of equations [14], only those two containing A_o and A_{-1} need be retained, and the following set of coupled equations is obtained:

$$\frac{dA_o}{dx} - \xi^* A_{-1} = 0, \qquad [17]$$

$$\frac{dA_{-1}}{dx} - i\beta_{-1}A_{-1} + \xi A_o = 0,$$

where

$$\beta_{-1} = \frac{K}{\cos \bar{\theta}_o}\left(\sin \bar{\theta}_o - \frac{K}{2k_o n_o}\right)$$

With the same boundary condition as in Eq. [14], the solution to Eq. [17] is, at $x = W$,

$$A_o(W) = -E_i\,[\cos \alpha W - (i\beta_{-1}/2\alpha) \sin \alpha W] \exp [-i\beta_{-1}W/2], \qquad [18]$$

$$A_{-1}(W) = -E_i\,[(\xi/\alpha) \sin \alpha W] \exp [-i\beta_{-1}W/2],$$

where

$$\alpha = \left[|\xi|^2 + \left(\frac{1}{2}\beta_{-1}\right)^2\right]^{1/2}.$$

Note from Eqs. [11] and [14] that $\sin \bar{\theta}_{-1} = -\sin \bar{\theta}_o$ and that $\beta_{-1} = 0$ at the center of the Bragg regime. This gives for the intensities at the center of the regime:

$$|A_o|^2 = E_i^2 \cos^2 (|\xi| W) \text{ and } |A_{-1}|^2 = E_i^2 \sin^2 (|\xi| W),$$

and shows that for $|\xi| W = \pi/2$, all the incident energy is transferred to the $m = -1$ order.

2.3 Solution in the Second and Higher Order Bragg Regimes

In the second Bragg regime, the horizontal line passes through point Q in Fig. 2 where the $m = 0$ and $m = -2$ modes are synchronous. From the $\bar{\nu}$ intersect, the incidence angle is found to be

$$\sin \bar{\theta}_o = \frac{K}{k_o n_o} = \frac{\lambda_o}{n_o \Lambda}.$$

Eq. [9] is *not* an appropriate solution to Eq. [5] in this case, since a direct substitution does not lead to equations that couple the $m = 0$ and $m = -2$ modes. In general, the *coupled* mode set is not a direct solution of the wave equation. The direct solution of Eq. [5] is the set of *characteristic* or waveguide modes discussed earlier. However, each characteristic mode can in turn be represented by a set spectral modes and the complete solution cast in the form given by Eq. [9]. This solution is worked out in detail by Chu and Tamir[20] who obtain in the neighborhood of a Bragg regime of any order m a set of coupled equations of the form

$$\frac{dB_o}{dx} - i\bar{\mu}B_o - \xi_m{}^*B_{-m} = 0,$$

$$\frac{dB_{-m}}{dx} - i\bar{\mu}_{-m}B_{-m} + \xi_m B_o = 0. \qquad [19]$$

where

$$\xi_m = -i\frac{2k_o\Delta n}{\cos \bar{\theta}_o}\left[\frac{m}{m!2^m}\right]^2. \qquad [20]$$

The B_m coefficients are related to the A_m coefficients in this paper through the relation $B_{-m}(x) = \mathcal{E}^{i\bar{\mu}x} A_{-m}(x)$. Since $K \ll k_o n_o$ at acoustic frequencies below the microwave region, $\bar{\mu}_{-m}$ can be approximated by $\bar{\mu}_{-m} \cong \bar{\mu} + m\beta_{-m}$, and Eq. [19] reduces to

$$\frac{dA_o}{dx} - \xi_m{}^*A_{-m} = 0,$$

$$\frac{dA_{-m}}{dx} im\beta_{-m}A_{-m} + \xi_{-m}A_o = 0. \qquad [21]$$

Eq. [21] is a general form of Eq. [17] whose solution at $x = W$ is

$$A_o(W) = E_i \left[\cos \alpha_{-m} W - i\,(m\beta_{-m}/2\alpha_{-m}) \sin \alpha_{-m} W\right] \exp\left[-im\beta_{-m} W/2\right], \quad [22]$$
$$A_{-m}(W) = -iE_i \left[(\xi_m/\alpha_{-m}) \sin \alpha_{-m} W\right] \exp\left[-im\beta_{-m} W/2\right],$$

where

$$\alpha_{-m} = \left[|\xi_m|^2 + \left(\frac{1}{2} m\beta_{-m}\right)^2 \right]^{1/2}.$$

Eq. [22] is the solution for a Bragg regime of arbitrary order m when the incidence angle is in the neighborhood of the m^{th} Bragg angle given by $\sin \overline{\theta}_o = mK/(2k_o n_o)$.

2.4 Solution Between Bragg Regimes

When the incidence angle is between Bragg regimes, such as the point R between the first and second Bragg regime, the coupled-mode equations contain as many equations as there are modes of significant amplitudes. The equations are of the form

$$\frac{dA_m}{dx} - im\beta_m A_m - \sum_l \xi^*_{m,l} A_l = 0, \quad [23]$$

and the coefficients $\xi^*_{m,l}$ can be calculated using the procedure outlined by Chu and Tamir.[20] In particular, at point R of Fig. 2, where the $m = 0$ order is coupled to both the $m = -1$ and $m = -2$ orders, the mode equations can be written

$$\frac{dA_o}{dx} - \xi^*_{-1} - \xi^*_{-2} A_{-2} = 0,$$
$$\frac{dA_{-1}}{dx} - i\beta_{-1} A_{-1} + \xi_{-1} A_o = 0, \quad [24]$$
$$\frac{dA_{-2}}{dx} - 2i\beta_{-2} A_{-2} + \xi_{-2} A_o = 0.$$

The solution to Eq. [24] can be found by a number of methods, including Laplace transform and numerical integration, and will not be given here.

3. Application to Deflection Systems

In actual AO deflectors, the optical wavelength is a constant, the incidence angle is an adjustable parameter, and the acoustic frequency a variable. The incidence angle is adjusted to satisfy the first-order Bragg condition at the center frequency f_B of the transducer, and the actual frequency is varied approximately between $(1/2)f_B$ and $(3/2)f_B$. The wave number also varies between $(1/2)K_B$ and $(3/2)K_B$, where $K_B = (2\pi/v)f_B$. The effect of varying K is illustrated in Fig. 4. The

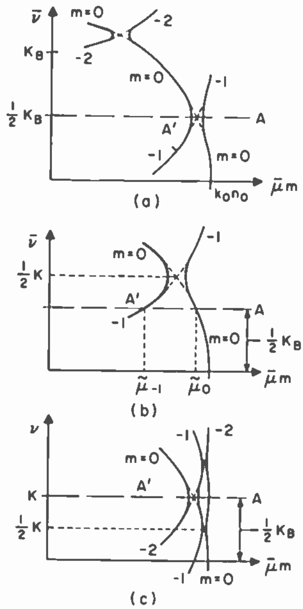

Fig. 4—Effect of changing frequency in AO deflectors: (a) Bragg Condition $K = K_B$; (b) $K > K_B$; (c) $K = K_B/2$.

incident angle is fixed at the first Bragg angle corresponding to f_B, i.e., $\bar{\nu} = (1/2)K_B$, and is represented by the line AA′. In Fig. 4a the acoustic frequency is f_B, i.e., the first Bragg condition is exactly satisfied by the $m = 0$ and $m = -1$ modes, and therefore A_{-1} is obtained from Eq. [16] by setting $\beta_{-1} = 0$. When the acoustic frequency is increased, the Bragg regime is shifted upward as in Fig. 4b. The strength of the coupling between the $m = 0$ and $m = -1$ modes is weakened, but there are no other modes present, and therefore A_{-1} is still given by Eqs. [18], using β_{-1} from Eqs. [17] with $\sin \bar{\theta}_o = K_B/2n_ok_o$. When the acoustic frequency is decreased, the $m = -2$

order approaches the line AA′; in particular, at $f = (1/2)f_B$, K is equal to $(1/2)K_B$ and the Bragg condition for the *second* order ($m = -2$) is satisfied by the incident light, as shown in Fig. 4c where $\bar{\nu} = K$. In that frequency range, the second-order light is prominent and A_{-2} is given by Eqs. [22] with $m = 2$. Thus for a given deflector, the second order becomes important at frequencies below the Bragg frequency. The results are summarized in the following expression for the efficiency η_m where $\eta_m = [|A_{-m}|/E_i]^2$:

$$\begin{aligned} \eta_1 &= [|\xi_1|/\alpha_{-1}]^2 \sin^2\alpha_{-1}W \\ \eta_2 &= [|\xi_2|/\alpha_{-2}]^2 \sin^2\alpha_{-2}W \end{aligned} \qquad [25]$$

$$\text{where } |\xi_1| = \frac{k_o \Delta n}{2\cos\bar{\theta}_o}, \qquad |\xi_2| = \frac{1}{4}|\xi_1|$$

$$[26]$$

$$\alpha_{-1} = \left[|\xi_1|^2 + \left(\frac{1}{2}\beta_{-1}\right)^2\right]^{1/2}, \; \alpha_{-2} = [|\xi_2|^2 + \beta_{-2}{}^2]^{1/2}$$

$$\beta_{-1} = \frac{K}{2k_o n_o \cos\bar{\theta}_o}(K_B - K), \; \beta_{-2} = \frac{K}{2k_o n_o \cos\bar{\theta}_o}(K_B - 2K)$$

$$K_B = (2\pi/v)\, f_B = 2n_o k_o \sin\bar{\theta}_o$$

The choice of K_B and $\bar{\theta}_o$ is usually dictated by convenience. However, there exists a lower limit to K_B, as determined by the crossover point between the Raman-Nath and the Bragg regimes. For a deflector aligned for $\bar{\theta}_o$ to be the Bragg angle for the first order, this crossover point may be chosen as the frequency for which all the higher order terms except J_o and J_{+1} in the Raman-Nath solution vanish. This point is obtained by setting $\beta_{-2}W/2 > \pi$, giving

$$K_B{}^2 W > 2\pi k_o n_o \text{ or } W > \frac{n_o \Lambda_B{}^2}{\lambda_o}, \qquad [27]$$

where $\Lambda_B = v/f_B$, as the condition to be met by a deflector in order to be operable in the first Bragg regime. Thus the minimum acoustic column width for Bragg operation at a given acoustic frequency f_B is $W_{BM} = n_o\Lambda_B^2/\lambda_o$. Alternatively, the minimum frequency for Bragg operation of a deflector having acoustic column width W is

$$f_{BM} = v\sqrt{\frac{n_o}{\lambda_o W}}.$$

The resolution of the deflector, i.e., the number of positions to which the first-order light beam can be focused as the acoustic frequency is varied over a range Δf_B, is the ratio of the swept angular range $|\Delta\overline{\theta}_{-1}|$ to the diffraction limited spot size $\delta\overline{\theta}$ of the light beam in the AO medium. From $\sin\overline{\theta}_{-1} = \sin\overline{\theta}_o - K/(k_o n_o)$, it is clear that for $\overline{\theta}_{-1}$ small, $|\Delta\overline{\theta}_{-1}|$ is given by

$$|\Delta\overline{\theta}_{-1}| = \frac{\Delta K}{k_o n_o} = \frac{\lambda_o}{n_o v}\Delta f_B. \qquad [28]$$

Table 1

Optical Beam Cross-Section	γ-Rayleigh	γ-Discrete
Square	1.0	2.0
Circular	1.22	2.44
Truncated Gaussian	1.27	2.54

From the Fourier transform of the incident optical beam of wavelength λ_o passing through an aperture D, the optical spread $\delta\overline{\theta}$ is

$$\delta\overline{\theta} = \gamma\frac{\lambda_o}{n_o D}, \qquad [29]$$

where the factor γ is a function of the cross section of the aperture and of the type of criterion used for the specification of $\delta\overline{\theta}$. The cross section may be square, circular, truncated Gaussian, or any other. If the criterion is the Rayleigh type, then $\delta\overline{\theta}$ is the angular range between the half-power points of the light beam. If the light spots are to be discrete or fully resolved, then $\delta\overline{\theta}$ is the angular range between the first zeros of the Fourier spectrum of the incident beam for the square or circular cross section, or the distance between the $\mathcal{E}^{-2}$ points for the truncated Gaussian beam. Table 1 gives some values of γ.

Taking the ratio of Eq. [28] to Eq. [29], the resolution is thus[7,13]

$$N_B = \frac{|\overline{\Delta\theta}_{-1}|}{\delta\theta} = \frac{1}{\gamma}\tau\Delta f_B, \quad [30]$$

where $\tau = D/v$ is the transit time of the sound across incident light beam. This time–bandwidth product is a fundamental limitation on any Bragg deflector.

The bandwidth is the distance between the half-power points in the plot η_1 from Eq. [25] versus frequency. If the bandwidth is large,

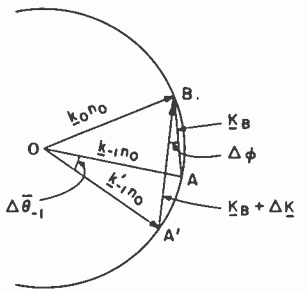

Fig. 5—Momentum diagram relating acoustic spread to change of optical diffraction angle due to change in acoustic frequency.

it is necessary to plot η_2 also and reduce the bandwidth by the frequency range over which the second order is within the field of view of the first order. Before proceeding with the plots, it is worthwhile to put in evidence the explicit frequency behavior of the parameters that enter Eq. [25]. The frequency dependence of β_{-1} and β_{-2} is quite evidence from Eq. [26]. The frequency dependence of ξ_1 and ξ_2 is not as evident, but will be made clear presently. As can be seen from Eq. [20], the parameters ξ_m contain the term Δn, which, according to Eq. [6] contains the function sinc $[(KW/2)(\sin\phi - \sin\phi_o)]$. For a small angular deviation $\Delta\phi$, this function can be written as sinc $[(KW/2)\Delta\phi]$ where $\Delta\phi = \phi - \phi_o \cong \sin\phi - \sin\phi_o$. Although the deviation $\Delta\phi$ represents a range of angles within the spread function of the acoustic beam, it can be shown to be proportional to a change $\Delta\overline{\theta}_{-1}$ of $\overline{\theta}_{-1}$ with frequency. Fig. 5 is a graphical description of the law of conservation of momentum for the acousto-optic interaction regarded as a collision process. The wave vectors $\mathbf{k}_o n_o$ of the incident wave, $\mathbf{k}_{-1} n_o$ of the first-order diffracted wave and $\mathbf{K}_B$ of the acoustic wave satisfy the vector relation $\mathbf{k}_o n_o = \mathbf{k}_{-1} n_o + \mathbf{K}_B$ represented by the triangle OAB. Since $|\mathbf{K}_B| \ll |\mathbf{k}_o n_o|$, the triangle is isosceles, with $|\mathbf{k}_o| = |\mathbf{k}_{-1}|$. If the direction of $\mathbf{K}_B$ is changed by $\Delta\phi$, its length must change so that its tip is at A′, and the direction of the diffracted wave change to $\mathbf{k}'_{-1} n_o$ to form the new isoceles triangle OA′B. Since $|\mathbf{k}_o| = |\mathbf{k}_{-1}| = |\mathbf{k}'_{-1}|$ it is clear that the points B, A and A′ must lie on the circumference of a circle of radius $|\mathbf{k}_o|$ and centered at O. Thus as the tip of $\mathbf{K}_B$ sweeps the arc AA′ through the angle $\Delta\phi$ with its apex on the circumference, the tip of the $\mathbf{k}_{-1} n_o$ vector sweeps the same arc through the angle $\Delta\bar{\theta}_{-1}$ with its apex at the center of the circumference. Consequently

$$\Delta\phi = \frac{1}{2} \Delta\bar{\theta}_{-1}. \qquad [31]$$

However, in order to change the length of $\mathbf{K}_B$ it is necessary to change the acoustic frequency. Thus the interpretation of Fig. 5 is as follows. As the acoustic frequency changes by Δf, the first-order light direction changes according to Eq. [28]. However, because of the natural spread of the acoustic $\mathbf{K}$ vector over a range given by $\mathbf{K}_B + \Delta\mathbf{K}$, only the component that is displaced from the direction ϕ_o by $\Delta\phi$ is effective in the acousto-optic interaction. Therefore $\Delta\phi$ is equivalent to a change of frequency in accordance with Eqs. [28] and [31], and Eq. [6] can now written

$$\Delta n = -\left[\frac{M_2 P_d}{2}\right]^{1/2} \operatorname{sinc}\left(\frac{1}{4} K W \Delta\bar{\theta}_{-1}\right). \qquad [32]$$

The above consideration together with the fact that $|\Delta\mathbf{K}| = |\mathbf{K} - \mathbf{K}_B|$ establishes the explicit frequency dependence of Eq. [25], which is now written as

$$\eta_1 = \frac{\operatorname{sinc}^2 U_1}{\operatorname{sinc}^2 U_1 + V_1^2} \sin^2 \{\xi_o W [\operatorname{sinc}^2 U_1 + V_1^2]^{1/2}\},$$

$$[33]$$

$$\eta_2 = \frac{\operatorname{sinc}^2 U_2}{\operatorname{sinc}^2 U_2 + V_2^2} \sin^2 \left\{\frac{1}{4} \xi_o W [\operatorname{sinc}^2 U_2 + V_2^2]^{1/2}\right\},$$

where

$$U_1 = -\frac{\pi}{2}a(a-1)r \qquad V_1 = \frac{U_1}{\xi_o W}$$

$$U_2 = -\frac{\pi}{2}a(2a-1)r \qquad V_2 = \frac{4U_2}{\xi_o W}$$

$$[34]$$

$$\xi_o = \frac{k_o}{2\cos\overline{\theta}_o}\left[\frac{M_2 P_d}{2}\right]^{1/2} \qquad a = \frac{K}{K_B} = \frac{f}{f_B}$$

$$r = \frac{W}{W_{BM}} = \left(\frac{f_B}{f_{BM}}\right)^2 \qquad W_{BM} = \frac{2\pi k_o n_o}{K_B{}^2} = \frac{n_o \Lambda_B{}^2}{\lambda_o}$$

$$f_{BM} = \sqrt{\frac{v^2 n_o}{\lambda_o W}}$$

The expression for η_1 is valid for the normalized frequency a in the neighborhood of unity, and the one for η_2 is valid for a in the neighborhood of 1/2. The parameter ξ_o is a "coupling constant" that is a function of the acoustic power, and the product $\xi_o W$ will sometimes be referred to as the "excitation". The parameter r, which is the ratio of the actual acoustic beam width to the minimum width suitable for operation in the Bragg regime, is a measure of how deep in the Bragg regime the interaction occurs. It is also the square of the ratio of the actual Bragg frequency to the minimum Bragg frequency for a deflector of acoustic width W. Its value should always be > 1. The larger it is, the wider the separation between the circles in the dispersion diagram and the deeper the operation in the Bragg regime. Fig. 6 is a plot of η_1 and η_2 versus frequency for $r = 2$ and several values of $\xi_o W$ or acoustic power. Fig. 7 is a plot for $\xi_o W = 1$ and several values of r. From these plots, the following observations can be made. The efficiency in the first order reaches its peak at $a = 1$ (i.e., $f = f_B$, where its value is $\eta_1 = \sin^2(\xi_o W)$. The fractional bandwidth Δa_B between the half-power points is a function of the acoustic power and of the value of r. The dependence on r is much more drastic than the dependence on the acoustic power; as can be seen in Fig. 7, the higher r (i.e., the deeper the operation in the Bragg regime), the narrower the fractional bandwidth. The second-order efficiency peaks at $a = 1/2$ and

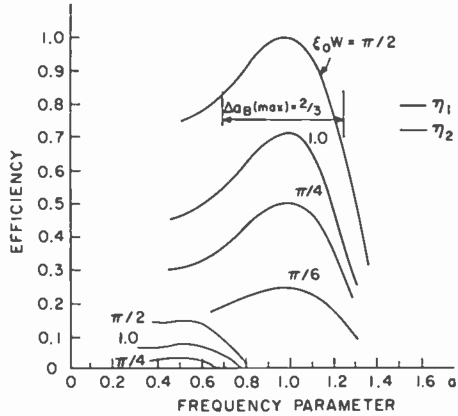

Fig. 6—Intensities of the first- and second-order diffracted lights as a function of frequency for $r = 2$ and for several values of the excitation $\xi_o W$.

has a value given by $\eta_2 = \sin^2(\xi_o W/4)$, regardless of r. This peak, which according to Fig. 7 is significant compared to the corresponding value of η_1, occurs at the location occupied by the first-order beam when a had the value of unity. The independence of η_2 (peak) from r is in disagreement with the results of Coquin et al[12] who in their Fig. 3 and 4 show η_2 to decrease with increasing r (γ in that reference) and to have a peak at $a \neq 1/2$. Our analysis reveals that the incidence angle satisfying the first-order Bragg condition at $a = 1$ also satisfies the

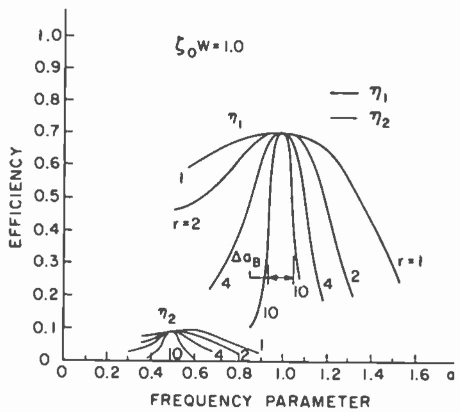

Fig. 7—Intensities of the first- and second-order diffracted lights as a function of frequency for $\xi_o W = 1$ and for several values of r.

second-order Bragg condition at $a = 1/2$, and that the value of r affects only the bandwidth of η_2, not its peak amplitude. The discrepancy between our results and those of Coquin et al stems from the fact that these authors used the Raman–Nath Eq. [14] for their computer calculations. The same equations were used by Klein and Cook[21] to find numerical solutions in the so-called "intermediate region" between the Raman–Nath and the first Bragg regime. However, it has already been shown in the present work that Eq. [14], obtained by substituting Eq. [9] into Eq. [5], cannot describe the problem in the second Bragg regime because Eq. [9] is *not* a solution to Eq. [5] in that regime. The coefficients in Eq. [9] must be obtained from Eq. [11]; the solution for the second-order beam in AO deflectors is given by A_{-m} in Eq. [22] with $m = 2$, and the relative second-order efficiency is given by η_2 in Eq. [33].

From a device viewpoint the following comments are in order. For $r > 3$, the bandwidths of both the first- and second-order beams are narrow and do not overlap appreciably. The bandwidth of the deflector is $\Delta f_B = f_b \Delta a_B$, where Δa_B is the fractional bandwidth of η_1. For $r < 3$ there is appreciable overlap between the two orders in the region $a < 1$. It is a simple exercise to verify that in order to keep the second order outside of the field of view of a deflector whose output is the first order, we must have $2/3 < a < 4/3$, i.e., $\Delta a_B = 2/3$. Thus the largest bandwidth Δf_B (max), obtained when $r = 1$, is then

$$\Delta f_B(\text{max}) \cong \frac{2}{3} f_{BM}, \qquad [35]$$

where f_{BM} is the minimum Bragg frequency, defined in Eq. [34]. An examination of the expression for η_1 in Eq. [33] and for f_{BM} in Eq. [34] indicates that, for a given λ_o and a given AO material, f_{BM} can be increased only by reducing W. However, for a given ξ_o determined by the available acoustic power, reducing W also reduces η_1.

In order to increase the resolution Eq. [30], it is necessary to increase the transit time τ (reduce the speed) and/or the bandwidth. The latter cannot be increased without reducing the efficiency. Thus the resolution of an ordinary AO deflector can be increased only at the cost of speed and/or efficiency.

These limitations can be overcome by "acoustic beam steering", according to which the first-order Bragg condition is maintained over a relatively large frequency range Δa_D by causing the acoustic column to rotate and automatically track the Bragg angle as the acoustic frequency is varied. The situation is similar to the automatic tuning of a highly selective receiver over a broad dynamic range Δf_D. The simplest method of beam steering is to design the transducer in a grating configuration with 180° phase difference between transducer elements and to use the first acoustic spectral order as the steering beam. Although the position of the first-order acoustic beam is not a linear function of frequency, as it would need to be for perfect tracking, an optimum design is achievable that results in a dynamic range that is significantly larger than the Bragg bandwidth of a deflector with fixed acoustic beam.

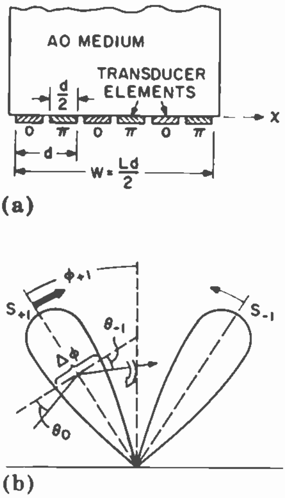

Fig. 8—(a) Transducer array with π phase shift between elements and (b) polar plot showing application of S_{+1} to beam-steering deflectors.

4. First-Order Beam Steering

4.1 Transducer Array

Consider an array of L transducer elements, each of width $d/2$, bonded to the AO medium, occupying a total width $W = Ld/2$, and emitting sound with 180° phase shift between adjacent elements, as shown in Fig. 8a. Such an array can be regarded as a grating of period d and aperture W upon which an acoustic strain wave of magnitude S_o is impinging at normal incidence. As usual the transmitted sound $S(x,z)$ is of the form

$$S(x,z) = \sum_n S_n \exp\{i(n2\pi/d)x\} \exp\{ik \cos\phi_n z\} \qquad [36]$$

representing a set of waves of amplitude S_n traveling in different directions ϕ_n. These directions are found by writing $n2\pi/d = K \sin \phi_n$. This gives $\sin \phi_n = n2\pi/Kd = n\Omega/d = nv/fd$. The Fourier amplitudes S_n for this case have a peak equal to $2/n\pi$ for n odd and to zero for n even. Since the width of the incident sound beam is finite in the x direction, a Fourier transform of Eq. [36] gives the output angular distribution $S(\phi,z)$. For the geometry under consideration, only the $n = +1$ and $n = -1$ components have significant magnitudes, i.e.

$$S(\phi,z) = [S_1(\phi) \exp\{iK \cos \phi_1 z\} + S_{-1}(\phi) \exp\{iK \cos \phi_{-1} z\}] \qquad [37]$$

where

$$S_{\pm 1} = \pm \frac{2}{\pi} S_o \operatorname{sinc}\left[\frac{KW}{2}(\sin \phi - \sin \phi_{\pm 1})\right], \qquad [38]$$

and

$$\sin \phi_{\pm 1} \cong \phi_{\pm 1} \cong \pm \frac{v}{fd}. \qquad [39]$$

In the power spectrum of Eq. [37], each of the two beams contains an amount $(2/\pi)^2$ or 42% (4dB insertion loss) of the total acoustic intensity, with a half-power angular width given by

$$\delta\phi \cong \frac{\Lambda}{W} = \frac{v}{fW}. \qquad [40]$$

A polar plot of $S(\phi,z)$, shown in Fig. 8b, illustrates how one of the beams can continuously satisfy the Bragg condition as the acoustic frequency varies. As the frequency increases, S_{+1} rotates clockwise (heavy arrow) and S_{-1} counterclockwise (thin arrow). A light incident at an angle $\overline{\theta}_o$ on S_{+1} is diffracted at the angle $\overline{\theta}_{-1}$. This angle changes in the clockwise direction, indicated by the double arrow, as the frequency increases. It is clear that only beam S_{+1} is suitable for tracking because only it rotates in the proper direction to track the Bragg angle. In order to prevent beam S_{-1} from spuriously rescattering the diffracted light, it is necessary to choose a grating period d that will effectively separate the two acoustic columns, and to operate in a frequency range that is deep in the Bragg region in order to have high selectivity in the scattering by S_{+1}. The spurious interference by

S_{-1} was a discouraging problem to Korpel et al[7] who worked with water deflectors in the 20-MHz range. It is of no significance in our work, which was carried out in the 100-260 MHz range.

The beam S_{-1} was completely eliminated by Korpel et al by constructing the transducer array in the staircase arrangement of Fig. 9, where the height of each step is equal to half the acoustic wavelength Λ_0 at the center of the frequency band. By means of this arrangement,

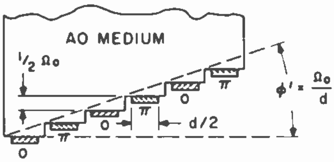

Fig. 9—Staircase array to eliminate spurious acoustic beam S_{-1}.

the acoustic wavefront is tilted by the angle $\phi' = \Lambda_0/d$, and it can be shown by Fourier transform that the amplitude of the S_{-1} becomes negligible. Although this approach utilizes all the incident sound power, it is very difficult to construct for high-frequency operation. The height of each step is only a few micrometers and must be ground accurately and polished to optical flatness. Each transducer section must be bonded at a pressure of several thousand psi, then lapped and polished, and so on. These considerations, together with the fact that the best AO materials cleave easily under stress, that the bond yield is low, and that the transducers may break during the lapping process, are convincing arguments that the stepped array is to be avoided at high frequencies. On the other hand, there exist geometrical configurations that make it possible to construct flat transducer arrays from a single bonded transducer of a given width. Although the grating efficiency in this case is only 42%, the equivalent 4-dB insertion loss is a value that is quite acceptable in transducer applications. Our work on beam steering deals exclusively with the flat array.

Our flat array is made from a single transducer. Normally the transducer is bonded to the AO material by evaporating a thin layer (less than 5000 Å) of indium on the faces to be bonded. The latter are then joined together under a pressure of about 4000 psi. One method of making the grating is shown in cross section in Fig. 10a. After the transducer has been bonded and lapped to its final thickness, grooves are cut through it and through the bond in order to make electrically insulated sections of width d. These sections will correspond to the grating period. Each section is covered by two adjacent metallic electrodes making up elements of width slightly less than $d/2$. The electrodes adjoining a groove are linked together electrically, and the two extreme electrodes are connected to the rf source. Any type of electrode may be used, e.g., a layer of silver paste painted on the surface with a brush or a layer of metal evaporated through a mask in a vacuum system. The grating effect is obtained in the following manner. The poling direction in the piezoelectric material has a component normal to the transducer surface, represented by the heavy arrow in Fig. 10a. The manner of interconnecting the electrodes

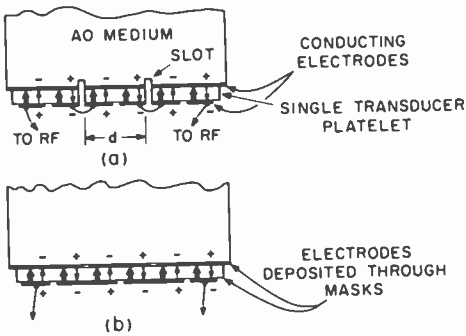

Fig. 10—Construction of flat array from single transducer platelet (a) by segmenting the platelet and (b) by staggering the electrodes.

causes the instantaneous polarity of the voltage across each element to alternate in space, as indicated by the + and − signs; and the electric field direction to alternate in a similar fashion, as indicated by the thin arrows. Thus the electric field is parallel to the poling direction in one element and anti-parallel to it in the next, causing one element to contract and the other to expand at any given time. When the electric field varies at the frequency of the rf source, the particle displacement is in opposite directions in adjacent transducer elements at all frequencies, and the resultant overall acoustic wave emitted by the array exhibits the 180° phase shift from element to element, as indicated earlier in this section.

The attractiveness of this design is that *any* fixed-beam single-transducer deflector can be converted into a beam-steering device. Another, somewhat neater, method of making the array is shown in Fig. 10b. Here no grooves are cut in the structure, but the geometrical pattern of the bond and the external electrodes are staggered across the transducer to make up the grating without the use of additional connection. It must be noted that, beside its beam-steering ability, the grating design described in this paper is also an impedance transformer with impedance ratio equal to L^2 when compared to a single transducer having the same overall area. This is so, because the array consists of a series connection of L elements, the impedance of each element being L times the impedance of a single transducer of the same area as the whole array. With the area of acoustic columns used in AO deflectors operating in the 100 to 300 MHz region, the impedance of the single transducer is only a few ohms. By suitable choice of the number of elements, the impedance can be brought closer to the 50 to 75 ohm impedance level of most rf sources.

4.2 Tracking

It is recalled from the momentum diagram (Fig. 5) that in order to satisfy the Bragg condition as the acoustic wave vector **K** changes, the latter must always be a chord of a circle of radius $k_o n_o$ and satisfy the relation $\Delta\phi = \Delta\bar{\theta}_{-1}/2$. This implies that the rate of change of ϕ and $\bar{\theta}_{-1}$ with frequency must be such that $d\phi/df = (1/2)d\bar{\theta}_{-1}/df$, a condition that cannot be fulfilled by the first-order acoustic beam, since from Eq. [39] $d\phi_1/df \propto 1/f^2$, whereas from Eq. [28] $d\bar{\theta}_{-1}/df$ is a constant. However, a more relaxed tracking condition can be expressed if the acoustic spread between the half-power points are taken into consideration. Let us define two functions $\phi_L = \phi_1 - (1/2)\delta\phi$ and $\phi_H = \phi_1 + (1/2)\delta\phi$, where ϕ_1 and $\delta\phi$ are given by Eqs. [39] and [40], respectively, and let us require that the variations of $\bar{\theta}_{-1}$ be within those of $2\phi_L$ and $2\phi_H$. By choosing a reference Bragg frequency f_B (for alignment purpose) and the dummy variable a as before, where $a = f/f_B$, the following expressions can be written:

$$\begin{aligned}
\phi_1(a) &= \frac{1}{a}\phi_{1B}, \\
\phi_L(a) &= \frac{1}{a}\left[\phi_{1B} - \frac{1}{2}\delta\phi_{1B}\right], \\
\phi_H(a) &= \frac{1}{a}\left[\phi_{1B} + \frac{1}{2}\delta\phi_{1B}\right], \\
\bar{\theta}_{-1}(a) &= \bar{\theta}_{oB}[1 - 2a],
\end{aligned} \qquad [41]$$

where

$$\phi_{1B} = \frac{v}{f_B d},$$

$$\delta\phi_{1B} = \frac{v}{f_B W}, \qquad [42]$$

$$\bar{\theta}_{oB} = \frac{\lambda_o}{2n_o v} f_B$$

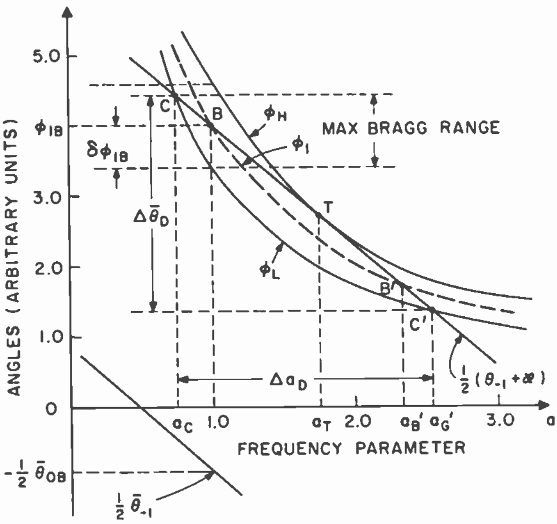

Fig. 11—Plot showing dynamic range Δa_D in deflectors with first order acoustic beam steering.

The functions ϕ_L, ϕ_1, ϕ_H and $\bar{\theta}_{-1}/2$ are plotted in Fig. 11. In order to compare them, the function $\theta_{-1}/2$ can be translated by a constant $\kappa = 2\phi_{1B} + \bar{\theta}_{oB}$, so that $(1/2)[\bar{\theta}_{-1} + \kappa]$ intersects the curve for ϕ_1 at the point B where the exact Bragg condition is fulfilled. The relaxed tracking condition can now be written in the form of the inequality

$$\phi_L(a) \leqslant \frac{1}{2} [\theta_{-1} + \kappa] \leqslant \phi_H(a)$$

or

$$\frac{1}{a}\left[\phi_{1B}-\frac{1}{2}\,\delta\phi_{1B}\right]\leqslant[(1-a)\bar{\theta}_{oB}+\phi_{1B}]\leqslant\frac{1}{a}\left[\phi_{1B}+\frac{1}{2}\,\delta\phi_{1B}\right]. \qquad [43]$$

From Fig. 11 it is clear that the maximum tracking range is obtained when $(1/2)[\bar{\theta}_{-1}+\kappa]$ is tangent to $\phi_H(a)$ at some point T, i.e., when the equation

$$(1-a)\bar{\theta}_{oB}+\phi_{1B}=\frac{1}{a}\left[\phi_{1B}+\frac{1}{2}\,\delta\phi_{1B}\right]$$

has a double root. This condition for the double root establishes the optimum value of the grating period d. The dynamic bandwidth and angular range are obtained from the intersects of $(1/2)[\bar{\theta}_{-1}+\kappa]$ with $\phi_L(a)$ at the points C and C′, i.e., from the roots of

$$(1-a)\bar{\theta}_{oB}+\phi_{1B}=\frac{1}{a}\left[\phi_{1B}-\frac{1}{2}\,\delta\phi_{1B}\right].$$

One obtains

$$\begin{aligned} a_T &= 1+1/\sqrt{r},\\ a_C &= 1-0.41/\sqrt{r}=a_T-\sqrt{2/r},\\ a_C{}' &= 1+2.41/\sqrt{r}=a_T+\sqrt{2/r}, \end{aligned} \qquad [44]$$

together with the expressions

$$\begin{aligned} d &= \frac{2W}{r(1+2/\sqrt{r})},\\ f_T &= a_T f_B = a_T\sqrt{r}f_{BM},\\ \Delta f_D &= \frac{2\sqrt{2}}{1+\sqrt{r}}f_T = 2\sqrt{2}\,f_{BM},\\ \Delta\bar{\theta}_D &= 4\sqrt{2/r}\,\bar{\theta}_{oB}, \end{aligned} \qquad [45]$$

where a_T, a_C and $a_C{}'$ are the values of the frequency parameter a at the tangent and intersect points referred to in Fig. 11, d is the grating period, f_T the frequency at the tangent point (which turns out to be the center frequency), Δf_D the dynamic bandwidth, and $\Delta\overline{\theta}_D$ the dynamic angular range in the AO medium.

The following conclusions can be drawn from the analysis:

1. The most important result is that the dynamic bandwidth is a *constant* whose value $\Delta f_D = 2\sqrt{2}\, f_{BM} = 2\sqrt{2}[v^2 n_o/(\lambda_o W)]^{1/2}$ is determined only by the optical wavelength λ_o, the acoustic beam width W, and material properties of the AO medium. This bandwidth is achievable when the incident light and the S_1 acoustic beam satisfy the Bragg condition at the reference frequency f_B, i.e., when the new incidence angle θ_i in air is

$$\theta_i = n_o[\overline{\theta}_{oB} + \phi_{1B}] \, . \qquad [46]$$

2. Comparing Δf_D to the maximum Bragg bandwidth $\Delta f_B \cong (2/3) f_{BM}$ of the deflector without beam steering, it is clear that $\Delta f_D/\Delta f_B \cong 4.24$ for a given value of transit time τ. Thus the performance of the beam-steered deflector is more than four times higher than that of the standard Bragg deflector.

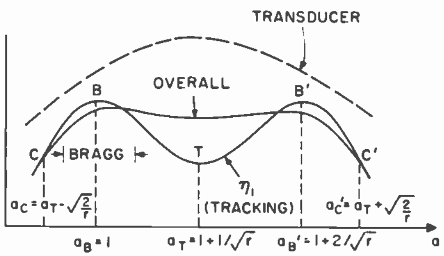

Fig. 12—Combined response of beam-steering tracking and of transducer.

3. The tangent point T corresponds to a half-power point at mid-band, and there are two points where the Bragg condition is fulfilled exactly, namely, the points B and B′ in Fig. 11. Hence the dynamic bandwidth has the three half power points denoted by C, T and C′, and two peaks denoted by B and B′ in Fig. 11. The overall response however is fairly flat due to the compensating effect of the transducer at mid-band as shown in Fig. 12.

4. Another important result of this analysis is the conclusion that, since the transducer grating can be made from a single transducer chip by the simple process of segmenting it and interconnecting the segments, any Bragg deflector can be easily converted to a beam-steering deflector with a fourfold improvement of performance.

4.3 Design

Based on the analysis presented above, there are three constraints that must be observed in the optimum design of beam-steering AO deflectors:

1. The grating spacing d must be smaller than the acoustic beam width W, preferably by a factor equal to an integer in order to minimize secondary spurious responses from the acoustic grating.
2. In an optimum design, the choice of the parameter r must be such that the dynamic bandwidth Δf_D is smaller than the transducer bandwidth Δf_T in order that the overall bandwidth be equal to the dynamic bandwidth. If Δf_T is less than Δf_D, the performance of the deflector is limited by the transducer bandwidth, and will not be optimum.
3. Since the frequency response is symmetric with respect to the tangent point a_T or f_T, the center frequency of the transducer should be at the tangent point.

From the fact that $W = Ld/2$ and the value of d given by Eq. [45], it is clear that L must be an even integer equal to $r[1 + (2\sqrt{/r})]$; or that r be given by

$$r = L + 2 \pm 2\sqrt{L+1}, \qquad [47]$$

where L is an even integer. Either of the two values of r from Eq. [47] is acceptable provided $r \geqslant 1$. However, when both values are >1, the smaller one should be chosen because it makes the transducer easier to fabricate.

As shown in Appendix 2, the bandwidth of transducers made from piezoelectric lithium niobate is quite large, of the order of $\Delta f_T \cong 1.4 f_T$ with proper acoustic loading. The effective dynamic bandwidth is the smaller of Δf_T and Δf_D. If $\Delta f_D < \Delta f_T$ the performance of the deflector is optimum, with dynamic bandwidth equal to Δf_D; if, however, $\Delta f_D > \Delta f_T$, the performance is limited by the transducer's bandwidth. It can be verified that $L \geqslant 4$ is desirable. The value $L = 4$ is the crossover point between optimum performance and transducer-limited performance, because it makes $r = 1.54$ and $\Delta f_D = 1.26 f_T$.

5. Results

5.1 Fabrication

Several deflectors were made according to the flat-transducer-array design described in the preceding sections with lead molybdate as the AO medium and 36° rotated Y-cut lithium niobate[29] as transducer material. Some samples were also made with SF 59 glass as the AO medium, but emphasis was placed upon lead molybdate because of its high figure of merit and low acoustic absorption in the upper range of operation of our transducers (around 300 MHz). The transducer is indium-bonded to the AO material as *one single* large platelet of area 5 by 10 mm and thickness 0.5 mm. In the usual indium-bonding technique, chromium, gold, and indium are evaporated (in that order) onto the surfaces of the AO and of the piezoelectric materials to be bonded, and the two are brought together in vacuum under a pressure of about 4000 psi.[22,23] This procedure does not work well with lead molybdate because of poor adhesion with chromium. Heating, which usually overcomes the poor adhesion problem, is not recommended because lead molybdate is highly susceptible to damage due to thermal stress. The problem was solved by substituting molybdenum for chromium, because it was observed experimentally that molybdenum adheres to lead molybdate much more strongly than does chromium. To further improve adhesion, the lead molybdate and lithium niobate surfaces to be bonded were polished to a mat quality prior to metallization and bonding. The roughness of the mat surface was about one micrometer, enough to scatter light, but still extremely smooth to acoustic waves at the frequencies of operation of our devices. This technique has resulted in bonding yields in excess of 80%. Following the bonding operation, the transducer platelet is lapped and polished to the half-wave thickness corresponding to the center of the chosen frequency range.

The segmenting scheme of Fig. 10a, was chosen for the sake of expediency because it is less elaborate than the scheme of Fig. 10b, although less neat. After the thickness reduction, the sample was sliced with a set of diamond-impregnated circular blades mounted on a jeweler's lathe. The electrode pattern was made by painting silver paste on the free surface of the transducer segments, and short pieces of thin wire jumpers held in place with silver paste were used to electrically join together the electrodes adjacent to the slits. A photograph of a typical grating having $L = 4$, $W = 8$ mm, $H = 4$ mm is shown in Fig. 13.

The rf power was provided by an rf sweeper feeding an rf power amplifier with an output of 0.5 watt into 50 ohms over the frequency range from 10 to 300 MHz. The sample was connected to the amplifier without tuning elements, although a broadband transformer was used sometimes to bring the sample's impedance closer to the amplifier's 50-ohm level. The untuned connection, as seen in Appendix 2, has a broader bandwidth than the tuned configuration, although the inser-

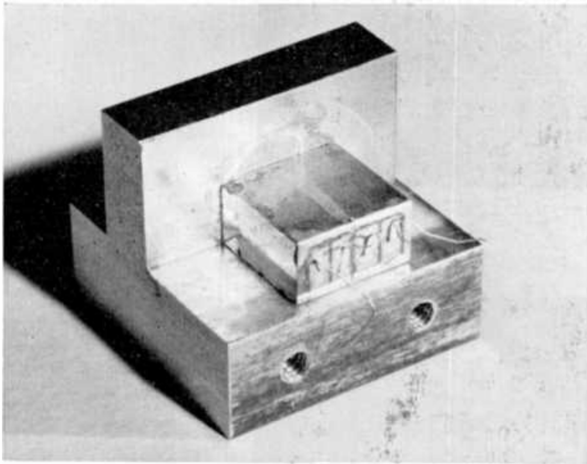

Fig. 13—Photograph of a four-segment (two-period) grating with electrical interconnections.

tion loss is higher. A 4-milliwatt HeNe laser ($\lambda_o = 632.8$ nm) was used as a light source, and part of the diffracted output light was directed to a solar cell acting as a photodetector. The output of the solar cell was fed to an oscilloscope whose horizontal sweep was controlled by the sweep generator. With this arrangement it was possible to display the whole frequency spectrum of the device.

The mechanical lapping and polishing set-up used in our work made it possible to readily achieve a transducer thickness of about 23 μm, which corresponds to a mechanical resonant frequency of about 150 MHz. With such a low center frequency, we expected our deflectors to be transducer-bandwidth limited. Optimum performance would be obtained if the transducer were thinner, but our set-up was not equipped to make thinner transducers with realiably uniform thickness. Very thin transducers can be made by sputtering the transducer platelets or by use of evaporated cadmium sulfide or zinc oxide transducers.

5.2 Experimental Results

The results for a typical lead molybdate sample are shown in Fig. 14. The transducer width was 8 mm, its center frequency 150 MHz, and its overall bandwidth Δf_T of 210 MHz ($\Delta f_T \cong 1.4\, f_T$). This bandwidth

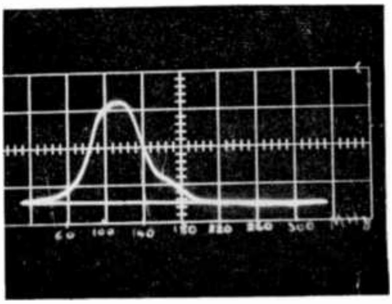

(a)

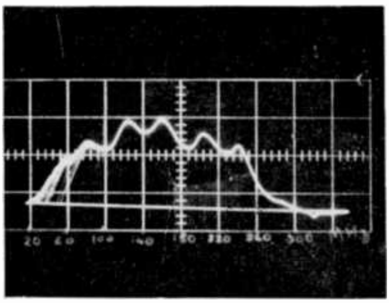

(b)

Fig. 14—(a) Oscillogram showing swept response of standard Bragg deflector with $W = 8$ mm and (b) oscillogram for the same sample after segmentation of transducer for operation in beam-steering mode.

was achieved by acoustically loading the free transducer surfaces with additional silver paste in order to make it appear symmetrically loaded (see Appendix 2). The sample was tested first as an ordinary fixed-beam deflector at the Bragg frequency of 115 MHz. Afterwards the transducer was segmented and interconnected according to Fig. 13, and the sample was then tested in the beam-steering mode. In the first, ordinary case, the bandwidth was 54 MHz, as shown in Fig. 14a. In the beam-steering mode, the measured bandwidth between the upper and lower half-power points is about 210 MHz. Note that this bandwidth is equal to the transducer bandwidth, i.e., it is transducer limited. The optimum dynamic bandwidth is supposed to be 240 MHz, a value that would be obtained if the transducer center frequency were 180 MHz or higher.

Despite the transducer limitation, the performance of the sample in the beam-steering mode was superior to that of the ordinary deflector by a factor of over 3.9. The performance of the device agrees well with theory, and it is clear that the full dynamic bandwidth would have been obtained if the transducer had been made thinner in order to operate at a higher center frequency.

In the sample, the acoustic beam width (transducer width) and, hence, the minimum Bragg frequency f_{BM} was chosen arbitrarily, and the acoustic power was left as an independent parameter that controls the efficiency. Such a design does not exploit the full potential of the deflector. Since f_{BM} is inversely proportional to the square root of the transducer width, the optimum design is one that will minimize the latter without sacrificing efficiency. In terms of the efficiency η_1 at the Bragg frequency, the transducer width can be written

$$W = 2\left[\frac{\lambda_o \cos\overline{\theta}_o \sin^{-1}\sqrt{\eta_1}}{\pi}\right]^2\left(\frac{H}{M_2 P_a}\right). \qquad [48]$$

For a given efficiency, the transducer width W can be minimized by reducing the transducer height H and by maximizing the acoustic power P_a. The choice of H depends on the overall optical system; if cylindrical lenses are allowed in the system, then H can be reduced to less than one millimeter. The acoustic power should be made as large as the deflector can tolerate. The maximum acoustic power can be several watts, depending on the strain limits and acoustic losses in the AO material; the strain limit causes physical damage to the material, and the acoustic losses cause optical distortion due to thermal gradients in the refractive index.

With the lowest value of W for a specified efficiency and maximum acoustic power, as in Eq. [48], the value of f_{BM} is maximized. This, in turn, requires an increase in the transducer center frequency, etc.

Performance of the deflector at shorter optical wavelengths is better than at longer ones. From Eqs. [34], [45], and [48], one obtains

$$\Delta f_D = \frac{2\pi v}{(\cos\overline{\theta}_o)(\sin^{-1}\sqrt{\eta_1})}\left[\frac{n_o M_2 P_a}{\lambda_o^3 H}\right]^{1/2}, \qquad [49]$$

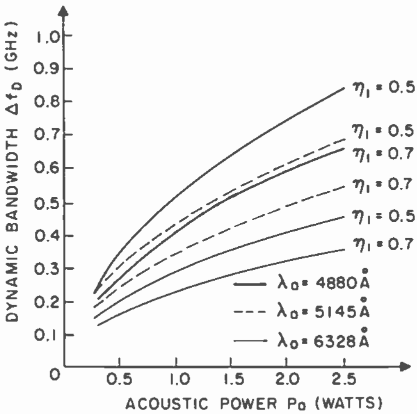

Fig. 15—Dynamic bandwidth capability of beam-steering deflector as a function of acoustic power, efficiency, and optical wavelength (AO material is lead molybdate and transducer height $H = 3.75$ mm).

which shows a $-3/2$ power dependence on λ_o. An additional, less explicit, dependence is embodied in the dispersion of the refractive index n_o and figure of merit M_2. Eq. [49] contains all the parameters that can be optimized if maximum bandwidth is a major goal. It is plotted in Fig. 15 as a function of acoustic power for two values of efficiency and three optical wavelengths. The appropriate values of n_o and M_2 for lead molybdate, taken from Pinnow's data,[15] are given in Table 2.

Table 2—Dispersion of n_o and M_2 for $P_bM_b0_4$[15]

λ_o(Å)	n_o	M_2 (sec³/kg)
6,328	2.395	$23.7 \times 1.51 \times 10^{-15}$
5,145	2.460	$28.9 \times 1.51 \times 10^{-15}$
4,880	2.495	$37.4 \times 1.51 \times 10^{-15}$

Optical polarization	x
Optical direction	y
Acoustic polarization and direction	z

The results can be impressive. With 2 watts of acoustic power and for an efficiency of 50% for 4880 Å light, the dynamic bandwidth is 740 MHz (obtainable if the transducer's center frequency is about 550 MHz). With a 10-mm diameter truncated Gaussian aperture the Rayleigh resolution is 1550 positions.

6. Conclusions

The proper application of diffraction theory to acousto-optic deflectors in which the output is the first-order diffracted light reveals that the second-order light is always important enough to limit the maximum bandwidth of ordinary Bragg deflectors. This maximum bandwidth is $(2/3)f_{BM}$, where f_{BM} is the minimum frequency for which a deflector of a given dimension can be considered to be in the Bragg regime for first-order diffraction. This frequency is a function of material constants, optical wavelength and acoustic beam width; furthermore it must be made low if high efficiency is desired, and vice versa. The resolution of the deflector, being proportional to its time–bandwidth product, can be increased only at the cost of efficiency, for a given deflector speed.

With acoustic beam steering, the bandwidth can be increased without decreasing the efficiency. When the steering beam is the first-order output from a transducer grating the 3-db dynamic bandwidth is $2\sqrt{2}\,f_{BM}$, an improvement of more than four over the best performance of ordinary fixed-beam deflectors.

Flat transducer arrays are more suitable for generating the steering acoustic column in AO media such as lead molybdate than are the stepped arrays reported by previous authors (although its acoustic output is only 42% of that of the stepped array) because the flat array is much easier to fabricate than the stepped array. It can be made from a single transducer platelet by designing the electrodes in a pattern such that the electric field in successive array elements is either parallel or antiparallel to the transducer's poling direction. The bonding of large, single, transducer platelets to lead molybdate AO media has been a difficult task, but techniques are described that overcome the difficulties.

Several experimental deflectors with lead molybdate and flat lithium niobate transducer arrays were made according to the theory and design procedures developed in this paper. Results from both fixed-beam and beam-steering operations confirm that a four-fold improvement of performance can be obtained if the transducer's electrical bandwidth is larger than the expected dynamic bandwidth; furthermore the method of fabrication reveals that any ordinary Bragg deflector can be converted from the low-performance fixed-beam mode to the high-performance beam-steering mode of operation.

Acknowledgments

The author gratefully thanks G. E. Bodeep for his invaluable technical assistance in the construction and testing of the samples and G. W. Leck and R. Pratt for the construction of the indium bonding apparatus and for their role in device fabrication. Acknowledgment is also extended to R. S. Mezrich and C. W. Wine for their help in computer programming, to W. C. Stewart for technical discussions during part of this project and to R. C. Alig for reviewing the manuscript. Sincere thanks are also expressed to J. A. Rajchman and R. D. Lohman for encouraging and supporting this work.

Appendix 1—Photoelastic Effect

The photoelastic effect is the change ΔB of the indicatrix B of a material as a result of stress or strain. The indicatrix is a second-rank tensor representing the inverse of the dielectric permittivity tensor $\mathcal{E}$. Its components B_{ij} are given by[24]

$$B_{ij} = \mathcal{E}_o \frac{\partial E_i}{\partial D_j}, \qquad [50]$$

where $\mathcal{E}_o$ is the free-space permittivity and E_i and D_j are components of the electric field and displacement, respectively. The change ΔB_{ij} in the indicatrix is related to the strain S_{kl} through the dimensionless fourth-order photoelastic tensor p_{ijkl} according to the relation

$$\Delta B_{ij} = p_{ijkl} S_{kl}. \qquad [51]$$

In solving the wave equation, it is customary to deal with the dielectric tensor $\mathcal{E}$. Since the product $\mathbf{B}\mathcal{E} = 1$, it follows that $\Delta(\underset{\sim}{\mathbf{B}}\underset{\sim}{\mathcal{E}}) = 0$, i.e.,

$$\Delta\underset{\sim}{\mathcal{E}} = -\underset{\sim}{\mathcal{E}}\Delta\underset{\sim}{\mathbf{B}}\underset{\sim}{\mathcal{E}}, \qquad [52]$$

or

$$\Delta\mathcal{E}_{mn} = -\mathcal{E}_{mi}\Delta B_{ij}\mathcal{E}_{jn}. \qquad [53]$$

All tensors representing physical quantities are symmetrical, and equations that contain them can be reduced to simple matrix equations by means of a contracted notation that substitutes a single-matrix subscript for two-tensor subscripts according to the following scheme:

Tensor	11	22	33	23, 32	31, 13	12, 21
Matrix	1	2	3	4	5	6 .

According to this scheme a second-rank tensor reduces to a 1×6 column matrix, and a fourth-rank tensor reduces to a 6×6 matrix. In particular Eq. [51] becomes

$$\Delta B_i = p_{ik} S_k, \tag{54}$$

i.e.,

$$\begin{bmatrix} \Delta B_1 \\ \Delta B_2 \\ \Delta B_3 \\ \Delta B_4 \\ \Delta B_5 \\ \Delta B_6 \end{bmatrix} = \begin{bmatrix} p_{11} & p_{12} & p_{13} & \cdot & \cdot & \cdot \\ p_{21} & p_{22} & p_{23} & \cdot & \cdot & \cdot \\ p_{31} & p_{32} & p_{33} & \cdot & \cdot & \cdot \\ \cdot & \cdot & \cdot & p_{44} & \cdot & \cdot \\ \cdot & \cdot & \cdot & \cdot & p_{55} & \cdot \\ \cdot & \cdot & \cdot & \cdot & \cdot & p_{66} \end{bmatrix} \begin{bmatrix} S_1 \\ S_2 \\ S_3 \\ S_4 \\ S_5 \\ S_6 \end{bmatrix} . \tag{55}$$

Once the matrix components ΔB_i are obtained, the tensor components ΔB_{ij} are obtained as

$$\begin{bmatrix} \Delta B_{11} & \Delta B_{12} & \Delta B_{13} \\ \Delta B_{21} & \Delta B_{22} & \Delta B_{23} \\ \Delta B_{31} & \Delta B_{32} & \Delta B_{33} \end{bmatrix} = \begin{bmatrix} \Delta B_1 & \Delta B_6 & \Delta B_5 \\ \Delta B_6 & \Delta B_2 & \Delta B_4 \\ \Delta B_5 & \Delta B_4 & \Delta B_3 \end{bmatrix} . \tag{56}$$

Because of symmetry, some tensors like the strain tensor require factors of 1/2:[34]

$$\begin{bmatrix} S_{11} & S_{12} & S_{13} \\ S_{21} & S_{22} & S_{23} \\ S_{31} & S_{32} & S_{33} \end{bmatrix} = \begin{bmatrix} S_1 & \frac{1}{2}S_6 & \frac{1}{2}S_5 \\ \frac{1}{2}S_6 & S_2 & \frac{1}{2}S_4 \\ \frac{1}{2}S_5 & \frac{1}{2}S_4 & S_3 \end{bmatrix} . \tag{57}$$

From the above theory, the dielectric permittivity of a class $4/m$

crystal subjected to a uniaxial strain S_3 in the z direction is

$$\underset{\sim}{\mathcal{E}} = \begin{bmatrix} \mathcal{E}_1 - \mathcal{E}_1{}^2 p_{13} S_3 & 0 & 0 \\ 0 & \mathcal{E}_1 - \mathcal{E}_1{}^2 p_{13} S_3 & 0 \\ 0 & 0 & \mathcal{E}_2 - \mathcal{E}_2{}^2 p_{33} S_3 \end{bmatrix}. \qquad [58]$$

Appendix 2—Evaluation of the Elastic Strain

The acoustic network for an AO deflector consists of a piezoelectric transducer, a bonding layer and the AO medium on one side, and a metallic electrode on the free side, as shown in Fig. 16. The bonding

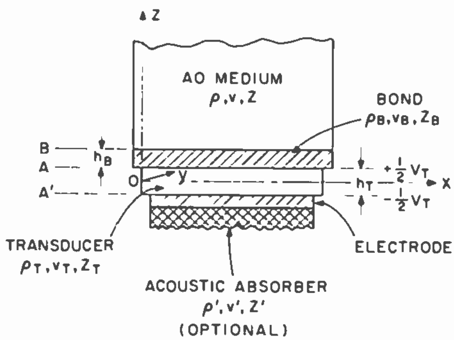

Fig. 16—Cross-section of AO deflector showing AO medium, bonding layer, transducer, and acoustic absorber on free surface of transducer.

layer is usually metallic and serves as the other electrode. When broad mechanical bandwidth is desired the free side may be acoustically loaded. The strain in the AO medium is obtained by solving the equation of motion for the particle displacement **l**, which is, in terms of the components l_i,

$$\rho \frac{\partial^2 l_i}{dt^2} = \frac{\partial T_{ki}}{\partial x_k}, \qquad [59]$$

where ρ is the density of the AO medium, T_{ki} is the component of the stress tensor $\underset{\sim}{\mathbf{T}}$, and x_k and t are the space and time variables ($x_{k \text{ or } i} = x, y, z$). The acoustic-wave equation for a medium is obtained from the relation

$$S_{ik} = \frac{\partial l_i}{\partial x_k}, \qquad [60]$$

where S_{ik} are the components of the strain tensor **S**, and from the constitutive relation

$$T_{ki} = C_{kimn} S_{mn}, \qquad [61]$$

where C_{kimn} are the components of the elastic stiffness tensor $\underset{\sim}{\mathbf{C}}$. The force vector **F** and particle velocity vector **U**, which are the acoustic analogues of voltage and current are given by

$$F_i = -(\mathbf{i} \cdot \underset{\sim}{\mathbf{T}}) A_T \text{ and } U_i = \frac{dl_i}{dt}, \qquad [62]$$

where **i** is the unit vector normal to the area A_T on which the force is exerted.

In the piezoelectric region, the constitutive relations must include the electric field and displacement. They are given by[25]

$$\underset{\sim}{\mathbf{T}} = \underset{\sim}{\mathbf{C}}^D \underset{\sim}{\mathbf{S}} - \underset{\sim}{\mathbf{h}}_t \underset{\sim}{\mathbf{D}}, \qquad [63]$$

$$\underset{\sim}{\mathbf{h}} \underset{\sim}{\mathbf{S}} = -\mathbf{E} + \underset{\sim}{\mathbf{B}}^S \underset{\sim}{\mathbf{D}}, \qquad [64]$$

where $\underset{\sim}{\mathbf{D}}$ is the electric displacement tensor, **E** the electric field vector (a tilde underneath a symbol indicates a tensor), $\underset{\sim}{\mathbf{C}}^D$ the elastic stiffness at constant charge density, $\underset{\sim}{\mathbf{B}}^S$ the dielectric impermeability at constant strain, and where $\underset{\sim}{\mathbf{h}}$, whose transpose is $\underset{\sim}{\mathbf{h}}_t$, is a tensor given by

$$\underset{\sim}{\mathbf{h}} = \underset{\sim}{\mathbf{d}} \underset{\sim}{\mathbf{C}}^E \underset{\sim}{\mathbf{B}}^S. \qquad [65]$$

In Eq. [65] $\mathbf{d}$ is the piezoelectric stress tensor and $\underset{\sim}{\mathbf{C}}^E$ is the elastic stiffness at constant electric field. When the particle displacement is uniaxial, the tensor equations reduce to simple scalar relations. In this work, all motion will be assumed to be in the z direction only. To evaluate the strain in the AO medium and relate it to the conditions at terminals of the rf sources, it is necessary to consider the propagation characteristics of the AO medium, the equivalent circuit of the transducer, and the insertion loss and bandwidth considerations.

2.A AO Medium

In the AO medium, assuming the particle velocity to be of the form

$$U_3(z,t) = \sqrt{2}\, \mathrm{Re}\, \{U(z) \mathcal{E}^{-i\Omega t}\}, \qquad [66]$$

where Re{ } ≡ Real part of, substitution of Eqs. [60] to [62] and [66] into Eq. [59] gives the wave equation:

$$\frac{d^2}{dz^2} U(z) + K^2 U(z) = 0. \qquad [67]$$

Here

$$K = \frac{\Omega}{v} \text{ and } v = [C_{33}/\rho]^{1/2} \qquad [68]$$

are the acoustic wave number and the longitudinal speed of sound, respectively. The fact that K is real means that the medium is assumed to be lossless.

At the boundary between the AO medium and the bonding layer, the normal component of particle velocity and the force are continuous. Since this velocity at point B in Fig. 16 is U_B, the solution in the AO medium, assumed to be infinitely long or properly terminated, is $U(z) = U_B \exp\{ikz\}$. This, together with Eqs. [60] and [62] gives the strain

$$S(z) = \frac{U(z)}{v} = \frac{U_B}{v} \exp\{iKz\} \qquad [69]$$

or

$$S_3(z, t) = \sqrt{2} \frac{U_B}{v} \cos(\Omega t - Kz). \qquad [70]$$

It can be shown that the force obeys the same wave Eq. [67] and that both the force and particle velocity obey the transmission line equations[26]

$$\frac{dF}{dz} = iKZU,$$
$$\qquad [71]$$
$$\frac{dU}{dz} = iKYF,$$

where

$$Z = \frac{1}{Y} = \rho v A_T = \frac{\Omega \rho A_T}{K} \qquad [72]$$

is the acoustic impediance of the AO medium of cross-section A_T. Since both F and U propogate as exp $\{iKz\}$ it follows that

$$F = ZU. \qquad [73]$$

It can also be shown that the acoustic power is

$$P_a = \text{Re}\,\{FU^*\}, \qquad [74]$$

where U^* is the complex conjugate of U. For the infiinite, lossless medium, $Pa = F_B U_B$, where F_B is the mechanical force at point B in Fig. 16. This gives

$$U_B = \left[\frac{P_a}{\rho v A_T}\right]^{1/2} = \left[\frac{P_d}{\rho v}\right]^{1/2} \qquad [75]$$

where $P_d = P_a A_T$ is the acoustic power density at the input of the AO medium.

Finally, the effect of the finite size of the transducer width W must be taken into account. This is done by considering the acoustic wave impinging upon the AO medium as an infinite plane wave incident at some angle ϕ_o on an aperture of width W. By means of Fourier transform, it can be shown that the wave is spread over a range of angles ϕ. Analytically this spread introduces the factor sinc $[(KW/2)\ (\sin\phi - \sin\phi_o)]$ in the expression for U_B at the boundary of the AO medium, giving the proper expression for the strain from Eq. [70] as

$$S_3(z,t) = \left[\frac{2P_d}{\rho v^3}\right]^{1/2} \text{sinc}\left[\frac{KW}{2}(\sin\phi - \sin\phi_o)\right] \cos\,(\Omega t - Kz). \qquad [76]$$

The actual value of P_d is affected by the transmission properties of the bonding layer and by the electromechanical conversion efficiency of the transducer. When the bonding-layer thickness is not negligible, its effect can be taken into account by considering it as a section of transmission line of length h_B (Fig. 16), characteristic impedance Z_B and propagation charcteristics $\gamma_B = \alpha_B - iK_B$. The attenuation constant α_B may or may not be zero, depending on the material used for the bond. If the bond is negligibly thin acoustically, the velocity at plane A in Fig. 16 is the same as that at plane B and both U_A and U_B are given by Eq. [75]. If the bond thickness is nonnegligible, U_B can be obtained from U_A by means of transmission line theory[27]; the result is that U_A is still given by Eq. [75], but U_B is now given by

$$U_B = U_A \mathcal{E}^{-\gamma_B h_B} [1 - \Gamma_B \mathcal{E}^{2\gamma_B h_B}], \qquad [77]$$

i.e., the factor $\mathcal{E}^{-\gamma_B h_B} [1 - \Gamma_B \mathcal{E}^{2\gamma_B h_B}]$ must be included in Eq. [76] for the strain. In Eq. [77], Γ_B is the reflection coefficient at the interface between the AO medium and the bond, given by

$$\Gamma = \frac{Z - Z_B}{Z + Z_B}. \qquad [78]$$

The acoustic impedance of the bond Z_B has the same form as Eq. [72], but with K replaced by $i\gamma_B$. The input impedance at the surface of the bond in contact with the transducer, which is also the equivalent acoustic load of the transducer at that mechanical port is

$$Z_A = Z_B \frac{Z + Z_B \tanh (\gamma_B h_B)}{Z_B + Z \tanh (\gamma_B h_B)}. \qquad [79]$$

This expression reduces to Z, the impedance of the AO medium, when the bond thickness is negiligible.

2.B Transducer

In the transducer, the particle velocity is in the standing-wave form

$$U_T(z) = C_1 \sin K_T z + C_2 \cos K_T z, \qquad [80]$$

where the subscript T identifies the velocity and wave number for the transducer, and the strain is, from Eq. [69], $S_T = U_T/v_T$, where v_T is the speed of sound in the transducer. From the effective terminal voltage V_T across the transducer electrodes and the current I_T supplied by the rf source, the electrical displacement D (obtained by the application of Gauss' law around one of the electrodes) and the electric field are obtained as

$$D = \frac{I_T}{j\Omega A}, \quad E\,(\pm h_T/2) = \pm \frac{V_T}{2h_T}. \tag{81}$$

When Eq. [81] is applied to the constitutive relations [63] and [64] and to the expression [62] for the force at the electrodes, the following relations are obtained:

$$\begin{aligned} F_A &= -i\left[\tan\left(\frac{K_T h_T}{2}\right)\right] Z_T U_A + \mathrm{i}\frac{Z_T}{\sin\,(K_T h_T)}(U_A + U_A) + \mathrm{i}\frac{h_{33}}{\Omega} I_T, \\ F_A' &= -i\left[\tan\left(\frac{K_T h_T}{2}\right)\right] Z_T U_{A'} + \mathrm{i}\frac{Z_T}{\sin\,(K_T h_T)}(U_A + U_{A'}) + i\frac{h_{33}}{\Omega} I_T, \end{aligned} \tag{82}$$

where $K_T = \Omega/v_T$ where $v_T = [C^D{}_{33}/\rho_T]^{1/2}$ is the speed of longitudinal sound in the transducer material, and $Z_T = \rho_T v_T A_T$ is the acoustic impedance of the transducer. Finally, integration of Eq. [64] with respect to z to get V_T yields

$$I_T = -i\Omega C_o V_T - \alpha\,(U_A + U_{A'}), \tag{83}$$

where $C_o = A_T/B_{33}h_T$ is the clamped capacitance of the transducer and $\alpha = h_{33}C_o$ the electromechanical transformation ratio. Fig. 17a shows an equivalent circuit satisfying Eqs. [82] and [83]. It is a three-port network with two mechanical ports and one electrical port, the electrical port being connected to the mechanical system by means of the ideal transformer with transformation ratio α. Usually a transducer is operated near one of its resonances, specifically the lowest one, and the free surface is either in contact with air or is loaded with some acoustic absorber. When the free surface is in contact with air, $Z_{A'}$ is set to zero because the air impedance is very much less than a solid. When it is loaded, the use of the equivalent circuit is more complicated except in the case of symmetric loading with $Z_{A'} = Z_A$. For both the air backed and symmetrically loaded structure, the equivalent circuit near the first resonance is shown in Fig. 18, obtained by using the transformation illustrated in Fig. 17b, together with the expansions

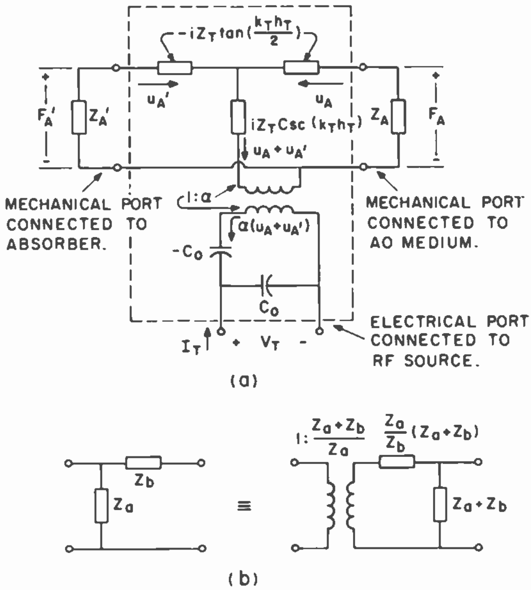

Fig. 17—(a) Equivalent circuit of piezoelectric transducer loaded at both surfaces and (b) transformation used to simplify equivalent circuit.

$$\tan\beta = -\sum_{l\ \mathrm{odd}} \frac{2\beta}{\beta^2 - \left[\dfrac{l\pi}{2}\right]^2}, \qquad [84]$$

and

$$\csc\beta = \frac{1}{\beta} + \sum_{l=1}^{\infty} \frac{(-1)^l 2\beta}{\beta^2 - (l\pi)^2}$$

near their poles $l\pi/2$ and $l\pi$, and retaining only the $l=1$ term. In the equivalent circuit of Fig. 18a, there is an electrical section consist-

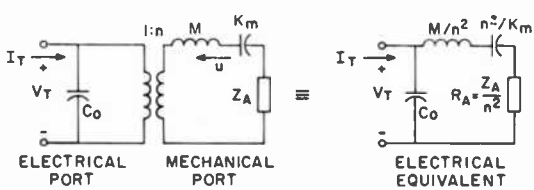

Fig. 18—Equivalent circuit of air-backed and symmetrically loaded piezoelectric transducer.

ing of the clamped capacitance C_0 and a mechanical section consisting of the series M, K_m, Z_A "circuit", where M is a fraction of the mass of the transducer, K_m the transducer stiffness, and Z_A is the acoustic load. The electrical and mechanical sections are coupled together through the electromechanical equivalent transformer of transformation ratio n. The values of M, K_m, Z_A, and n depend on the loading. They are given in Table 3 for the air-backed (abbr. AB) and symmetrically loaded (abbr. SL) systems.[28]

Table 3—Comparison of Air-Backed and Symmetrically Loaded Transducers

Quantity	Symbol and Unit	Air Back	Symmetrical Load
Transformation ratio	n[Newton/volt]	$n_{AB}=2e_{33}A_Th_T$ $=[C_{33}^D\mathcal{E}_o\mathcal{E}_r]^{1/2}A_Tk_Th_T$	$\frac{1}{2}n_{AB}$
Mass	M[kg]	$M_{AB}=\frac{1}{2}\rho_Th_TA_T$	$\frac{1}{4}M_{AB}$
Stiffness	K_m[Newton/meter]	$K_{mAB}=\pi^2C_{33}^DA_T/2h_T$	$\frac{1}{4}K_{mAB}$
Acoustic load	Z_A[kg/sec]	$Z_{AB}=Z\dagger$	$\frac{1}{2}Z$
Particle velocity	U[meter/sec]	$U_{AB}=U_A$	$2\,U_A$
Mechanical Quality factor	Q_m	$Q_{mAB}=\Omega M_{AB}/Z_{AB}$	$\frac{1}{2}Q_{mAB}$
Acoustic Power	P_a[watts]	$P_{aAB}=ZU_A^2$	$\frac{1}{2}P_{aAB}$
Resonant frequency	f_T[Hz]	$v_T/2h_T$	$v_T/2h_T$

† Z is the acoustic impedance of the AO medium if the bond is lossless and thin. Otherwise it must be replaced by Z_A from Eq. [82].

In Table 3, k_T is the mechanical coupling factor of the transducer. It is important to realize that the mechanical Q_m and the acoustic power in the AO medium for the symmetrical leading are one-half that of the air-backed transducer. Thus, the mechanical bandwidth of the symmetrical system is twice that of the air-backed system at the price of half the available acoustic power; the other half is lost in the back load. This point is important in the design of systems that call for maximum power or maximum bandwidth. The all-electrical equivalent circuit in Fig. 18b is useful for the purpose of making calculations. Note that the units of the electrical elements M/n^2, n^2/K_m and Z_A/n^2 are henrys, farads and ohms, since the MKS system is used throughout this paper.

2.C Insertion Loss and Overall Bandwidth

In the electrical driver–amplifier system feeding the transducer, the available power P_g is either specified or is easily calculated. Thus, the insertion loss between the rf source and the acoustic load must be known in order to determine the actual acoustic power P_a. The overall bandwidth of the system is also an important quantity since it ultimately affects the performance of the deflector. Both the bandwidth and the insertion loss are determined by the interconnecting network or filter between the transducer and the rf source. Among the several interconnection schemes that are possible, the simplest ones are the so-called "tuned" and "untuned" connections.

In the "tuned" connection an inductor L_o is connected across the trasducer. Its value is chosen such that it forms a parallel resonant circuit with the clamped capacitance C_o at the mechanical resonant frequency f_T. Thus, at resonance, the source sees a pure real impedance and the insertion loss I.L. is, assuming the source to be a voltage source,

$$\text{I.L. (tuned)} = 10 \log_{10} \frac{(R_g + R_A)^2}{4R_g R_A}, \qquad [85]$$

where $R_A = Z_A/n^2$ ohms. In evaluating R_A, care must be taken to use the value of Z_A and n from Table 3 that is appropriate to the type of loading used. The electrical bandwidth is

$$\Delta f_T \text{ (tuned)} = (2\pi R_A C_o)^{-1}. \qquad [86]$$

It can be verified that the electrical bandwidth in the "tuned" connection is in most cases less than the mechanical bandwidth. Moreover its value for the SL system is only half that of the AB system. Thus, although the mechanical bandwidth of an SL system is twice as large as that of the AB system, its overall bandwidth in the tuned configuration is only one-half that of the latter.

In the "untuned" configuration the transducer is connected directly to the source. It can be shown that the insertion loss at mechanical resonance is given by

$$\text{I.L. (untuned)} = 10 \log_{10} (R_g R_A / 4X_{Co}^2), \qquad [87]$$

where X_{Co} is the reactance of the transducer's clamped capacitance at resonance. The untuned insertion loss tends to increase at high mechanical resonant frequencies because of the decreasing value of

X_{Co}. However, it can be shown that the overall bandwidth is approximately equal to the mechanical bandwidth of the loaded transducer, i.e.,

$$\Delta f_T \text{ (untuned)} = \frac{2}{\pi} \frac{Z_A}{Z_T} f_T = \frac{1}{Q_m} f_T. \qquad [88]$$

Thus the "untuned" configuration is characterized by high insertion loss and broad bandwidth equal to the mechanical bandwidth. The maximum bandwidth in the "untuned" configuration is clearly obtained when the transducer is symmetrically loaded. The maximum bandwidth in this case is $\Delta f_T = (4/\pi)\, f_T$ when both loading media have the same acoustic impedance as the transducer itself. In practice the free surface of the transducer is loaded by covering its "free" metal electrode with a material that either scatters or absorbs sound. With lead molybdate as the AO medium and lithium niobate as the transducer, the ratio Z/Z_T is less than unity ($Z/Z_T = 25.9/34.5$). However, there is always some loss at the bond. With the additional broadening introduced by the bond, bandwidths as large as 1.4 f_T are still readily achievable.

With the dimensions discussed in the text, R_A for the unsegmented transducers is usually smaller than R_g. When the transducer is segmented into L segments connected in series; then R_A and X_{C_0} are increased by a factor of L^2, and the insertion loss is reduced. In particular for the untuned conection the insertion loss for the segmented transducer system becomes

$$\text{I.L. (untuned, segm.)} = \text{I.L. (untuned, unsegm.)} - 10 \log_{10} L^2 \qquad [89]$$

Additional reduction of insertion loss is achieved if a broadband transducer is used between the transducer and the source. The insertion loss is then given by Eq. [89] with an additional term of the form $-10 \log_{10} N^2$ where N is the transformation ratio. Many such broadband transformers are commercially available.

References:

[1] F. M. Smits and L. E. Gallaher, "Design Considerations for a Semipermanent Optical Memory," **Bell Syst. Tech. J.**, Vol. 46, p. 1267, July-August, 1967.

[2] L. K. Anderson, S. Brojdo, J. T. LaMacchia, and L. H. Lin, "A High-Capacity Semipermanent Optical Memory," **IEEE J. Quant. Elec.**, Vol. QE-3, p. 245, 1967.

[3] R. J. Collier, "Holograms for Information Storage," **J. Opt. Soc. Amer.**, Vol. 58, p. 1548, Nov. 1968.

[4] J. A. Rajchman, "Promise of Optical Memories," **J. Appl. Phys.**, Vol. 41, p. 1376, March 1970.

[5] R. D. Lohman, R. S. Mezrich, and W. C. Stewart, "Holographic Mass Memory's Promise: Megabits Accessible in Microseconds," **Electronics**, p. 61, 18 Jan. 1971.

[6] R. Whitman, A. Korpel, and S. Lotsoff, **Proc. Symp. on Modern Optics**, Polytechnic Press, N. Y., (1967) p. 243.

[7] A. Korpel, R. Adler, P. Desmares, and W. Watson, "Television Display Using Acoustic Deflection and Modulation of Coherent Light," **Appl. Opt.**, Vol. 5, p. 1667, Oct. 1966.

[8] I. Gorog, J. D. Knox, and P. V. Goedertier, "A Television Rate Laser Scanner," **RCA Review** (to be published).

[9] A. J. DeMaria, "Ultrasonic Diffraction Shutters for Optical Maser Oscillators," **J. Appl. Phys.**, Vol. 34, p. 2984, Oct. 1963.

[10] D. L. Lyon and T. S. Kinsel, "Transitions Between Mode-Locked States in Intracavity Phase-Modulated Lasers," **Appl. Phys. Let.**, Vol. 16, p. 89, Feb. 1970.

[11] O. R. Wood, R. L. Abrams, and T. J. Bridges, "Mode Locking of a Transversely Excited Atmospheric Pressure CO_2 Laser," **Appl. Phys. Let.**, Vol. 17, p. 376, 1 Nov. 1970.

[12] G. A. Coquin, J. P. Griffin, and L. K. Anderson, "Wide-Band Acousto-optic Deflectors Using Acoustic Beam Steering," **IEEE Trans. Sonics and Ultrasonics**, Vol. SU-17, p. 34, 1970.

[13] E. I. Gordon, "A Review of Acousto-optical Deflection and Modulation Devices," **Proc. IEEE**, Vol. 54, p. 1391, 1966.

[14] D. A. Pinnow, "Acousto-Optic Light Deflection: Design Considerations for First-Order Beam-Steering Transducers," **IEEE Trans. Sonics and Ultrasonics**, Vol. SU-18, p. 209, 1971.

[15] D. A. Pinnow, L. G. Van Uitert, A. W. Warner, and W. A. Bonner, "Lead Molybdate: A Melt-Grown Crystal with a High Figure of Merit for Acousto-Optic Device Applications," **Appl. Phys. Let.**, Vol. 15, p. 83, 1 Aug. 1969.

[16] D. A. Pinnow and R. W. Dixon, "Alpha-Iodic Acid: A Solution-Grown Crystal with a High Figure of Merit for Acousto-Optic Device Applications," **Appl. Phys. Let.**, Vol. 13, p. 156, 1968.

[17] T. Yano, A. Fukumoto, and A. Watanabe, "Telluride Glass: A New Acousto-Optic Material," **J. Appl. Phys.**, Vol. 42, p. 3674, Sept. 1971.

[18] S. T. Peng and E. S. Cassedy, **Proc. Symp. on Modern Optics**, Polytechnic Press, New York (1967), p. 299.

[19] L. Bergstein and D. Kermish, **Proc. Symp. on Modern Optics**, Polytechnic Press, New York (1967), p. 655.

[20] R. S. Chu and T. Tamir, "Guided-Wave Theory of Light Diffraction by Acoustic Microwaves," **IEEE Trans. Microwave Theory and Techniques**, Vol. MTT-17, p. 1002, 1969.

[21] W. R. Klein and G. D. Cook, **IEEE Trans. Sonics and Ultrasonics**, Vol. SU-14, p. 123, 1967.

[22] E. K. Sittig and H. D. Cook, "A Method for Preparing and Bonding Ultrasonic Transducers Used in High-Frequency Digital Delay Lines, "**Proc. IEEE**, Vol. 56, p. 1375, 1968.

[23] J. D. Larson and D. K. Winslow, "Ultrasonically Welded Peizoelectric Transducers," **IEEE Trans. Sonics and Ultrasonics**, Vol. SU-18, p. 142, 1971.

[24] J. F. Nye, **Physical Properties of Crystals**, Clarendon Press, Oxford, 1957.

[25] D. A. Berlincourt, D. R. Curran, and H. Jaffe, **Physical Acoustics**, Vol. I, Part A, Ed. by W. P. Mason, Academic Press, New York, 1964.

[26] A. A. Oliner, "Microwave Network Methods for Guided Elastic Waves," **IEEE Trans. Microwave Theory and Techniques**, Vol. MTT-17, p. 812, 1969.

[27] C. G. Montgomery, R. H. Dicke, and E. M. Purcell, **Principles of Microwave Circuits**, McGraw Hill, New York, 1948.

[28] T. F. Hueter and R. H. Bolt, **Sonics**, J. Wiley and Sons, New York, 1966.

[29] A. W. Warner, M. Onoe, and G. A. Coquin, "Determination of Elastic and Piezoelectric Constants for Crystals in Class (3m)," **J. Acous. Soc. Amer.**, Vol. 42, p. 1223, 1967.

RCA Technical Papers Second Quarter, 1972

April

"Analog Memory Devices Employing PE-FE Interactions for Adaptive Control Voltage Modules," S. S. Perlman, J. H. McCusker, and S. M. Boardman, **IEEE Trans. GSU**

"The Bismuth Titanate FE-PC Optical Storage Medium—Further Developments," G. W. Taylor, **IEEE Trans. GSU**

"Calculation of Deposition Profiles and Compositional Analysis of Co-sputtered Films," J. J. Hanak, H. W. Lehmann, and R. K. Wehner, **J. Appl. Phys.**

"Electrophotography—A Review," R. B. Comizzoli, G. S. Lozier, and D. A. Ross, **Proc. IEEE**

"An ELF Wide-Band Noise Receiver," J. O. Sinniger, **IEEE Trans. GGE**

"Ferroelectric Light Valve Arrays for Optical Memories," G. W. Taylor and W. F. Kosonocky, **IEEE Trans. GSU**

"High-Efficiency Operation of GaAs Schottky-Barrier IMPATTS," H. C. Huang, P. A. Levine, A. R. Gobat, and J. B. Klatskin, **Proc. IEEE** (Letters)

"High-Performance Low-Power CMOS Memories Using Silicon-on-Sapphire Technology," J. E. Meyer and Coauthor, **IEEE J. Solid-State Circuits**

"Lang Topographic Studies of III-V Heteroepitaxial Films Grown on Sapphire and Spinel," S. H. McFarlane III and C. C. Wang, **J. Appl. Phys.**

"Magnetocapacitance Effect in a Metal-$CdCr_2Se_4$ Junction," M. Toda and S. Tosima, **J. Appl. Phys.**

"Preparation, Microstructure, and High-Field Superconducting Properties of Nb_3Sn Doped with Group-III, -V, and -VI Elements," R. E. Enstrom and J. R. Appert, **J. Appl. Phys.**

"The Quality of Starting Silicon," A. Mayer, **Solid State Tech.**

"The Role of Space-Charge-Limited Currents in Photoconductivity-Controlled Devices," A. Rose, **IEEE Trans. GED**

"Solid State: Microwave Power Sources," H. Sobol and F. Sterzer, **IEEE Spectrum**

"Thermally Fixed Holograms in $LiNbO_3$," D. L. Staebler and J. J. Amodei, **IEEE Trans. GSU**

"Electric-Field-Dependent Magnetoresistance in Ferromagnetic Semiconductors," I. Balberg and H. L. Pinch, **Phys Rev. Letters** (3 April)

"Height-to-Width Converter Digitizes Analog Samples," R. J. Turner, **Electronics** (Designer's Casebook) (April 10)

May

"Bialkali (K_2CsSb) Photocathode as a High-Gain Secondary Electron Emitter," A. H. Sommer, **J. Appl. Phys.** (Communications)

"Reply to 'Comment on Temperature Dependence of Hole Velocity in p GaAs'," V. L. Dalal, A. B. Dreeben, and A. Triano, **J. Appl. Phys.** (Communications)

"Computer Calculation of Device, Circuit, Equipment, and System Reliability," D. R. Crosby, **IEEE Trans. GR**

"Fine Line Printing for Consumer Electronics," R. A. Vogel, **Solid State Tech.**

"The Future for LEDs," C. J. Nuese, H. Kressel, and I. Ladany, **IEEE Spectrum**

"GaAs Vapor-Grown Shockley Diodes and Semiconductor-Controlled Rectifiers," C. R. Wronski, C. J. Nuese, and H. F. Gossenberger, **IEEE Trans. GED** (Correspondence)

"A High Performance Television Receiver Experiment," D. H. Pritchard, A. C. Schroeder, and W. G. Gibson, **IEEE Trans. GBTR**

"Influence of Deposition Temperature on Composition and Growth Rate of $GaAs_xP_{1-x}$ Layers," V. S. Ban, H. F. Gossenberger, and J. J. Tietjen, **J. Appl. Phys.** (Communications)

"Phase Detector Data Distortion in Phase-Lock Loop Receivers," G. D. O'Clock, Jr., **IEEE Trans. GAES** (Correspondence)
"Properties of Electron Surface States on Liquid Helium," R. S. Crandall and R. Williams, **Phys. Rev. A**
"Magnetic Properties of Granular Nickel Films," J. I. Gittleman, S. Bozowski and Coauthor, **Phys. Rev. B** (1 May)

June

"Correction to 'Applications of Integrated-Circuit Technology to Microwave Frequencies,'" (H. Sobol, **Proc. IEEE,** Vol. 59, pp. 1200-1211, Aug. 1971), H. Sobol, **Proc. IEEE** (Letters)
"Communicating with the Engineer Who Becomes Unemployed," T. G. Greene, **IEEE Trans. GPC**
"A Comparative Study of IMPATT Diode Noise Properties," P. A. Levine and V. W. Chan, **Proc. IEEE** (Letters)
"A Computer-Controlled RF Test System," F. Pfifferling and D. H. Williamson, **IEEE Trans. GMFT**
"Detection of Multiple Faults in Combinational Logic Networks," I. Kohavi and Coauthor, **IEEE Trans. GC**
"The Distribution of Gains in Uniformly Multiplying Avalanche Photodiodes: Experimental," J. Conradi, **IEEE Trans. GED**
"The Distribution of Gains in Uniformly Multiplying Avalanche Photodiodes: Theory," R. J. McIntyre, **IEEE Trans. GED**
"Electrical Properties of Silicon Films on Sapphire Using the MOS Hall Technique," A. C. Ipri, **J. Appl. Phys.**
"Electrophotography: A Review," R. B. Comizzoli, G. S. Lozier, and D. A. Ross, **RCA Review**
"Evolution Not Revolution—Electronic Data Communications," J. M. Osborne, **Signal**
"Free Charge Transfer in Charge-Coupled Devices," J. E. Carnes, W. F. Kosonocky, and E. G. Ramberg, **IEEE Trans. GED**
"Improved Diode and Circuit Procedures for High-Efficiency S-Band Oscillators," A. S. Clorfeine, H. J. Prager, and R. D. Hughes, **Proc. IEEE** (Letters)
"Infrared Transmission Microscopy Utilizing a High-Resolution Video Display," R. A. Sunshine and N. Goldsmith, **RCA Review**
"An Investigation of the Effects of the Error Rate of Multiple Phase-Shift-Keyed Signals Through a Hard Limiter," B. E. Tyree and Coauthor, **IEEE Trans. GCOM, Pt. 1**
"Low-Voltage Electron-Beam-Pumped Lasing of CdS at Atmospheric Pressure," F. H. Nicoll, **IEEE Trans. GED** (Correspondence)
"Luminescence from GaN MIS Diodes," J. I. Pankove and P. E. Norris, **RCA Review**
"Modulation Transfer Function Calculation of Electrostatic Lenses," I. P. Csorba, **RCA Review**
"Negative Electron affinity Materials in Photomultipliers," B. F. Williams, **IEEE Trans. GNS**
"Negative Resistance in Cadmium Selenide Powder-Comparison of Experiment and Theory," L. J. Nicastro and E. L. Offenbacher, **RCA Review**
"Noise Sources in Charge-Coupled Devices," J. E. Carnes and W. F. Kosonocky, **RCA Review**
"Psychology of Sound Reproduction," H. F. Olson, **Audio**
"Recent Work on Fast Photomultipliers Utilizing GaP(Cs) Dynodes," H. R. Krall and D. E. Persyk, **IEEE Trans. GNS**
"A Review of the Technological and Electromagnetic Limitations of Hybrid Circuits for Microwave Applications," H. Sobol, **IEEE Trans. GPHP**
"Second-Harmonic Generation and Miller's Delta Parameter in a Series of Benzine Derivatives," P. D. Southgate and D. S. Hall, **J. Appl. Phys.**
"A Simplified Method for the Determination of Particle Size Distributions of Fine Magnetic Powders," J. W. Robinson and E. F. Hockings, **RCA Review**
"16-Bit Switchable Acoustic Surface-Wave Sequence Generator/Correlator," G. D. O'Clock, Jr., D. A. Gandolfo, and R. A. Sunshine, **Proc. IEEE** (Letters)
"A Solid-State Transponder Source Using High-Efficiency Silicon Avalanche Oscillators," J. F. Reynolds, J. Assour, and A. Rosen, **RCA Review**
"Stable Voltage Reference Sources," D. Hampel, **IEEE J. Solid-State Circuits** (Correspondence)
"Transmission Electron Microscopy of Granular Nickel/SiO_2 Cermet Films," M. S. Abrahams, C. J. Buiocchi, M. Rayl, and P. J. Wojtowicz, **J. Appl. Phys.**
"Band-Edge Excitons in PbI_2: A Puzzle?" G. Harbeke and Coauthor, **Phys. Rev. Letters** (12 June)
"Electron-Paramagnetic-Resonance Spectrum of Mo^{5+} in $SrTiO_3$—An Example of the Dynamic Jahn-Teller Effect," B. W. Faughnan, **Phys. Rev. B** (15 June)
"Efficiency of the Electrochemiluminescent Process," P. M. Schwartz, R. A. Blakeley, and B. B. Robinson, **J. Phys. Chem.** (June 22)

Patents Issued to RCA Inventors Second Quarter, 1972

April

J. M. Assour, A. Rosen, and J. F. Reynolds High Efficiency Mode Avalanche Diode Oscillator (3,659,222)
B. B. Bell and W. E. Pederson Slurry Process for Coating Particulate Material Upon a Surface (3,653,941)
U. Bharali, Four-Phase High Speed Counter (3,654,441)
R. W. Bruce, Jr. Corona Generating Circuits for Electrophotographic Printers Cooperatively Operating with Television Receivers (3,655,912)
B. L. Dickens, B. F. Melchionni, and R. R. Werner Web Cartridge (3,653,608)
B. L. Dickens, L. J. Kudla, A. C. Luther, Jr. and B. F. Melchionni Web Handling Apparatus (3,654,400)
F. A. Digilio Motion Transfer Mechanism (3,655,126)
R. W. Etter Color Kinescope Production with a Temporary Mask (3,653,901)
J. A. Files Method of Manufacture of Cathode Ray Tubes Having Frit-Sealed Envelope Assemblies (3,658,401)
T. U. Foley Transmission Line Filter (3,659,232)
R. A. Freggens Internal Configuration for a Radial Heat Pipe (3,658,125)
J. W. Gaylord Internal Construction for Plastic Semiconductor Packages (3,659,164)
F. R. Goldammer and H. D. Albrecht, Jr. Coil Suspension Arrangement for a Cathode Ray Tube (3,657,674)
D. L. Greenaway and J. P. Russell High Fidelity Readout of a Hologram Performing the Function of a Complex Wave Modifying Structure (3,658,403)
D. L. Greenaway Complex Wave Modifying Structure Holographic System (3,658,404)
G. D. Hanchett Counter (3,654,440)
G. H. Heilmeier Liquid Crystal Display Assembly Having Independent Contrast and Speed of Response Controls (3,655,269)
F. A. Helvy Method of Making a Multialkali Photocathode with Improved Sensitivity to Infrared Light and a Photocathode Made Thereby (3,658,400)
T. W. Kisor Static Charge Protective Packages for Electron Devices (3,653,498)
K. Louth Video Tape Recorder Synchronizing System (3,654,387)
K. Louth Device to Keep a Capstan in Phase When Switching Modes (3,654,398)
R. A. Mao Circuits for Driving Loads Such as Liquid Crystal Displays (3,653,745)
F. J. Marlowe and E. O. Nester Alternating Voltage Excitation of Liquid Crystal Display Matrix (3,654,606)
D. D. Mawhinney Microwave Oscillator with Two or More Paralleled Semiconductive Devices (3,659,223)
A. Month and D. L. Thornburg Method of Fabricating a Porous Tungsten Body for a Dispenser Cathode (3,653,883)
J. E. Meyer Decoder Circuit Employing Switches Such As Field Effect Devices (3,659,118)
F. H. Mosher and E. G. Jenney Cable Harness Assembly Board and Method of Making the Same (3,653,411)
L. S. Napoli Waveguide Structure (3,654,572)
L. S. Napoli and J. J. Hughes Semiconductor Device with Plurality of Small Area Contacts (3,656,030)
L. S. Napoli Strip-Type Directional Coupler Having Elongated Aperture in Ground Plane Opposite Coupling Region (3,659,228)
F. H. Nicoll Electron Beam Excited Laser (3,657,735)
P. E. Norris, Method of Detecting the Completion of Plasma Anodization of a Metal on a Semiconductor Body (3,658,672)
L. A. Olson Test System for Electrical Apparatus (3,659,044)
C. S. Planzo Semiconductor Device Package (3,659,035)

J. A. Rajchman and W. F. Kosonocky Electrically and Optically Accessible Memory (3,656,121)
M. R. Royce Visible-Emitting Cerium-Activated Calcium Aluminum Oxide Phosphor (3,657,138)
C. C. Wang Epitaxial Silicon on Hydrogen Magnesium Aluminate Spinel Single Crystals (3,658,586)
Z. A. Weinberg Charge Coupled Device (3,656,011)
C. P. Wen Microwave Hybrid Comprising Through Waveguide and Balanced Mixer Utilizing Same (3,654,556)
A. E. Widmer Zn Diffusion Into GaP (3,653,989)
S. Wlasuk Lightning Protection System (3,656,062)
O. M. Woodward Wide Band Balun (3,656,071)

May

T. R. Allington and J. R. McClellan Method of Adjusting the Resistivity of Thick-Film Screen-Printed Resistors (3,663,276)
J. J. Amodei and R. Williams Electro-Optical Memory (3,660,818)
J. Avins Balanced Angle Modulation Detector (3,667,060)
W. H. Barkow Beam Convergence Exciter for Shadow Mask Color Picture Tube (3,663,907)
H. W. Becke, E. F. Cave, and D. Stolnitz High Power Frequency Device (3,659,334)
N. W. Brackelmanns Method for Making Transistors Including Gain Determining Step (3,666,573)
R. L. Brooks Method for Monitoring the Capacitance of a Capacitor While Adjusting Its Capacitance (3,665,570)
J. R. Collard, S. Y. Narayan, and J. P. Paczkowski Semiconductor Diode (3,665,254)
R. P. Crow Sequential AGC System for Signal Receiver (3,665,317)
J. F. Dienst Frequency Modulation by Light Impingement on a Solid State Oscillator (3,662,289)
W. V. Dix Memory Sense Amplifier Inherently Tolerant of Large Input Disturbances (3,663,887)
W. G. Einthoven and H. K. Donnell Method of Manufacturing Semiconductor Devices Having High Planar Junction Breakdown Voltage (3,664,894)
W. W. Evans VHF/UHF Interlock Circuit (3,662,270)
N. Feldstein Method for Photodepositing Smaller Size Image Screen Areas for Cathode Ray Tube from Larger Size Mask Apertures (3,661,581)
N. Feldstein and T. S. Lancsek Method of Electroless Deposition of Metals with Improved Sensitizer (3,666,527)
E. C. Giaimo, Jr. Manifold for Fountain-Type Liquid Dispenser (3,664,298)
N. M. Goun and C. F. Wheatley, Jr. Heat Dissipation for Power Integrated Circuits (3,665,256)
A. P. Haines Method of Rebuilding an Evacuated Electron Tube (3,663,862)
L. C. Harlow, S. D. Ransberg, and L. L. Mehaffey Automatic Record Molding Apparatus and Method (3,662,051)
L. A. Harwood Selective Tint Correction Circuits (3,663,744)
F. L. Katnack Semiconductor Device Employing Two-Metal Contact and Polycrystalline Isolation Means (3,667,008)
H. Kressel and J. I. Pankove Semiconductor Electron Emitter (3,667,007)
P. Kuznetzoff Method for Making a Kinescope Comprising Production and Treatment of a Temporary Mask (3,663,997)
W. W. Lee Correlation Peak Detector in Optical Spatial Filtering System (3,666,359)
S. Liu Self-Pulsed Microwave Oscillator (3,665,339)
D. L. Matthies Compounded Liquid Crystal Cells (3,661,444)
E. E. Mayaud Photographic Method for Producing a Cathode-Ray Tube Screen Structure (3,661,580)
A. Z. Miller Method of Bonding Metals Together (3,662,454)
H. I. Moss Magnetic Head Material Method (3,661,570)
J. J. O'Toole Compensated Television Matrix Amplifiers (3,663,745)
H. W. Silverman Checking an Automatic Testing System (3,665,504)
R. M. Stahl Tape Player with Fast Tape Winding Mechanism (3,666,153)
M. W. Vigh and H. T. Rocheleau Method of Removing Polyurethane Resin Protective Coating (3,661.641)
H. R. Warren Record Medium Guide (3,661,311)
P. K. Weimer Image Sensor Array in Which Each Element Employs Two Phototransistors One of Which Stores Charge (3,660,667)

June

T. R. Allington Method of Making a Thick-Film Hybrid Circuit (3,669,733)
T. G. Athanas Input Transient Protection for Complementary Insulated Gate Field Effect Transistor Integrated Circuit Device (3,673,428)
J. Avins and J. Craft Combined Tuning and Signal Strength Indicator Circuit with Signal Strength Indication Derived from Each IF Amplifying Stage (3,673,499)
R. L. Barbin Toroidal Deflection Yoke Having Asymmetrical Windings (3,668,580)
P. S. Carnt and G. Schiess Television Apparatus Responsive to a Transmitted Color Reference Signal (3,673,320)
R. B. Clover, Jr. Bubble Domain Sonic Propagation Device (3,673,582)
M. Cooperman High Speed Set-Reset Flip-Flop (3,671,768)
F. T. D'Augustine Process for Screening Cathode Ray Tubes Including Salvaging of Excess Phosphor Slurry (3,672,932)
A. G. F. Dingwall Method of Fabrication of Photomasks (3,673,018)
J. P. Dismukes Low Temperature Silicon Etch (3,669,774)
N. Feldstein Method of Making Abrasion-Resistant Metal-Coated Glass Photomasks (3,669,770)
N. Feldstein Method of Preparing a Substrate for Depositing a Metal on Selected Portions Thereof (3,672,925)
D. G. Fisher Method for Activating a Semiconductor Electron Emitter (3,669,735)
R. A. Freggens Method of Making a Heat Pipe Having an Easily Contaminated Internal Wetting Surface (3,672,020)
W. J. Greig and R. R. Soden Semiconductor Device with Multi-Level Metalization and Method of Making the Same (3,668,484)
G. D. Hanchett Switching Circuits (3,671,778)
J. R. Harford Gain Controlled Cascode-Connected Transistor Amplifier (3,673,498)
S. Y. Husni Method of Connecting Semiconductor Device to Terminals of Package (3,668,770)
C. C. Ih and M. J. Lurie Recording of a Continuous Tone Focused Image on a Diffraction Grating (3,669,673)
C. J. Jacob and G. W. Lawton Method of Making Electrical Connections to a Glass-Encapsulated Semiconductor Device (3,669,734)
L. B. Kimbrough Method of Mounting a Mass in a Cathode-Ray Tube Using Retractable Spacing Units (3,672,014)
J. E. Krupa and M. R. Paglee Field Effect Transistor Modulator Circuit (3,668,561)
M. L. Levene and M. Yamamoto Electrostatic Printing Apparatus (3,672,763)
A. L. Limberg Synchronous Demodulator Employing a Common-Base Transistor Amplifier Input (3,673,505)
G. J. Meslener Sampling Decoder for Delay Modulation Signals (3,670,249)
A. Miller Digital Light Deflector Using Optical Resonators (3,672,746)
P. C. Olsen and P. C. Tang Video Blanking and Sound Muting Circuit (3,673,318)
R. C. Owens and L. P. Thomas Kinescope Socket (3,668,475)
W. S. Pike Electrical Circuit (3,670,179)
L. A. Rempert and E. P. Helpert Machine Implemented Method for Positioning and Inspecting an Object (3,670,153)
G. C. Robitschek Transducing Head Mount Apparatus (3,668,668)
D. A. Ross Method of and Apparatus for Reproducing a Colored Image by Electrophotographic Means (3,667,841)
E. R. Schrader Method of Energizing Fully Persistent, High Field, High Homogeneity Magnets (3,668,581)
W. W. Siekanowicz Broadband Circulator Wherein Differential Phase Shift Varies with Frequency in Predetermined Manner (3,668,563)
L. E. Smith and R. J. Gries Raster Correction Circuit Utilizing Vertical Deflection Signals and High Voltage Representative Signals to Modulate the Voltage Regulator Circuit (3,668,463)
R. D. Smith Computer with Program Tracing Facility (3,673,573)
L. J. Thorpe Special Effects Generators for Providing Iris-Type Television Displays (3,671,667)
H. A. Wittlinger, C. F. Wheatley, Jr., and R. D. Knapp Sample-Hold and Read Circuit (3,671,782)
J. J. Yorganjian Resettable Logic Gate Multivibrator (3,671,881)

Gerard A. Alphonse attended New York University where he obtained a B.S.E.E. in 1958 and a M.S.E.E. in 1959, after doing research in the field of superconductivity. He joined the RCA Laboratories in June 1959 and worked toward the development of superconductive memories. In 1963 he attended the Polytechnic Institute of Brooklyn under an award from RCA Laboratories, obtaining his Ph.D. in Electrophysics in 1967. In addition to his work on superconductivity, he has also done research on photochromic memories and more recently, has made contributions in the field of Acousto-Optics. Dr. Alphonse received an "Outstanding Research Award" from RCA in 1960 for his work in superconductivity. Besides his work at RCA, he is a physics instructor in the Evening Division of La Salle College in Philadelphia.

He is a senior member of the IEEE, a member of Eta Kappa Nu, Tau Beta Pi, the American Institute of Physics, and the Optical Society of America.

Ralph W. Engstrom received his Ph.D. in Physics from Northwestern University in 1939. Since joining RCA Corporation in 1941, he has been associated as an engineer and engineering manager with various photosensitive devices, including photomultipliers, image tubes and camera tubes. Dr. Engstrom is a Fellow in the American Physical Society and a Member of Sigma Xi.

Michael G. Kovac received the B.S. degree from the University of Notre Dame, Notre Dame, Ind., in 1963, and the M.S. and Ph.D. degrees from Northwestern University, Evanston, Ill., in 1967 and 1970, respectively, all in electrical engineering. His research activities have included investigations of an x-ray imaging system based on the electron beam scanning of a mosaic target coupled to a gas-filled detection chamber, of x-ray-induced secondary electron emissions from metal-insulator layers, and of various aspects of a two-dimensional, beam-scanned ultrasonic imaging system. He has worked at the General Electric Industry Control Department, Salem, Va., and since 1970 has been associated with RCA Laboratories, Princeton, N. J., where he has been concerned with silicon and thin-film self-scanned imaging systems. His work has included investigations of both x-y addressed image sensors and of charge-transfer image sensors.

Dr. Kovac is a member of Tau Beta Pi, Eta Kappa Nu, and Sigma Xi.

Henry Kressel received the B.A. degree from Yeshiva College in 1955. He received the S.M. degree in Applied Physics from Harvard University in 1956, and the M.B.A. and Ph.D. degree from the University of Pennsylvania in 1959 and 1965, respectively. Dr. Kressel joined RCA Electronic Components and Devices, Somerville, N. J., in 1959. He has been instrumental in the research and development of high-frequency mesa, planar, and planar epitaxial silicon transistors. In 1961 Dr. Kressel became head of the microwave diode group, where he was responsible for research, development, and pilot-line engineering of gallium arsenide and silicon varactor diodes. From 1963 to 1965, he was on leave of absence doing doctoral work in metallurgy. Upon his return to RCA in 1965, he became head of the Device Physics Group in the Technical Programs Laboratory (Somervile, N. J.). He joined RCA Laboratories, Princeton, in 1966. He is currently head of the semiconductor Optical Devices Research Group. Dr. Kressel is a member of the IEEE, The American Physical Society, and Sigma Xi.

Ivan Ladany received the B.S. and M.S. degrees from Northwestern University, Evanston, Ill. In 1953 he joined the Naval Research Laboratory, Washington, D. C., where he worked briefly in the field of underwater sound, spending most of his time in semiconductor device research. Since joining RCA Laboratories, Princeton, N. J., in 1966, he has worked on GaP, GaAlP, and GaAs luminescent diode problems.

Mr. Ladany is a member of the American Physical Society and Sigma Xi. In 1969 he was awarded an RCA Laboratories Achievement Award for his contributions to GaP electroluminescence.

Winthrop S. Pike received the B.A. degree in physics from Williams College, Williamstown, Mass., in 1941. Shortly thereafter, he entered the U. S. Army Signal Corps as a Radar Officer. He was discharged as a Captain in 1946, and became a Member of the Technical Staff of RCA Laboratories, Princeton, N. J. He has done work on sensory aids for the blind, storage tubes and their application, color television receivers, cameras and encoders, highway-vehicle control devices, industrial and educational television camera chains, electronic devices for medical applications, high-altitude balloon-borne television systems for astronomical observations, and camera and data collecting systems using solid-state sensors.

Mr. Pike has been the recipient of five RCA Achievement Awards.

Frank V. Shallcross received the A.B. degree in chemistry from the University of Pennsylvania, Philadelphia, in 1953, and the Ph.D. degree in physical chemistry from Brown University, Providence, R. I., in 1958. He was employed as a chemist by M.&C. Nuclear, Inc., Attleboro, Mass., from 1957 to 1958. In 1958 he joined RCA Laboratories, Princeton, N. J. At RCA he has done research on laser materials, thin-film photoconductors and semiconductors, television camera tubes, thin-film active devices, and silicon and thin-film self-scanned sensor arrays.

Dr. Shallcross is the recipient of an RCA Laboratories Achievement Award. He is a member of the American Chemical Society, the American Institute of Chemists, the American Association for the Advancement of Science, Phi Beta Kappa, and Sigma Xi.

J. L. Vossen joined RCA in 1958 after receiving a B.S. in physics from St. Joseph's College. He was first associated with the Microelectronics Department of the RCA Solid-State Division in Somerville, N. J. There, his work centered on thick- and thin-film passive component processes. In 1962, Mr. Vossen transferred to the Advanced Communications Laboratory of the Defense Communications Systems Division in New York City, where he led a group conducting research on precision thin film resistors and capacitors. In 1965 he joined the Process Research and Development Laboratory of the RCA Laboratories in Princeton, N. J., where he has been engaged in research on sputtering processes and other physical methods of film deposition.

Mr. Vossen is a member of the American Physical Society, the American Vacuum Society, the Electrochemical Society and Sigma Xi.

John H. Sternberg received the B.S. degree in Electrical Engineering from Cornell University in 1950. From 1950 to 1961, except for a two-year period in which he was self-employed, he was with the General Electric Company. Early assignments included electronic design in the airborne radar field and instruction to U. S. Air Force personnel in the Far East theatre. Subsequently, he became part of the W2F-1 (Hawkeye) Project Office, as project engineer responsible for the aircraft's search radar and Rotodome antenna.

Mr. Sternberg joined RCA AED in 1961 as a project engineer for the Nimbus Satellite's Advanced Vidicon Camera System (AVCS). Following this, he directed Resource Planning for the Video and Communication subsystems of the Mobile Lunar Laboratory design study, and later became Equipment Manager for all Nimbus subsystem development participating extensively in the development of the High Data Rate Storage System (HDRSS), the unified tape recorder for Nimbus. In 1967, he became Project Manager of a classified program. Since 1969, he has been active on development of the two-inch return beam vidicon cameras for the Earth Resources Technology Satellite (ERTS) and the silicon version of the two-inch RBV. He is currently Manager, Ground Data Handling Programs.

Mr. Sternberg is a member of Eta Kappa Nu.

Paul K. Weimer received his A.B. degree from Manchester College in 1936, his M.A. degree in physics from the University of Kansas in 1938, and his Ph.D. degree in physics from Ohio State University in 1942. From 1937 to 1939, he taught physics and mathematics at Tabor College, Hillsboro, Kansas. Since 1942, Dr. Weimer has been engaged in research at RCA Laboratories, Princeton, N. J., where he is a Fellow, Technical Staff, and Head of Solid-State-Scanned Device Research. At RCA Laboratories he has participated in the basic development of various types of television tubes and solid-state devices. From 1959 to 1960, Dr. Weimer was granted an RCA fellowship for study abroad, which was spent at the Laboratoire de Physique, Ecole Normale Superieure, Paris, France, working in the field of semiconductors. He was recipient of a Television Broadcasters' Award in 1946, the IRE Vladimir K. Zworykin Television Prize in 1959, and the 1966 IEEE Morris N. Liebmann Prize Award. In 1968, Dr. Weimer was awarded an honorary degree of Doctor of Science by Manchester College. He is a Fellow of the Institute of Electrical Engineers and a member of the American Physical Society.